FIRST-PRINCIPLES STUDY OF PALLADIUM-BASED METAL ALLOYS AS HYDROGEN PURIFICATION MEMBRANES

A Dissertation

Presented to

The Academic Faculty

by

Chen Ling

In Partial Fulfillment

Of the Requirements for the Degree

Doctor of Philosophy in Chemical Engineering

Georgia Institute of Technology

December, 2009

FIRST-PRINCIPLES STUDY OF PALLADIUM-BASED METAL ALLOYS AS HYDROGEN PURIFICATION MEMBRANES

Approved by:

Dr. David S. Sholl, Advisor
School of Chemical & Biomolecular Engineering
Georgia Institute of Technology

Dr. Pradeep G. Agrawal
School of Chemical & Biomolecular Engineering
Georgia Institute of Technology

Dr. Tom Fuller
School of Chemical & Biomolecular Engineering
Georgia Institute of Technology

Dr. Christopher W. Jones
School of Chemical & Biomolecular Engineering
Georgia Institute of Technology

Dr. Faisal M. Alamgir
School of Materials Science and Engineering
Georgia Institute of Technology

Date Approved: October 30, 2009

To my parents,

For always insisting upon education,

and

To my girlfriend,

Lingjia,

For always being there to support me.

ACKNOWLEDGEMENTS

This research project would not have been possible without the support of many people. First I wish to express my gratitude to my supervisor, Dr. David Sholl, who was abundantly helpful and offered invaluable assistance, support and guidance. Dr. Sholl has not only aided in my growth as a professional but as an overall human being by introducing both aspects of life through his own example.

I would like to thank all my graduate friends, especially former group members Dr. Haibin Chen and Dr. XinLi for their kindness and friendship. I would also like to thank current group members Dr. Hao and Dr. Semidey-Flecha for their cooperation in making a collaborative work a complete success.

Special thanks to Dr. Tom Fuller, Dr. Faisal Alamgir, Dr. Pradeep Agrawal, and Dr. Christopher Jones for their comments and questions as members of my thesis committee.

I am grateful to my parents, Yanzhu Ling and Dingya Yu, for their constant love and support. And I am especially thankful to my girlfriend, Lingjia Li, for giving me the courage to continue, for believing in me, and for always standing by my side.

TABLE OF CONTENTS

LIST OF TABLES

Page

LIST OF FIGURES

Page

SUMMARY

Hydrogen is a good candidate as a future energy source. Current technologies generate hydrogen from hydrocarbons as mixtures with other species like CO and CO_2. High flux and resistance to contaminants are required for membranes used to separate hydrogen from these mixtures, as well as other requirements such as long operation standard and low cost. Development of new membranes is hampered by the large effort and time required to experimentally develop and test these membranes. I show how first-principles Density Functional Theory (DFT) calculations combined with coarse-grained modeling can be used to predict the performance of metal alloys as H_2 purification membranes. I introduce quantitative modeling methods based on DFT calculations that assess the relative role of surface resistances for metal alloy membranes, the bulk permeation rate through alloy membranes, and the selectivity of metal membranes. In my study, I first examined the importance of surface processes for thin membranes. The possibility of using new materials such as PdCuAg ternary alloys and metal sulfides as hydrogen purification membranes were examined. Finally I predicted the absorption and diffusion of another atomic species, carbon, in the membranes. My methods require no experimental input apart from the knowledge of the bulk crystal structure, so they provide an alternate way to explore new materials as hydrogen purification membranes. My results will be a useful guide for future experimental studies.

I. Introduction

1.1 Metal membranes in H_2 purification

As an abundant "elementary" resource at a global level—not only in the vast waters of the oceans but also everywhere in the organic world, from biomass to hydrocarbons—hydrogen is a potential source with huge energy capacity.[1] The large-scale exploitation of hydrogen would make it possible to achieve a dramatic reduction in CO_2 emissions. Nevertheless, pure hydrogen doesn't exist naturally, so it must be produced from other resources. Broadly, two possible processes exist for doing this. Hydrogen can be obtained by water electrolysis or water splitting, the most promising method to produce hydrogen in a fully sustainable fashion. However, due to the large energy requirement in the water splitting remaining unsolved, currently hydrogen is most economically extracted from fossil fuels by the reforming of hydrocarbon sources with steam and/or partial oxidation of hydrocarbons. These methods also produce other by-products with H_2 such as CO, CO_2, CH_4, and trace amount of other species.

One critical need for use of hydrogen fuels is the ability to purify hydrogen from mixed gas streams.[2] For example, many fuel cells require highly purified hydrogen. Trace contaminants such as S-containing species can severely inhibit these devices. Membranes for gas separations are often favorable since they typically require less energy than other competing methods such as cryogenic distillation.[3, 4, 5, 6] Dense metal membranes are well known in application for H_2 purification and have many advantages over alternative purification methods. Pure Pd is well known as a metal that

can be used as a H_2 purification material. Despite the wide commercial success of Pd membranes, several factors limit their widespread applications.[7] At temperatures below 573 K and moderate H_2 pressures, a Pd hydride phase forms with lattice constant substantially different from pure Pd. Membrane integrity can be compromised if this phase is formed. A more serious problem is that pure Pd membranes are extremely sensitive to non-hydrogen contaminants such as H_2S and CO, which can effectively reduce the H_2 flux through the membranes to zero.[3, 4, 8] H_2S is ubiquitous in natural gas and CO is always present in syngas. Poisoning of membranes by these species is thus a critical issue for hydrogen separations from these gas mixtures. The development of practical metal membranes is still required. The general aim of work in this area is to identify materials that simultaneously exhibit high H_2 flux, good thermal stability and chemical stability to resist poisoning by common contaminants.

1.2 Scope of work

One obvious way to improve the performance of pure metal membranes is to use metal alloys.[9] Binary alloys of Pd are widely studied,[10, 11, 12, 13] among which PdCu membranes are of particular interest as they significantly increase the resistance of poisoning to H_2S.[14, 15] These PdCu membranes, however, have lower H_2 flux than pure Pd membranes.[15] One method to increase the H flux through PdCu binary membranes is to decrease the permeation resistance through the membrane. An effective way to achieve this is to use thinner membranes to reduce the bulk diffusion resistance, which is inversely proportional to the thickness of the membrane. An important question that has been examined in my research is the limitations of this method that occur when

bulk diffusion is no longer the rate dominating step in H transport and the net permeation is controlled by surface processes such as desorption.[16] When the membrane is thin enough that the surface processes begin to dominate the permeation, further decreases of the membrane thickness no longer increases the H flux any more.

Another method to improve H flux is to use other materials that have higher H permeability than PdCu binary alloys. Desirable materials should also at least remain the resistance of the contaminants observed in PdCu alloys. In this thesis, I discuss this problem in two different ways. The first one is to use metal sulfides as H_2 purification membranes. I examined several different metal sulfides by predicting their solubility, diffusivity and permeability and compare the results with pure metals. Another approach of this problem is to use PdCu based ternary alloys. PdCuAg alloys are studied in my research, as PdAg binary alloys was proved to increase H permeability compared with pure Pd.[13] I found that adding Ag in PdCu alloys does increase the H permeability, indicating that PdCuAg could be a good candidate as membrane materials.

I have also studied another issue related to H_2 purification that is seldom considered in previous studies, namely the transport of carbon atoms through dense metal membranes. Most studies assume that non-hydrogen species such as carbon and oxygen are unable to permeate through Pd based dense metal membrane. However, experiments with high quality membranes have shown that after long term operation, a carbon layer could form on the permeate side of the membrane. In my study, I have predicted the adsorption and diffusion of carbon in both Pd and Pd based binary alloys, and compared the results with H permeation.

Due to the large time and cost requirement of experimental studies of metal membranes, theoretical predictions have provided an effective alternate approach in the development of practical metal membranes for H_2 purification. First principle calculations, for example, have been used in the past to successfully describe the adsorption and diffusion behavior of hydrogen in the bulk phase of numerous metal and metal alloys as well as on their surface and subsurface layer without any experimental input.[17, 18, 19, 20, 21, 22] Recently Kamakoti and Sholl have developed a theoretical framework to predict macroscopic properties of nonporous H_2 selective membranes using a hierarchical approach based on quantum chemical calculations and coarse grained lattice gas modeling.[15, 19, 23] They have applied their methodology to predict H solubilities and diffusivities in a range of PdCu alloys. The adsorption and diffusion of H in amorphous metals and in metal hydrides were also studied theoretically by Hao and Sholl.[24, 25] Based on these successes, I have used first principle Density Functional Theory (DFT) to approach the topic described in this thesis.

In Chapter II, I first introduce the model to calculate the solubility and diffusivity of hydrogen in my research. In Chapter III I discuss the prediction of surface resistance for PdCu alloys. The rates of the adsorption and desorption on the PdCu surface and diffusion through the bulk phase of PdCu were first determined by first-principle DFT calculations. Then the importance of surface processes were calculated and shown to control the permeation process for thin membranes. The possibility of using metal sulfides is discussed in Chapter III. I have used DFT calculation to characterize the behavior of interstitial H in several different metal sulfides in Chapter IV. The solubilities and diffusivities of hydrogen in those metal sulfides are then calculated based on the

model I introduce in Chapter II. In Chapter V, I have screened a series of PdCuAg alloys by extending Kamakoti and Sholl's method to ternary systems, and compared the results with pure Pd and PdCu binary alloys. Finally, the adsorption and diffusion of carbon in Pd and Pd based alloys is discussed in Chapter VI.

1.3 Reference

[1]L. Schlapbach, A. Zuttel Nature 414 353 (2001)

[2]B. C. Steele, A. Heinzel Nature 414 345 (2001)

[3]D. J. Edlund, D. Friesen, B. Johnson, W. A. Pledger Gas. Separ. Purif. 8 131 (1994)

[4]D. J. Edlund, A. Pledger J. Membr. Sci. 77 255 (1993)

[5]F. Roa, M. J. Block, J. D. Way Desalination 147 411 (2002)

[6]S. Uemiya Sepr. Purif. Tech 22-3 309 (2001)

[7]J. Volkl, G. Alefield *Hydrogen in Metals I* (Springer-Verlag, Berlin, 1978),

[8]N. Lopez, J. K. Norskov Surf. Sci. 477 59 (2001)

[9]S. N. Paglieri, J. D. Way Sep. Purif. Methods 31 1 (2002)

[10]F. Roa, J. D. Way Ind. Eng. Chem. Res. 42 5827 (2003)

[11]F. Roa, J. D. Way, R. L. McCormick, S. Paglieri Chem. Eng. J 93 11 (2003)

[12]B. H. Howard, R. P. Killmeyer, K. S. Rothenberger, A. V. Cugini, B. D. Morreale, R. M. Enick, F. Bustamante J. Membr. Sci. 241 207 (2004)

[13]G. L. Holleck J. Phys. Chem. 74 503 (1970)

[14]B. D. Morreale, M. V. Ciocco, B. H. Howard, R. P. Killmeyer, A. Cugini, R. M. Enick J. Membr. Sci. 241 219 (2004)

[15]P. Kamakoti, B. D. Morreale, M. V. Ciocco, B. H. Howard, R. P. Killmeyer, A. V. Cugini, D. S. Sholl Science 307 569 (2005)

[16]T. L. Ward, T. Dao J. Membr. Sci 153 211 (1999)

[17]J. Greeley, M. Mavrikakis J. Phys. Chem. B 109 3460 (2005)

[18]J. Greeley, W. R. Krekelberg, M. Mavrikakis Angew. Chem. Ind. Ed. 43 4296 (2004)

[19]P. Kamakoti, D. S. Sholl Phys. Rev. B 71 014301 (2005)

[20]D. S. Sholl J. Alloys. Comp. 446 462 (2007)

[21]B. Bhatia, X. J. Luo, C. A. Sholl, D. S. Sholl J. Phys: Conden. Matter 16 8891 (2004)

[22]D. E. Jiang, E. A. Carter Phys. Rev. B 70 064102 (2004)

[23]P. Kamakoti, D. S. Sholl J. Membr. Sci. 225 145 (2003)

[24]S. Q. Hao, D. S. Sholl J. Chem. Phys. 130 244705 (2009)

[25]S. Q. Hao, D. S. Sholl Appl. Phys. Lett. 94 171909 (2009)

Chapter II Models and methods

In this chapter, I discuss how to determine the H flux through dense metal membranes. I present a statistical mechanical model based on first principles calculations to predict interstitial H solubility in metal alloys. I also show how to perform Kinetic Monte Carlo (KMC) simulations to predict H diffusivity in disordered materials, and how to calculate the H diffusivity in ordered materials based on the theory given by Braun and Sholl.[1]

2.1 H permeability through dense metal membranes

The ability of a membrane to transport hydrogen is typically quantified in terms of permeability, permeance or flux. The H flux through a membrane, J, is obtained from Fick's first law as the product of the diffusion coefficient and the concentration gradient across the membrane:

$$J = -D\frac{C_{feed} - C_{per}}{L} \qquad (2.1)$$

where D and L are the diffusion coefficient and membrane thickness respectively. C_{feed} and C_{per} are the H concentration in the metal layers immediately adjacent to the surface on the feed and permeate side respectively. I will use this description to model membranes defined by dense metal film of homogeneous composition in which H transport through grain boundaries or other defects can be neglected.

For thick membranes, the rate limiting step is the transport of H atoms through the membrane.[2] In this situation, the surface reaction is rapid enough for the dissolved H

atoms at the surface to be in equilibrium with gaseous H_2 on either side of the membrane. Under these circumstances, the dilute H concentration in metals and alloys follows Sieverts' law,[3] and the flux through the membrane can be written as

$$J = DK_s \frac{P_{feed}^{0.5} - P_{per}^{0.5}}{L} \qquad (2.2)$$

Here, P_{feed} and P_{per} are the partial pressure of gaseous H_2 on the feed and permeate side respectively, K_s is the Sieverts' constant, which I will discuss later. The H permeability, k, is defined as

$$k = \frac{JL}{P_{feed}^{0.5} - P_{per}^{0.5}} \qquad (2.3)$$

Therefore, if the permeation process is dominated by the diffusion of interstitial H through the bulk of the membrane, the permeability, k, can be written as a product of the Sieverts' constant and the diffusion coefficient

$$k = DK_s \qquad (2.4)$$

If the flux is expressed in terms of moles of H_2 rather than the moles of H, then $k=0.5DK_s$. This expression indicates that the permeability, k, is a function of temperature and independent of other operating conditions such as the thickness of the membrane or the feed and permeate pressure at each side. However, as I will discuss in details in Chapter III, when the permeation is dominated by the surface processes, Eq. (2.4) is no longer valid to describe the permeability. In this situation, the permeability is defined by Eq. (2.3), provided that the value of J in this expression accounts for all resistances to H transport that are relevant in the membrane.

2.2 Statistical mechanical model for H solubility in the membranes

Eq. (2.4) shows that for thick membranes the permeability of H can be expressed as a product of the solubility and the diffusivity. In the following two sections, I discuss how to obtain K_s and D from first principle calculations. I first begin with H solubility. Hydrogen dissolves in metal alloys via dissociative absorption of molecular H_2, which can be written as:

$$H_2(g) \longleftrightarrow 2H(a) \qquad (2.5)$$

The above equation corresponds to a situation where H atoms dissolved in a metal/alloy are in equilibrium with gaseous H_2 in the neighboring gas phase having a partial pressure P. I define the concentration of H atoms, θ, as the ratio of the number of H atoms dissolved to the total number of metal atoms in the system. The solubility of H in metals and alloys at dilute concentrations follows Sieverts' law, [3]

$$\theta = K_s P^{0.5} \qquad (2.6)$$

where K_s is the Sieverts' constant.

Eq. (2.6) is only valid for the dilute concentrations of interstitial H solutions. For example, Sieverts' Law is accurate for hydrogen dissolving in Pd at the temperature ranges 873-1473 K and pressures up to 1 atm.[4] These conditions lead to the so-called α-PdH phase, where the low concentration of H atoms in the Pd interstitial sites are disordered. As T is lowered below 873 K or the pressure is raised, deviations are observed due to appearance of an ordered β-PdH phase. In my later calculations, the calculated solubility is always smaller than 0.1, which suggests that Sieverts' law is valid in my systems.

Kamakoti and Sholl developed a comprehensive model to predict hydrogen

solubilities at dilute loadings using a combination of atomic scale first principles calculations and statistical thermodynamic modeling.[5, 6, 7] The resulting model is valid over a wide range of temperatures, pressures and different materials. In this approach, the chemical potential for H atoms, μ_H , is equated to the H_2 chemical potential, μ_{H_2} , by

$$\frac{1}{2}\mu_{H_2(g)} = \mu_{H(a)} \qquad (2.7)$$

Molecular H_2 is treated as an ideal gas, an accurate approach for a wide range of pressures at elevated temperatures. The chemical potential of an ideal gas at constant volume, V, and temperature, T, is: [8]

$$\mu_{H_2} = k_b T \ln[\frac{qk_bT}{V}] \qquad (2.8)$$

where k_b is Boltzmann's constant. The partition function for a diatomic ideal gas is:[8]

$$\frac{qk_bT}{V} = (\frac{2\pi mk_bT}{h^2})^{1.5}\frac{8\pi^2 Ik_bT}{\sigma h^2}\frac{\exp(-\beta h\nu_{H_2}/2)}{1-\exp(-\beta h\nu_{H_2}/2)}e^{\beta D_E} \qquad (2.9)$$

Here, m is the molecular mass of H_2, h is Planck's constant, I is the molecular moment of inertia, σ is the symmetry number for the molecule, $\beta = 1/k_bT$, ν_{H_2} is the vibrational frequency of the molecule and D_E is the molecular dissociation energy. Eq. (2.9) treats the vibrational degrees of freedom of H_2 as harmonic. The known quantities for H_2 are: m=3.32×10^{-27} kg, ν_{H_2} =6.48×10^{-13} s^{-1}, σ =2 and I=4.67×10^{-48} kg • m^2.

To determine the chemical potential of interstitial atomic H, μ_H, I assume that the interstitial sites in the metal can be treated as independent three-dimensional harmonic oscillators with binding energy defined with respect to gaseous H_2, E_b, and average vibrational frequency, ν_H . The chemical potential of absorbed H, μ_H , can be obtained from the Helmholtz free energy using

$$A = -k_b T \ln Q \tag{2.10}$$

and

$$\mu_H = (\partial A / \partial N_H)_{V,T} \tag{2.11}$$

where Q is the total partition function for the dissolved H atoms. For a system of N_H absorbed H atoms dissolved in a total of N_s available sites, Q can be written as [4]

$$Q = \frac{N_s!}{(N_s - N_H)! N_H!} q_1^{N_H} \tag{2.13}$$

Here q_1 is the partition function for an individual H atom in the metal, where [4]

$$q_1 = \frac{\exp(-\beta(E_b + 1.5h\nu_H - 0.5D_E))}{\prod_{i=1}^{3}(1-\exp(-\beta h\nu_{H,i}))^3} \tag{2.14}$$

If I substitute $\theta = N_H / N_s$ into Eq. (2.13) and equate Eq. (2.7) - (2.14), I can express the Sieverts' constant, $K_{s,i}$, as:[5]

$$K_{s,i} = \exp(\beta(-E_b - 1.5h\nu_H + 0.25h\nu_{H_2}))\frac{1}{\sqrt{\alpha}}\frac{\sqrt{1-\exp(-\beta h\nu_{H_2}/2)}}{\prod_{i=1}^{3}(1-\exp(-\beta h\nu_{H,i}))^3} \tag{2.15}$$

where

$$\alpha = \left(\frac{2\pi m k_b T}{h^2}\right)^{3/2} \frac{8\pi^2 I (k_b T)^2}{2h^2}.$$

Eq. (2.15) gives the H solubility at one interstitial site with binding energy E_b and vibrational frequency ν_H. The subscript i in Eq. (2.15) indicates that there are three vibrational frequencies for the interstitial H. The net Sieverts' constant for the material K_s, is obtained by summing $K_{s,i}$ over the all possible individual sites, that is,

$$K_s = \sum K_{s,i} \tag{2.16}$$

The model described above has similarities to previously reported work by Fowler et al. and Lacher.[4, 9] However, the critical difference lies in the manner used to describe the unknown quantities, the binding energy E_b and vibrational frequency ν_H. I show later how first principles calculations can be used to accurately determine these quantities without using any experimental input.

2.3 Methods to calculate H diffusivity

2.3.1 Individual hopping rate

The migration of H atoms in metals and alloys can proceed via several possible mechanisms, one of them dominating others in a given range of temperature.[10, 11] In the lowest temperature region, where practically no phonons are present, H atoms are expected to migrate via coherent tunneling. As the temperature is raised, the H atom will be localized about a specific interstitial site. The elementary step of this diffusion process is now a thermally activated jump which H may execute by tunneling from one site to another or by hopping over the potential barrier. In the first case, thermal activation is required to equalize the energy levels of both sites to the same height. In the second case, a higher activation energy is required to overcome the barrier. Finally, at extremely high temperatures, H motion proceeds via a "fluid like diffusion" where the interstitial will be mainly at states above the potential barrier. At moderate and high temperatures, the over-barrier jumps of H atoms from one equilibrium site to another are expected to be dominant. Tunneling contributions to H transport are known to be negligible except at cryogenic temperatures.[12, 13]

In my study, I am interested in how H diffuses at temperatures of 600 K-1200 K.

In this region, thermally activated jumps between interstitial sites over the potential barrier dominate the diffusion process. For H hopping over the potential barrier, the individual hopping rate from site *i* to site *j* can be obtained from the classical transition state theory as

$$k_{ij} = \frac{k_b T}{h} \frac{q_{TS}}{q_i} e^{-\beta E_a} \tag{2.17}$$

where q_i and q_{TS} are the canonical partition functions at site *i* and the transition state (TS) for this hopping, respectively. E_a is the classical activation barrier, defined as the energy difference between site *i* and TS. If I model H atoms as three dimensional classical harmonic oscillators, the partition function for this system is [8, 14, 15]

$$q_i = \prod_{m=1}^{3} \frac{k_b T}{h \nu_i^m} \tag{2.18}$$

The partition function for the H atom at a TS can similarly be written with a loss of one degree of freedom at the saddle point as

$$q_{TS} = \prod_{m=1}^{2} \frac{k_b T}{h \nu_{TS}^m} \tag{2.19}$$

The classical rate theory expression can be modified by replacing the classical partition functions in Eq. (2.18) and (2.19) with their quantum mechanical counterparts. The partition function for a three dimensional quantum mechanical harmonic oscillator at an O site can be written as [16]

$$q_i^{qc} = \prod_{m=1}^{3} \frac{1}{2 \sinh(h\nu_i^m / 2k_b T)} \tag{2.20}$$

A similar expression can be written for the partition function at a TS. The hopping rate for H motion from site i to j, k_{ij}, using transition rate theory can then be written as [14]

$$k_{ij} = \frac{\prod_{m=1}^{3} f(h\nu_i^m / 2k_bT)\nu_i^m}{\prod_{m=1}^{2} f(h\nu_{TS}^m / 2k_bT)\nu_{TS}^m} e^{-\beta E_a} \qquad (2.21)$$

where $f(x)=\sinh(x)/x$.

The model summarized above defines the local hopping rates of interstitial H atoms. To predict the net H diffusivity, this information about the localized hopping rates has to be linked with the long range H transport in the materials of interest. A description of H diffusion in metals can be modeled based on the lattice-gas model. This model assumes that atoms occupy fixed lattice sites and can undergo jumps to other vacant sites with some probability. Two kinds of structures exist in my research: ordered structures, for crystals, such as pure Pd or metal sulfides, and the disordered structures like PdCu alloys. In my study, a disordered structure still defines a fixed ordered lattice. The atoms of different chemical species in the material, however, are randomly located on the lattice. Below I show how I obtain the diffusivity with the technique given by Braun and Sholl for ordered materials[1] and kinetic Monte Carlo (KMC) simulations for disordered materials.[7] I aim to use these techniques to get the self-diffusivity of hydrogen in different materials (metal sulfides, metal alloys, etc). At dilute concentration, the self-diffusivity equals the transport diffusivity, which I used to calculate the H flux and H permeability (Eq. (2.4).[17] In my calculations, the H concentration is usually smaller than 0.1. It indicates that the self diffusivity obtained as I discuss below can be directly used to get the permeability without any further modifications.

2.3.2 Diffusion in an ordered structure

I first look at diffusion in an ordered structure with finite number of interstitial sites in the unit cell. In an ordered structure, the sites in a periodic structure with s sites per unit cell may be labeled by two indices l and a, where l labels the elementary cell and a labels the different sites within the cell, a=1,…,s. The equilibrium occupation numbers at each site, ρ_a, should satisfy the Boltzmann distribution at dilute concentrations:

$$\rho_a = e^{-\beta\varepsilon_a} / \sum e^{-\beta\varepsilon_a} \tag{2.22}$$

where ε_a is the site energy at site a.

To get the diffusion coefficient in an ordered structure, I define the transfer matrix as

$$\Delta_{l,a;l',a'} = \delta_{ll'}\delta_{aa'}\sum_{l'',a''} k_{l'',a'';l',a'} - k_{l,a;l',a'} \tag{2.23}$$

where $k_{l,a,l',,a'}$ is the jump rate from site (l,a) to site (l',a'). From the periodicity of the lattice, $\Delta_{l,a;l',a'}=\Delta_{l-l',a,0,a'}$. A new matrix $\Lambda(\mathbf{k})$ can then be introduced as:

$$\Lambda_{a;a'}(\mathbf{k}) = \rho_a^{-1/2}(\sum_{l} \exp[i\mathbf{k}(l-l_0)]\Delta_{l,a;l_0,a_0})\rho_{a'}^{1/2} \tag{2.24}$$

The Taylor expansion of $\Lambda(\mathbf{k})$ is:

$$\Lambda(\mathbf{k}) = \Lambda_0 + \Lambda_1(\mathbf{k})k_x + \frac{1}{2}\Lambda_2(\mathbf{k})k_x^2 \tag{2.25}$$

where

$$\Lambda_0 = \lim_{\mathrm{k}->0}\Lambda(\mathbf{k})$$

$$\Lambda_1 = \lim_{\mathrm{k}->0}\frac{\partial}{\partial k_x}\Lambda(\mathbf{k}) \quad .$$

$$\Lambda_2 = \lim_{\mathrm{k}->0}\frac{\partial^2}{\partial k_x^2}\Lambda(\mathbf{k})$$

Braun and Sholl showed that for a periodic structure, the solution of the master equation

associated with the transfer matrix defined above leads to an expression of the diffusivity D_{xx} as:[1]

$$D_{xx} = v_0^* \Lambda_1 v_1 + \frac{1}{2} v_0^* \Lambda_2 v_0 \tag{2.26}$$

where v_0 and v_1 are two vectors obtained as:

$$\begin{aligned} &(v_0)_a = \rho_a^{1/2} \\ &\Lambda_0 v_1 + \Lambda_1 v_0 = 0 \end{aligned} \tag{2.27}$$

In my studies, I first applied first-principle calculations to obtain the binding energies in all interstitial sites, and the energies in all transition states for site to site hoppings among these sites. The site to site jumping rate can be obtained from Eq. (2.11), as described in Sec. 2.3.1. The transfer matrix is then obtained from Eq. (2.23), given how the sites are connected in a unit cell and all jump rates between those sites. The diffusivity is then found from by solving Eq.(2.25-2.27).

The above technique gives an accurate description of the diffusivity in an ordered structure at low concentration. This method cannot, however, be applied to substitutionally disordered materials, since no periodic unit cell can be found for these materials. In this case a different approach is required to determine interstitial diffusion coefficient. This approach is described in the next section.

2.3.3 Kinetic Monte Carlo (KMC) simulations

In general, I used kinetic Monte Carlo (KMC) simulations to obtain the diffusivity of H in disordered systems. KMC simulations are well suited to stochastically modeling a system defined by discrete events with known rates, in this case a series of activated jumps between adjacent sites.[18, 19] In KMC simulations, the short-time dynamics of

the system are replaced by discrete hops in a lattice. The available sites in the lattice are associated with the minima in the energy landscape. The energy of the lattice site and the hopping rate between sites are typically defined in terms of the local environment around the state such as number, position and chemical identity of surrounding atoms.

I am interested in measuring the H diffusivity in Pd-based metal alloys. These alloys have a disordered fcc structure. Two kinds of interstitial sites exist in a fcc lattice: the octahedral site (O) and the tetrahedral site (T). The jump rates between O site and T site can be evaluated using Eq. (2.21) via quantum modified harmonic transition state theory.[7] The following KMC algorithm is then used to follow the time evolution of non-interacting H atoms in disordered alloys. [7]

1. Define a simulation volume consisting of randomly arranging the atoms of the alloy at the desired composition.
2. Scan through the entire simulation volume to identify the fastest rate of hopping within all possible hops in the volume, identified as k_{fast}.
3. Randomly position N_H H atoms among the volume in O sites.
4. At each time step in my KMC an interstitial H is randomly selected from all the H atoms that have been placed in the simulation volume. Next a move direction is chosen randomly from the 8 (4) possible directions available for an O (T) site.
5. Hops are accepted depending on the direction of the hop
    a. O site to T site hops are accepted with probability $2k_{OT}/k_{fast}$
    b. T site to O site hops are accepted with probability k_{TO}/k_{fast}

    The factors in these acceptance probabilities arise from the different number of hopping directions available to the different types of possible hops.

6. Regardless of the outcome of the attempted hop, time is incremented by $\Delta t = 1/\left(4N_H k_{fast}\right)$, where N_H is the total number of interstitial H atoms in the simulation volume.

It is straightforward to show that this algorithm correctly defines the local hopping rates of all possible processes in my lattice model. I have not included site blocking effects in my simulations since I am working with dilute H concentrations. These effects could easily be incorporated in these simulations if simulations of concentration-dependent diffusion were of interest.

My simulation volume consisted of 4,631 metal atoms randomly distributed in an fcc lattice representing the composition of interest. In each simulation, 150 H atoms were randomly distributed in the O sites of the simulation volume. A large number of KMC steps (typically 50,000 steps per H atom) were used to thermally equilibrate the system. After equilibration a further 500,000 MC steps per H atom were performed while collecting data on the trajectory of each atom. After observing a large number of hops in a KMC simulation, the mean square displacement of each H atom is calculated. After correcting for passage across the periodic boundaries, the self diffusivity, D_s, is determined using an Einstein expression relating the diffusivity to the mean square displacement.[20]

$$D_s = \lim_{t->\infty}\left[\frac{1}{6Nt}\sum_{t=1}^{N}\sum_{i=1}^{N_H}|\,R_i(t)-R_i(0)\,|^2\right] \qquad (2.28)$$

Here, the vector $R_i(t)$ determines the position of atom i at time t.

2.4 Density Functional Theory

In the previous sections, I have shown how to calculate the net solubility and diffusivity of H in dense metal membranes. The inputs in these methods are the binding energies, vibrational frequencies of H at the interstitial sites and the transition states. I used plane wave Density Functional Theory (DFT) to calculate the binding energy and vibrational frequencies for atomic H without any experimental input. DFT is a first principles theory of electronic ground-state structure based on the electronic density distribution. DFT can be used for the understanding and calculation of ground state electron density and total energy of any system consisting of nuclei and electrons. In principle, it can be applied to all atoms in the periodic table, and can be used for systems involving metallic, covalent and ionic bonds. DFT can be used to model isolated molecules and phenomenon occurring in bulk solids and extended surfaces such as adsorption and absorption. A large number of studies have shown that DFT is quantitatively accurate for describing the potential energy surface of H atoms adsorbed in metals and metal surfaces,[21, 22, 23, 24] the diffusivity of H in amorphous metals and metal hydrides,[25, 26] the tunneling jump rate of H at very low temperatures[13] and the free energies for solid phase hydride reactions.[27, 28, 29] In my studies, some preliminary calculations were done for Pd-H systems in order to examine the accuracy of DFT calculations in my system. For example, DFT gave a lattice constant 3.960 Å for pure Pd, in good agreement with the experimental measurements of 3.890 Å. The classical binding energy and zero point energy of H in an O site in pure Pd was calculated to be -0.16 eV and 0.09 eV, respectively, while the experiments gave -0.12 eV and 0.07 eV, respectively.[6] Previously, Kamakoti and Sholl showed that DFT calculations,

combined with a lattice gas model and the methods I introduced above, gave a good prediction for the solubility and diffusivity of H in PdCu binary alloys.[5, 6, 7] In the following chapters, I discuss in details how to apply DFT calculations, together with the models introduced above, to obtain the macroscopic properties of H in different materials.

2.5 Reference

[1]O. M. Braun, C. A. Sholl Phys. Rev. B 58 14870 (1998)

[2]T. L. Ward, T. Dao J. Membr. Sci 153 211 (1999)

[3]G. Alefeld, J. Volkl *Hydrogen in Metals II* (Springer-Verlag, Berlin, Heidelberg, New York, 1978),

[4]J. R. Lacher Proc. Roy. Soc. A 161 525 (1937)

[5]P. Kamakoti, B. D. Morreale, M. V. Ciocco, B. H. Howard, R. P. Killmeyer, A. V. Cugini, D. S. Sholl Science 307 569 (2005)

[6]P. Kamakoti, D. S. Sholl J. Membr. Sci. 225 145 (2003)

[7]P. Kamakoti, D. S. Sholl Phys. Rev. B 71 014301 (2005)

[8]D. A. McQuarrie *Statistical Mechanics* (University Science Books, 2000),

[9]R. H. Fowler, C. J. Smithells Proc. Roy. Soc. A 160 37 (1937)

[10]G. Alefeld, J. Volkl *Hydrogen in Metals I* (Springer-Verlag, Berlin, Heidelberg, New York, 1978),

[11]D. Richter Springer Tracts in Modern Physics 101 85 (1983)

[12]K. Haug, T. Jenkins J. Phys. Chem. B 104 10017 (2000)

[13]B. Bhatia, D. S. Sholl Phys. Rev. B 72 224302 (2005)

[14]L. Katz, M. Guinan, R. J. Borg Phys. Rev. B 4 330 (1971)

[15]G. H. Vineyard J. Phys. Chem. Solids 3 121 (1957)

[16]R. Kircheim, R. B. Mclellan Acta. Metall. 28 1549 (1980)

[17]D. S. Sholl Acc. Chem. Res. 39 403 (2006)

[18]R. M. Nieminen J. Phys.:Condens. Matt. 14 2859 (2002)

[19]C. Uebing, R. Gomer J. Chem. Phys. 100 7759 (1994)

[20]D. S. Sholl Ind. Eng. Chem. Res. 39 3737 (2000)

[21]A. Gross, S. WIlke, M. Scheffler Phys. Rev. Lett. 57 2493 (1995)

[22]O. M. Lovvik, R. A. Olsen Phys. Rev. B 58 10890 (1998)

[23]O. M. Lovvik, R. A. Olsen J. Alloys. Compounds. 330-332 332 (2002)

[24]Z. Sljivancanin, B. Hammer Phys. Rev. B 65 085414 (2002)

[25]S. Q. Hao, D. S. Sholl Energy Envir. Sci. 1 175 (2008)

[26]S. Q. Hao, D. S. Sholl J. Phys. Condens. Matter 21 115402 (2009)

[27]S. V. Alapati, J. K. Johnson, D. S. Sholl J. Phys. Chem. C 11 6910 (2007)

[28]S. V. Alapati, J. K. Johnson, D. S. Sholl Phys. Chem. Chem. Phys. 9 1438 (2007)

[29]S. V. Alapati, J. K. Johnson, D. S. Sholl J. Phys. Chem. C 112 5258 (2008)

Chapter III. Evaluation of the surface resistance for H permeation through PdCu alloys

One key technical issue in choosing metal alloys for separating H_2 from other gases is to find alloys with H permeability comparable to pure Pd, or even higher than Pd. Recent research efforts have been focused on screening different alloys components and compositions. Many Pd based binary alloys including PdAg and PdCu have been studied widely,[1, 2, 3] and more limited efforts have been made to examine alloys with three or more components.[4] Another method to increase H permeability is to fabricate thinner membrane layers, which would allow higher permeation rates or reduced membrane surface area requirements, both of which impact economic feasibility. However, using thinner membranes also means that surface process such as adsorption and desorption might play a more important role during the permeation, as has been indicated experimentally in pure Pd and some Pd based alloys.[5, 6, 7, 8] In this chapter, I will discuss how surface processes affect the permeation rate of H_2 through metal alloy membranes using first principles calculations. A general method is established to evaluate the surface resistance for PdCu and other alloys.

3.1 Introduction

H permeation through a metal membrane can be divided into several steps, as shown in Fig. 3.1. A hydrogen molecule first adsorbs on the metal surface dissociatively. Then, atomic hydrogen moves from the surface to the bulk of the material, diffuses in the bulk through the interstitial sites, moves from the bulk to the downstream surface and

finally recombinatively desorbs from the surface as gaseous hydrogen molecules. In many circumstances, interstitial diffusion is the rate-limiting step in this multi-step process. The flux of H_2, J, dominated by the interstitial diffusion can be described via Fick's law as:

$$J = -D\frac{\Delta c}{L} \tag{3.1}$$

Here D is the diffusivity of hydrogen in the membrane. L is the thickness of the membrane and Δc is the concentration difference between the feed side and the permeate side. At dilute interstitial concentration, the concentration of hydrogen in the metal can be directly related to the pressure by Sieverts' Law. In this case, Eq. (3.1) can be rewritten as:

$$J = -DS\frac{P_{feed}^{0.5} - P_{per}^{0.5}}{L} \tag{3.2}$$

Here, S is the Sieverts' constant which is a function of temperature and P_{feed} (P_{per}) is the hydrogen pressure at the feed side (permeate side), correspondingly. In both Eq. (3.1) and Eq. (3.2), the H flux through a membrane is inversely proportional to the membrane film thickness. This observation has driven a great deal of work in the field that aims to reduce membrane thicknesses. Metal membranes with thicknesses on the order of a few microns are now routinely fabricated, and methods to reduce this thickness continue to be developed.[9]

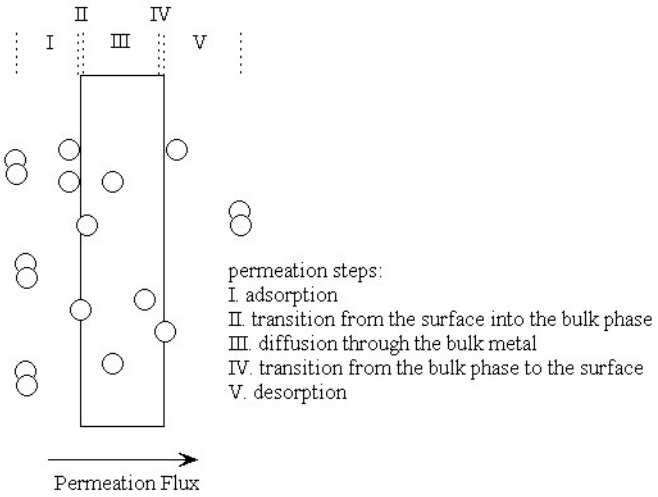

Figure 3.1: Schematic illustration of the H_2 permeation process through a dense metal membrane. Circles: H atoms and molecules.

The assumption that H_2 permeation rates are controlled solely by diffusion in the bulk of the membrane is, however, only valid for sufficiently thick membranes. The dissociation and recombination processes that occur on membrane surfaces also define resistances to mass transport, and as membrane thicknesses are reduced, these surface resistances may play an important role in the overall performance of a membrane. A number of previous studies have shown this phenomenon. McCool and Lin performed experiments with PdAg membranes with submicron thicknesses, and concluded that the bulk diffusion resistance was only dominant for temperatures higher than 200 °C.[5] Zhang et al. compared microfabricated Pd membranes with thicknesses of several microns and found that hydrogen permeation through these membranes was ~50% of that for a relatively thick membrane for temperatures of 200–400 °C.[7] Other groups reported deviations from diffusion dominated behavior for 1 μm thick PdTa membranes[8] or for

membranes operated below 350 °C.[6] These deviations were attributed to the influence of surface processes.[6, 8]

A detailed model that accounts for the existence of surface resistances in pure Pd membranes was developed by Ward and Dao.[10] This model explicitly includes adsorption and desorption of H_2 from the membrane surfaces, hopping of H between surface sites and subsurface sites, and interstitial diffusion within the metal. The parameters necessary for implementing this model were taken from the large body of surface science and membrane experiments that have been performed for pure Pd and its surfaces. In agreement with the experiments of Zhang et al. and with earlier experiments, Ward and Dao's model predicted that bulk diffusion would dominate the performance of pure Pd membranes at temperatures higher than ~300 °C and membrane thicknesses larger than ~10 μm.[10]

To apply Ward and Dao's model to pure Pd or any other membrane material, a large number of rate parameters must be known or estimated. Many of these parameters are associated with rates occurring on the membrane's surfaces. Because experiments of many different kinds have been performed for Pd surfaces, reliable values for these parameters were available. Unfortunately, the same is not true for the large range of alloys that have been considered as possible alternatives to pure Pd as membrane materials. In the following sections, I will show how first-principles calculations can be used to obtain these parameters for metal alloys of interest, allowing us to make detailed predictions for the importance of surface resistances in membranes made from these alloys. A number of recent studies have used first-principles methods to characterize H_2 permeation through metal alloys,[11-15] but in each case the focus has been on interstitial

transport within the membrane material. In this chapter, I discuss first extension of these methods to include surface resistance effects.

3.2 Model description

My model for the permeation of H_2 through a metal membrane closely follows the work of Ward and Dao.[10] This approach describes a membrane that is simplified in several important ways from practical membranes. First, I treat the membrane as an unsupported, defect-free metal film. This implies that both the upstream and downstream surfaces of the membrane are defined by the membrane material and that contributions to transport due to grain boundaries or other defects are not considered. Most practical thin film membranes include a porous support layer for mechanical stability, and this layer and the interface between the support and the metal film can introduce additional transport resistances that are not described in my model. Multi-scale models that include the effects of support resistances in inorganic membranes have been explored in other contexts.[8] Second, I assume that both the feed and permeate gases around the membrane are pure H_2, which means that chemical contamination of the membrane surfaces is not considered. The performance of membranes when using mixed gas feeds that include possible chemical contaminants is of course important in the practical application of metal membranes. Nevertheless, membrane permeance when using pure H_2 is a useful quantity for making initial comparisons between potential membrane materials. Finally, I assume that the gas in the feed and permeate regions are well mixed, so no transport resistances arise from gas phase transport. Ward and Dao discussed this issue in a more detailed way. My overall microkinetic description of H_2 permeation through a

metal film includes contributions from bulk diffusion in the membrane, recombinative desorption and dissociative adsorption of H_2 on the membrane surface, and hopping of H between surface and subsurface sites. Below, I define the fluxes associated with each of these processes.

3.2.1 Diffusion of atomic H through the bulk phase of PdCu alloys

Previous studies revealed that the adsorbed hydrogen atoms occupy the interstitial sites in the bulk phase of Pd based alloys.[12, 13] The net flux due to diffusion through the bulk of the membrane is defined via Eq. (3.1). When the interstitial concentrations are low, which is known to be the case for PdCu alloys at the conditions I will consider,[12, 13] the concentration c can be related to the interstitial H concentration as

$$c = N_b X \tag{3.3}$$

and Eq. (3.1) becomes

$$J = -DN_b \frac{\Delta X}{L} \tag{3.4}$$

Here, X is the probability that an interstitial is occupied by H and N_b is the density of metal atoms in the alloy (in units of mol/m^3). If interstitial concentrations were large inside a membrane, this description would need to account for the concentration dependence of the interstitial diffusion coefficient.[16]

Kamakoti and Sholl have previously used first-principles calculations to predict the solubility and diffusivity of H in PdCu alloys as functions of alloy composition and temperature.[11, 12, 13] These calculations make predictions that are in good agreement with the experimental data that is available for these alloys.[11] In order to predict the diffusivity of H in a disordered alloy, Kamakoti and Sholl performed a large number of

density functional theory calculations characterizing individual hops between adjacent interstitial sites in PdCu alloys, then used kinetic Monte Carlo simulations to connect these individual events with net diffusive transport. I used the temperature dependent diffusion coefficients calculated by Kamakoti and Sholl for the alloys I considered without further modification.[13]

3.2.2 Surface desorption and adsorption

The flux of H_2 molecules leaving a metal surface by recombinative desorption can be expressed as:[10]

$$J = k_0 e^{-\frac{E_{des}}{k_b T}} P_{11} N_s^{\,2} \qquad (3.5)$$

Here, k_0 and E_{des} are the pre-exponential factor and activation energy for the desorption of a pair of H atoms from neighboring adsorption sites on the surface, P_{11} the probability that both sites are occupied by H atoms, and N_{s} is the density of metal atoms on the surface (in units of mol/m^2).On a defect-free pure Pd surface, every surface site is equivalent. On an alloy surface, however, the binding energy of H atom on the surface varies according to the identities of the metal atoms around the binding site, so k_0, E_{des}, and P_{11} must be defined in a way that accounts for this spatial heterogeneity. I will describe how I use first-principles calculations to provide the information that is necessary to accomplish this task in the following section.

As the dissociative adsorption of hydrogen on the surface is the reverse of recombinative desorption, the adsorption and desorption rates are equal at equilibrium. At the same time, since the dissociative adsorption involves two adjacent empty sites on the surface, the adsorption rate is proportional to the probability that adjacent sites are empty,

P_{00}. As a result, under steady state but non-equilibrium conditions, the net flux onto a surface due to adsorption can be expressed as

$$J = J_{des}^{eq}(P_{00} / P_{00}^{eq}) \qquad (3.6)$$

Here J_{des}^{eq} is the equilibrium desorption rate at the same gas phase pressure and is the probability of two adjacent sites being empty at the equilibrium surface coverage corresponding to this pressure. To use this expression in a practical calculation, the surface adsorption isotherm and the neighboring site probability functions must be known. I will describe how first-principles calculations can be used to determine these quantities in the following paragraphs.

3.2.3 Transition between surface and subsurface layers

To describe the net flux of H atoms from the membrane surface on the feed side to adjacent subsurface interstitial sites, I follow the approach of Ward and Dao [10].

$$J = \beta_0 e^{-E_{a,1}/k_b T}(1 - X_s)\theta_s N_s N_b \qquad (3.7)$$

In this equation, β_0 and $E_{a,1}$ are the pre-exponential and activation energy barrier for hopping from a surface site to a subsurface interstitial site, θ the probability that the surface site is occupied by H and X_s is the probability that the subsurface site is occupied. This mean-field expression is accurate in instances where X_s is much less than 1, as it is in the materials I consider. In a full treatment of this flux, this expression should be used with separate rate constants for each distinct binding site on the spatially heterogeneous surface defined by an alloy.

I treat the net flux of H atoms from subsurface interstitial sites to surface sites on the permeate side of the membrane in a similar way [10]. That is, this flux is expressed as

$$J = \nu_0 e^{-E_{a,2}/k_b T} X_s (1 - \theta_s) N_s N_b \qquad (3.8)$$

Here, ν_0 and $E_{a,2}$ are the pre-exponential and activation energy barrier for hopping from a subsurface site to a surface site.

Once all the rate parameters in the individual fluxes defined above are known, the overall permeance of H_2 through a membrane can be calculated as a function of the feed pressure, trans-membrane pressure drop, and temperature. My approach to this calculation is similar to the method used by Ward and Dao[10]. By fixing the feed pressure (P_{feed}), I choose an arbitrary flux and calculate the corresponding permeate pressure (P_{per}). If the calculated permeate pressure does not match the desired permeate pressure, the flux value is updated to achieve a closer match between the calculated and desired value. This iterative process is continued until the difference between the calculated and target permeate pressure is less than 10^{-5} atm.

3. 3 First-principles calculations for $Pd_{75}Cu_{25}$(1 1 1) surfaces

All of my calculations were performed for $Pd_{75}Cu_{25}$, a binary alloy that has been studied experimentally because of its apparent resistance to sulfur poisoning [11]. The alloy has a random fcc crystal structure, so it is also a good example for exploring the technical issues that exist when performing first-principles calculations for disordered alloys. The properties of this bulk alloy have been extensively studied using DFT-based methods [11-13]. My calculations focused on the surface properties of this material, since this information is needed to use the description of surface resistances defined above. All of my surface calculations used the (111) surface, the closest packed surface of fcc metals. DFT calculations were performed using the Vienna *ab initio* simulation package (VASP)

using the generalized gradient approximation with the PW91 functional to describe electron exchange-correlation effects.[17] Ion–electron interactions were described by the ultrasoft pseudopotentials. A plane-wave expansion with a cut-off of 234.0 eV was used in all calculations. Geometry relaxations are performed with a conjugate gradient method algorithm until the forces on all unconstrained atoms were less than 0.03 eV/Å. My calculations examined (4×4) surface unit cells with a 3×3×1 Monkhorst–Pack *k*-points mesh.

My calculations used a slab containing fmy metal layers with a total of 48 Pd atoms and 16 Cu atoms in the computational supercell. Cu and Pd atoms within each layer were distributed randomly on the sites of the fcc structure. A vacuum space corresponding to seven metal layers was used to separate the slab and its periodic images along the surface normal. The top two layers of the slab were relaxed while the bottom two layers were fixed with the calculated equilibrium lattice constant, a_0, for the bulk alloy, 3.897Å. Adsorption was allowed on the relaxed side of the slab only.

Transition states for diffusion of H were determined using the Nudged Elastic Band (NEB) method [18]. The vibrational frequencies of local minima and transition states were calculated in the harmonic approximation by assuming that localized vibrations of H atoms are decoupled from vibrations of the metal atoms. This procedure gives three real frequencies at a local energy minimum and two real frequencies and one imaginary frequency at a transition state.

3.3.1 Surface segregation

The chemical composition at the surface of an alloy may differ from the composition in the bulk due to surface segregation [19-23]. Previous reports showed that this surface segregation could affect adsorption significantly [24]. Therefore, five $Pd_{75}Cu_{25}$ configurations were chosen with fixed stoichiometric composition $Pd_{75}Cu_{25}$ in the two lower layers and varied composition in the surface and subsurface layer. Specifically, I performed calculations for $Pd_{100}/Pd_{50}Cu_{50}$, $Pd_{87.5}Cu_{12.5}/Pd_{62.5}Cu_{37.5}$, $Pd_{75}Cu_{25}/Pd_{75}Cu_{25}$, $Pd_{62.5}Cu_{37.5}/Pd_{87.5}Cu_{12.5}$ and $Pd_{50}Cu_{50}/Pd_{100}$ in the surface/subsurface layer. For each configuration, Pd and Cu atoms are randomly distributed on the top two layers. My results show that it is strongly energetically preferable for Cu atoms in the surface layer to exchange positions with Pd atoms from the second layer. Within the set of configurations I considered, the total energy is minimized when the surface layer is made entirely from Pd atoms and the subsurface layer has composition $Pd_{50}Cu_{50}$, as shown in Fig. 3.2. All calculations below used this structure for the top two layers, with the third and fourth layers in the surface slab having the bulk composition, $Pd_{75}Cu_{25}$.

It is interesting to consider the implications of my observations regarding surface segregation for the behavior of these membranes in a sulfur-contaminated environment. The presence of strongly adsorbing species on alloy surfaces will typically result in segregation of the alloy component that interacts most strongly with the adsorbing species to the surface. In the present example, this reasoning suggests that adsorbed S would further enhance the tendency of Pd atoms to segregate to the surface of the alloy. Although it is tempting to think of the performance of alloy membranes in sulfur-containing environments in terms of the properties of pristine metal surfaces, this

may not be the most useful approach. Recent experimental results have shown that prolonged exposure to H_2S causes the formation of thick sulfide scales on both pure Pd and some Pd–Cu alloys [25], although the growth rate of these scales was much less for some alloys than for pure Pd [6]. These experiments suggest that understanding the growth and stability of these sulfide scales may be critical to understanding the performance of Pd-based alloy membranes in sulfur-containing environment.

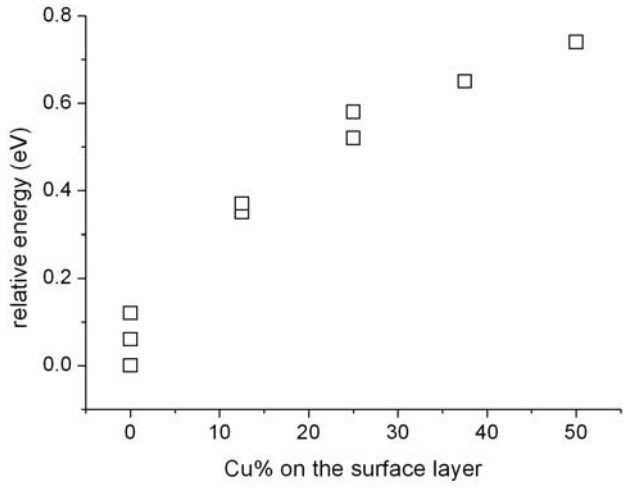

Figure 3.2: The relative energy of $Pd_{75}Cu_{25}$ with different configurations. The reference state is chosen to be the configuration with the minimum energy in my calculations.

3.3.2 Binding energy of an H atom on the surface

The desorption energy of H_2 can be treated as a combination of binding energies of individual adsorbed H atoms. Zero point energy corrected binding energies for atomic H on the surface were calculated using [12]:

$$E_b = E_{H/slab} - \frac{1}{2}E_{H_2} - E_{slab} + E_{H/slab}^{ZPE} - \frac{1}{2}E_{H_2}{}^{ZPE} \qquad (3.9)$$

where the terms on the right in this expression are the total energies of the slab with one adsorbed H atom, a H_2 molecule in the gas phase, the slab with no H, and the zero point energy of the adsorbed H and gas phase H_2 molecule, respectively. On the (111) surface of fcc metals, atomic H can bind in two types of threefold sites, namely the fcc and hcp sites, as illustrated in Fig. 3.3. Most reports showed that the adsorption of hydrogen on the fcc-hollow sites of Pd or Pd-based alloys is slightly more stable than on the hcp hollow sites [26, 27]. However, the difference of binding energies is only 0.06 eV for pure Pd [26]. Thus I considered the adsorption on both sites in my calculations.

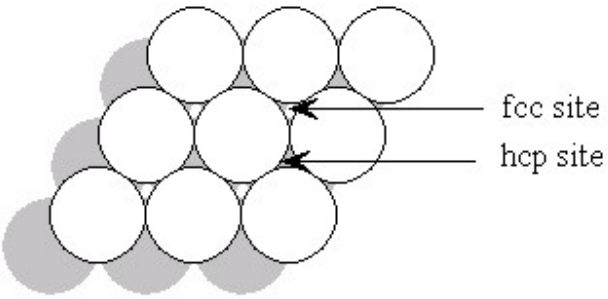

Figure 3.3: Schematic illustration of the fcc and hcp site on the Pd (111) surface. White circles: Pd atoms on surface layer, gray circles: Pd atoms on subsurface layer.

A significant difference between pure Pd and the $Pd_{75}Cu_{25}$ alloy is that the latter surface has a spatially heterogeneous set of binding sites. The binding sites on the alloy surface are geometrically similar but have varying local atomic compositions. To examine this, I used three distinct supercells that had the same layer-by-layer composition but different randomly assigned Pd and Cu positions within the layers. I

examined 48 distinct fcc sites and 48 distinct hcp sites. The distribution of the binding energies is shown in Fig. 3.4. The binding energies in fcc sites varied from −0.53 to −0.44 eV, while the energies in hcp sites varied from −0.48 to −0.40 eV.

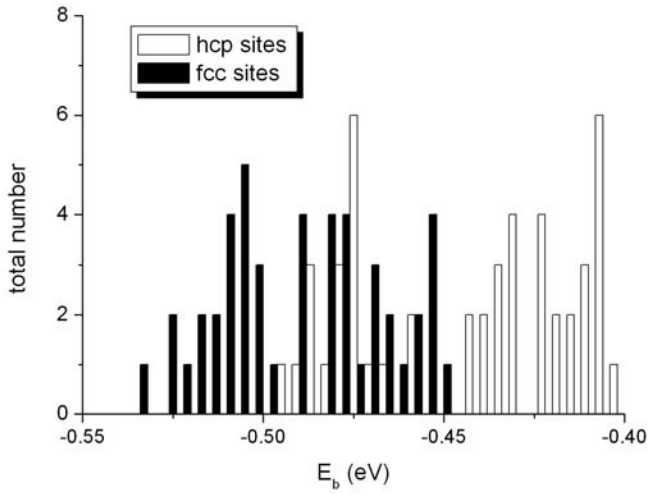

Figure 3.4: The distribution of binding energies for both fcc and hcp sites on $Pd_{75}Cu_{25}$ (111) surface.

One way to model the influence of the heterogeneity of a surface is to relate the binding energies with the identities of the metal atoms surrounding the binding sites [13]. I used a cluster expansion (CE) method to approach this task [28-30]. The basic concept of a CE is that for a given underlying lattice, any configuration can be defined using a formally infinite series of figures such as pairs, triangles, etc. The energy of any configuration on this lattice can then be written as a linear combination of the characteristic energies of each individual figure [30]. If a truncation of the infinite series is chosen, the characteristic energies for the figures in the truncated expansion can be found by fitting the available data, in my case from DFT calculations, with a

least-squares method. A detailed discussion on applying CE method to model the solubility and diffusion of interstitial H binding in the bulk of Pd-based alloys is given in Chapter V.

Since the surface layer of the alloy is made of pure Pd in my calculations, I only considered the interaction between hydrogen and metal atoms on the second layer. My truncated CE model included atoms up to the next nearest neighbor metal atoms in the second layer. Both two-body interactions between hydrogen and one metal atom, σ_1, and three body interactions between hydrogen and two metal atoms, σ_2, were included. For a hydrogen atom adsorbed at an fcc site the binding energy was expressed as

$$E_b = E_0 + \Pi_1^{NN}\sigma_1^{NN} + \Pi_1^{NNN}\sigma_1^{NNN} + \Pi_2^{NN-NN}\sigma_2^{NN-NN} + \Pi_2^{NNN-NNN}\sigma_2^{NNN-NNN} + \Pi_2^{NN-NNN}\sigma_2^{NN-NNN} + \Pi_2^{NN-NNN'}\sigma_2^{NN-NNN'} \quad (3.10)$$

Here, Π defines the number of interactions of the specified type that occur for the adsorbed atom, while σ defines the strength of these interactions [28, 30, 31]. The superscripts describe the type of interaction in terms of the locations of the metal atoms relative to the adsorbed H atom, with the nearest neighbor shell (NN) and the next nearest neighbor shell (NNN) considered separately. For instance, σ_1^{NN} describes the two-body interaction between H and one of the metal atoms closest to H in the second layer. Similarly, σ_2^{NN-NN} defines a three-body interaction between H and two of the metal atoms closest to H in the second layer. σ_2^{NN-NNN} and $\sigma_2^{NN-NNN'}$ are three-body interactions between H, one NN atom in the second layer, and one NNN atom in the second layer. These two interactions differ in the distance between the two metal atoms. For σ_2^{NN-NNN} this distance is $0.707a_0$, while in $\sigma_2^{NN-NNN'}$ it is $1.225a_0$, where a_0 is the lattice

constant. For a hydrogen atom adsorbed on an hcp site, the binding energies were expressed as:

$$E_b = E_0 + \Pi_1^b \sigma_1^b + \Pi_1^{NN} \sigma_1^{NN} + \Pi_1^{NNN} \sigma_1^{NNN} + \Pi_2^{NN-NN} \sigma_2^{NN-NN} + \Pi_2^{NNN-NNN} \sigma_2^{NNN-NNN} + \Pi_2^{NN-NNN} \sigma_2^{NN-NNN} + \Pi_2^{NN-NNN'} \sigma_2^{NN-NNN'} + \Pi_2^{b-NN} \sigma_2^{b-NN} + \Pi_2^{b-NNN} \sigma_2^{b-NNN} \quad (3.11)$$

Similar symbols were applied in eq. (3.12). The superscript "b" in this equation represents the metal atom right below the adsorbed H on the subsurface layer. The characteristic energies of each interaction in the expansion above were found by fitting the expansions to my DFT data in a least-squares sense. Table 3.1 listed all the interaction energies (σ) described in Eq. (3.10) and Eq. (3.11) for both fcc and hcp sites after cluster expansion modeling. I summarized the results from CE modeling in Fig. 3.5, which compares the predicted binding energies from my CE with the results from my DFT calculations. The error given by cluster expansion model is always within 10% of the DFT calculated value.

Table 3.1: The interaction energies in Eq. (3.11) and (3.12) obtained from cluster expansion modeling for adsorption on fcc and hcp sites. The units are all in eV.

	E_0	σ_1	σ_2
fcc sites	-0.484	NN: -0.010 NNN: 0.004	NN-NN: -0.009; NNN_NNN:-0.002 NN-NNN:0.003; NN-NNN':0.003
hcp sites	-0.427	b: -0.017 NN: -0.009 NNN: 0.007	NN-NN: -0.008; NNN_NNN:-0.005 NN-NNN:0.005; NN_NNN': 0.000 b-NN:-0.006; b-NNN: 0.000

To assess the desorption rate of hydrogen from the $Pd_{75}Cu_{25}$ surface, I generated a 500×500 atom realization of a disordered $Pd_{75}Cu_{25}$ surface with pure Pd on the surface layer and 50% Pd on the second layer. Periodic boundary conditions were applied in the plane of the surface. I then used my CE model to characterize the desorption of hydrogen from this surface.

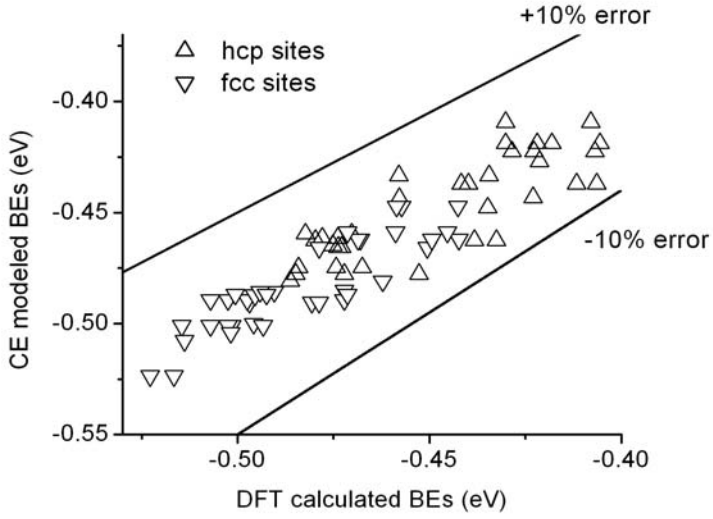

Figure 3.5: CE modeled binding energy (BE) compared with the DFT calculated binding energy for both fcc and hcp sites. The lines show 110% and 90% of the DFT calculated binding energies.

To describe the influence of adsorbate–adsorbate interactions on the desorption rate, I defined the desorption energy as

$$E_{des} = E_{b,1} + E_{b,2} + E_{H-H} \qquad (3.12)$$

Here the $E_{b,1}$ and $E_{b,2}$, are the binding energy of individual H atoms and E_{H-H} is the interaction energy between two adsorbed H atoms. To assess E_{H-H}, I performed DFT

calculations with two hydrogen atoms occupying pairs of adjacent fcc–fcc sites, fcc–hcp and hcp–hcp sites. For each kind of pairs, I randomly chose one example for each type on a (4×4) surface unit cell. The interaction energies of two H atoms on adjacent fcc sites and adjacent hcp sites were found to be 0.117 and 0.147 eV, respectively. For the fcc–hcp pair, the interaction energy was found to be 0.319 eV. All of these interactions are repulsive, with the most unstable one being the fcc–hcp pair due to the small distance between the sites. Thus, in my later calculations, I only considered desorption as occurring from fcc–fcc pairs and hcp–hcp pairs, excluding the possibility that fcc–hcp pairs exist on the surface.

3.3.3 Desorption rate

The expression needed to define the overall desorption rate constant in Eq. (3.6) is [32, 33]:

$$k = k_0 e^{-\frac{E_{des}}{k_b T}} = \frac{q_H^1 q_H^2}{q_{H_2}^{TS}} \tag{3.13}$$

Here $q_H^1 (q_H^2)$, $q_{H_2}^{TS}$ are the partition function of an adsorbed hydrogen atom and a hydrogen molecule at the transition state for desorption. I assumed that dissociation of H_2 on the surface is barrierless, so I used the partition function of gaseous H_2 instead of hydrogen molecule at the transition state in Eq. (3.13). The partition function of an adsorbed hydrogen atom and gaseous hydrogen can be calculated as [13, 33]:

$$q_H = \prod_{i=1}^{3} \frac{2k_b T}{h} \sinh\left(\frac{h\nu_{H,i}}{2k_b T}\right) e^{-\frac{E_b}{k_b T}} \tag{3.14}$$

and

$$q_{H_2} = \frac{\exp(\frac{-h\nu_{H_2}}{2k_bT})}{1-\exp(\frac{-h\nu_{H_2}}{k_bT})} \frac{k_bT}{2\varepsilon_{rot}} V(\frac{2\pi m k_b T}{h^2})^{1.5} \qquad (3.15)$$

Here ν_H and ν_{H2} are the vibrational frequencies of adsorbed H and gaseous hydrogen, ε_{rot} = 7.55 meV is the rotational constant for H_2, m and P are the mass and pressure of H_2. Similarly to the binding energies, the vibrational frequency of the adsorbed H is also influenced by the surroundings. To examine this, I chose several binding sites at random on the surface and calculated their vibrational frequencies. The results from these calculations are shown in Table 2. Neither the vibrational frequency nor the pre-factor calculated from Eq. (9) vary much among the binding sites I examined. Because the desorption rate depends on the desorption energy more strongly than on the prefactor, I used the average value of the calculated examples in my later calculations instead of calculating the pre-factor for each site.

Table 3.2: Vibrational frequencies of adsorbed hydrogen from adjacent fcc-fcc or hcp-hcp sites on the surface obtained from DFT calculations, and the pre-exponential factors for desorption from the corresponding sites at 700 K.

adsorption sites	vibrational frequencies (THz)	pre-exponential factor (10^{13} s^{-1})
fcc-fcc	29.64, 25.69, 24.00	3.3
	30.55, 25.71, 25.13	3.4
	29.58, 25.96, 22.05	3.2
hcp-hcp	35.96, 28.95, 27.05	4.1
	37.24, 30.56, 28.34	4.3
	34.96, 32.26, 27.59	4.2

`3.3.4 Prediction of the pair probability

To predict the net desorption rate of H_2 from a surface, I need to be able to predict the probability with which two adjacent binding sites on the surface are occupied. The simplest approach to this problem is the mean-field approximation, which ignores the interaction between adsorbates and distributes the adsorbates equally on each individual adsorption sites on the surface [34]. Using this approximation, the pair probabilities are expressed as:

$$\begin{aligned} P_{00} &= (1-\theta_s)^2 \\ P_{11} &= \theta_s^2 \end{aligned} \qquad (3.16)$$

Here θ_s is the fractional coverage of the adsorbate on the surface. However, I found that this approximation does not perform accurately under the operating conditions I consider below. A refinement of the interaction effects is achieved through the quasi-chemical approximation (QCA) [34, 35]. The QCA is based on the idea that pairs of adsorbates rather than individual adsorbates are distributed randomly on the surface. The pair probabilities under the QCA are [34, 35]:

$$\begin{aligned} &\frac{P_{11}P_{00}}{P_{10}^2} = 0.25\exp(-E_{H-H}/k_bT) \\ &2P_{00} + P_{10} = 2(1-\theta_s) \\ &2P_{11} + P_{10} = 2\theta_s \end{aligned} \qquad (3.17)$$

Here, P_{11}, P_{00}, and P_{10} are the probability to find two adjacent sites occupied, two adjacent sites empty, or two adjacent sites with one site empty and one occupied site, respectively. $E_{H\text{-}H}$ is the interaction energy between two adjacent hydrogen atoms, which based on the calculations described above I fixed to be 0.117 eV for fcc–fcc pairs and 0.147 eV for hcp–hcp pairs. As mentioned above, fcc–hcp pairs are excluded in my calculations. The adsorption isotherm within the QCA is [34, 35]:

$$P^{0.5} = b_0 e^{-E_b/k_bT} \frac{\theta_s}{1-\theta_s} g(\theta_s) \qquad (3.18)$$

Here $g(\theta)$ can be obtained from

$$g(\theta_s) = (\frac{2-2\theta_s}{1+\beta-2\theta_s})^z \qquad (3.19)$$

and

$$\beta = \{1-4\theta_s(1-\theta_s)[1-\exp(-E_{H-H}/k_bT)]\}^{1/2} \qquad (3.20)$$

In these equations, P is the pressure of gas phase H_2. The exponent of 0.5 in Eq. (15) arises because the adsorption of hydrogen on the surface is dissociative. z is the number of nearest neighbors on the surface, taken to be 6.

Because at dilute loading the QCA and the mean-field approximation must both lead to Sieverts' law, b_0 can be obtained by equating the chemical potentials of the adsorbed and gaseous species from [11]:

$$b_0 = e^{-E_b/k_bT} \frac{1}{\sqrt{\alpha}} (1-e^{-E_{H_2}^{ZPE}/k_bT})^{0.5} \prod_{i=1}^{3} \frac{1}{1-e^{-h\nu_{H,i}}} \qquad (3.21)$$

in which

$$\alpha = (\frac{2\pi m k_b T}{h^2})^{1.5} \frac{4\pi^2 I (k_b T)^2}{h^2} \qquad (3.22)$$

Here, ν_H is the vibrational frequency of the adsorbed hydrogen, m the mass of H_2, and I is the molecular moment of inertia of H_2.

Once b_0 is calculated in this way, the QCA is fully defined by the equations above, which can then be used to calculate the pair probabilities under any conditions of interest. Although it is more sophisticated than the mean-field approximation, the QCA is still approximate. To test the validity of QCA, I performed Grand Canonical Monte Carlo

(GCMC) simulations to accurately establish the adsorption isotherm for my description of adsorbed H and compared the result with QCA predictions [36, 37]. GCMC is a well-defined simulation method that explicitly includes the effects of adsorbate–adsorbate correlations that are approximated in the mean-field or QCA methods. In a GCMC simulation, many realizations of the surface are averaged in a statistical manner to determine the average properties of the surface under the physical conditions of interest. Unfortunately, this simulation approach needs to be applied separately at every state point of interest. As a result, it would be inconvenient to use GCMC simulations within the overall iterative procedure that is needed to compute the net flux through a membrane. Fig. 3.6 shows a contour plot of the deviation between the QCA and the results from GCMC simulations characterized by $(P_{11}^{QCA} - P_{11}^{GCMC}) / P_{11}^{GCMC}$. The difference between QCA and GCMC increases at high pressure and low temperatures, as might be expected. This phenomenon can be explained by the formation of large adsorbed clusters, which causes inaccuracy in the QCA. I will restrict my attention below to temperatures between 400 and 1000 K and pressures below 10 atm. In this range, the difference between QCA and GCMC is always less than 10%, so the QCA is an acceptable approximation during my calculations.

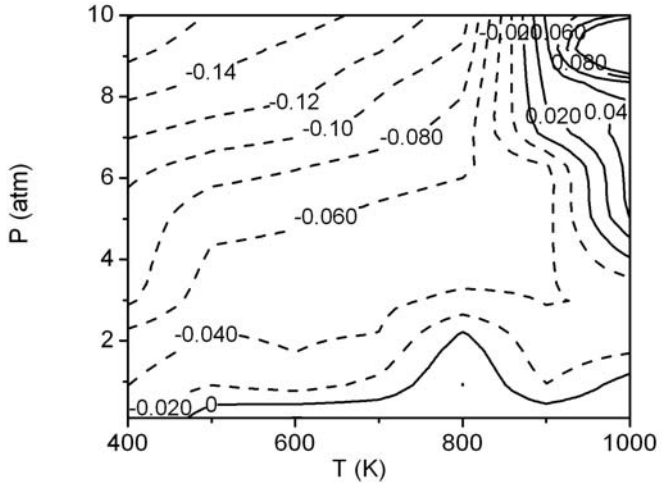

Figure 3.6: A contour plot of the deviation between QCA and GCMC predictions for the hydrogen surface coverage. See text for details.

3.3.5 Transition between surface and bulk sites

In the interior of fcc metals, H can bind at two kinds of interstitial sites, the octahedral (O) site and tetrahedral (T) site. Typically, H binds more strongly at O sites than at T sites[12, 13]. On this basis, I examined the processes that must occur for an H atom to move between a binding site on the surface of my material and O sites in the bulk. A schematic illustration of steps that define this process is shown in Fig. 3. An adsorbed H atom in an fcc hollow site can hop into the O site directly below its initial position. The atom can then hop into a tetrahedral site below the O site (denoted sub-T' in Fig. 3.7), and then into an adjacent O site (denoted sub-O' in Fig. 3.7). From this site, the atom can hop into a T site and then an O site that is characteristic of the bulk phase. If this process begins at an hcp hollow sites on the surface, the atom can first hop into the T site below its initial position, then hop to an adjacent O site below a surface fcc site. The hops that

can move the atom towards the bulk are then the same as for the process that began in a surface fcc site. The DFT-calculated difference in binding energies between sub-surface sites and bulk phase sites were small. The binding energy at the O site is only 0.066 eV larger than at sub-O site, which indicates that only a small number of layers are involved in the transition process.

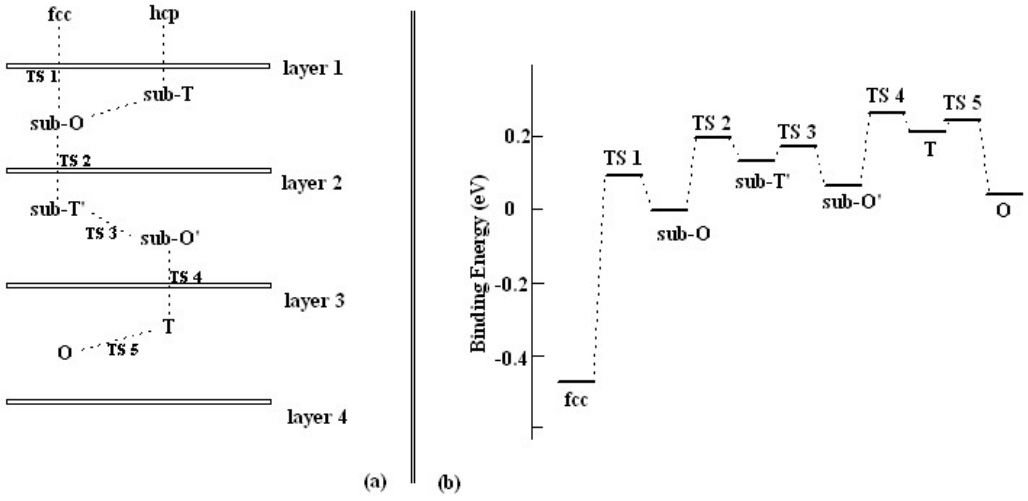

Figure 3.7: (a). A schematic illustration of the transition between surface and subsurface layers. The dotted lines show how the binding sites are connected. (b). The binding energies of hydrogen hopping from a fcc site on the surface to a octahedral site in the bulk.

Although the process described above involves multiple discrete steps, I aim to describe the overall process in terms of a single rate constant, as shown in Eqs. (3.8) and (3.9). As discussed later, the transition step will not be a rate dominant process. Therefore, instead of performing a large number of DFT calculations and setting up a detailed

database that can be used to obtain the accurate activation energy barrier, I only calculated the hopping from one fcc site and an adjacent hcp site on the surface towards a possible O site in the bulk, and estimated a net activation energy barrier for this process. A simple estimation of the activation energy of this process is to take the largest difference between the binding energies at an fcc site and the transition states along the diffusion path. This estimation gives us 0.747 eV (see Fig. 3b). A more accurate way to treat this situation is to consider hopping in the direction normal to the surface in terms of 1D diffusion model to calculate the rate using [38]:

$$\frac{1}{\Gamma} = \sum \frac{1}{\rho_\alpha \gamma_\alpha} \tag{3.23}$$

Here Γ is the net hopping rate, ρ_α is the probability of binding at site indexed α, γ_α is the hopping rate from site α to a site next to α, which can be obtained from the harmonic transition state theory [13]. Using this approach, the net activation energy is 0.730 eV for temperatures in the range 400–1200 K and the prefactor in Eq. (4) is 1.76×10^{12} s^{-1}. For the transition from bulk to surface, the same approach the activation energy barrier and prefactor were found to be 0.192 eV and 0.77×10^{12} s^{-1}, respectively.

3.3.6 Diffusion coefficient

The method used to derive bulk diffusion properties of H in Pd75Cu25 has been introduced by Kamakoti and Sholl before [13]. The calculated diffusivity can be described using the Arrhenius expression:

$$D = D_0 e^{-\frac{E_{diff}}{k_b T}} \tag{3.24}$$

where $D_0 = 2.62\times10^{-7}$ m^2/s and $E_{diff} = 0.26$ eV for the temperature higher than 700 K and $D_0 = 5.79\times10^{-7}$ m^2/s and $E_{diff} = 0.31$ eV at lower temperatures.

3. 4 Evaluation of Surface Resistance for $Pd_{75}Cu_{25}$

I first considered the performance of membranes when all the processes in my model are included, namely adsorption, diffusion, desorption, and the transitions between the membrane surfaces and the interior of the membrane. Figure 3.8 shows the calculated hydrogen flux for 1 μm membranes with 1 atm feed pressure and a vacuum condition at the permeate side. Fig. 3.8 also shows the flux predicted by only including the diffusion and desorption resistances in the membrane model. It can be seen from comparing these two sets of results that the adsorption and transition resistances are not dominant processes at any of the temperatures I have examined.

To evaluate the influence of the estimated activation energy barrier in the surface to subsurface transitions, I repeated my calculation while varying the activation energy barriers associated with these processes. When the activation energy barriers in Eq. 3.7 (Eq.3.8) are increased from the estimated 0.730 (0.192) to 1.00 (0.462) and 1.10 (0.562) eV, the calculated flux decreases about 10%. At higher temperatures, almost no decrease in the flux occurs even when the activation energy barriers are increased to 1.10 (0.562) eV. Since my estimated activation energy barrier in Eq. 3.7is far below 1.00 eV, the surface–subsurface transitions will not be a rate dominant process in my calculations. Ward and Dao previously concluded that for pure Pd, neither adsorption or surface-subsurface transitions are the rate dominant processes [10]. My results are

consistent with their conclusion. Therefore, in my later calculations, I will only consider the diffusion and desorption resistance.

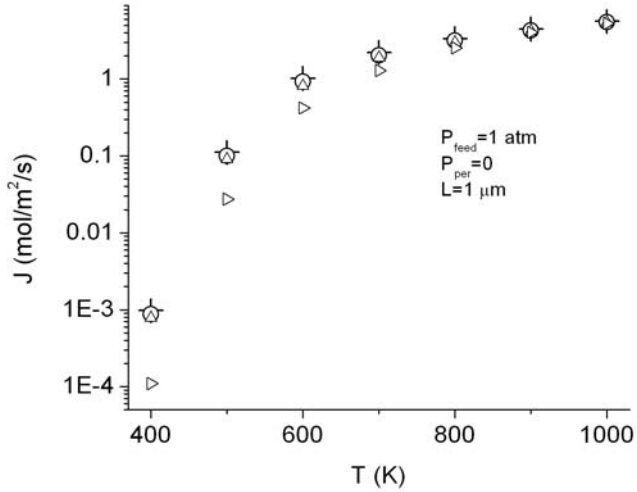

Figure 3.8: Hydrogen flux as a function of temperature for $Pd_{75}Cu_{25}$ membranes, including transport resistance from desorption, diffusion, adsorption and transitions between the surface and the bulk. Circles, triangles and squares correspond to different activation energies (E_a) for the surface to subsurface hopping process. For circles, E_a= 0.730 eV, triangles, E_a= 1 eV and squares, E_a= 1.1 eV. Crosses indicate calculations that included only effects from desorption and diffusion.

Fig. 3.9 shows the calculated flux through $Pd_{75}Cu_{25}$ membranes of several different thicknesses as a function of temperature for a feed pressure of 1 atm and a vacuum condition on the permeate side. The solid curves in Fig. 5 show the predicted flux if only intracrystalline diffusion is included in the description of permeation through the membrane. At sufficiently low temperatures, the net flux can be significantly lower

than the diffusion-limited flux. This is the same qualitative trend that was observed by Ward and Dao in their model for pure Pd [10].

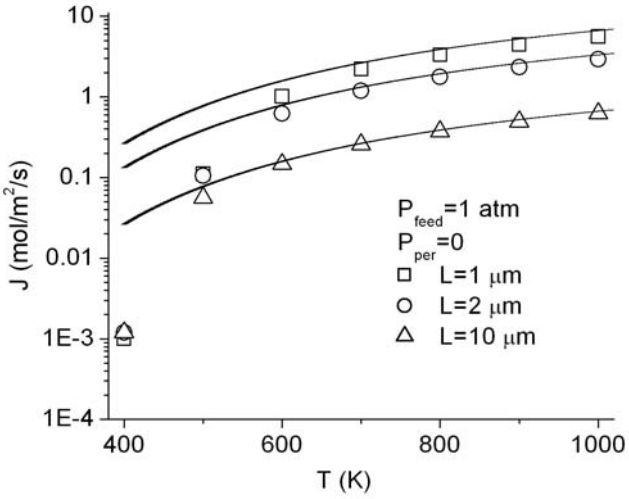

Figure 3.9: Hydrogen flux as a function of temperature for $Cu_{25}Pd_{75}$ membranes of different thicknesses, *L*. The solid line shows the diffusion limited flux for each thickness. The feed and permeate pressure are fixed to be 1 atm and 0.

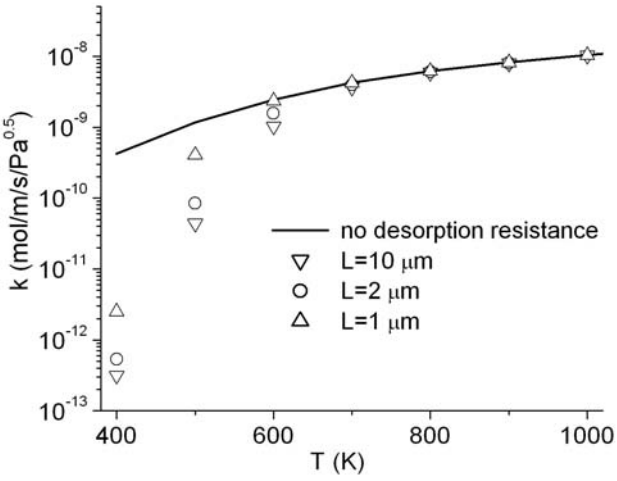

Figure 3.10: Hydrogen permeability, *k*, calculated from Fig. 4 as a function of temperature

The results from Fig. 3.9 are presented in terms of membrane permeability in Fig. 3.10. When this is done, the diffusion-limited result is independent of the membrane thickness. It is apparent from Fig. 3.10 that at 600 K, membranes that are 1 or 2 μm thick show a noticeable deviation from the diffusion limited regime but a membrane 10 μm thick (or thicker) does not. At lower temperatures, a 10 μm thick membrane also has a considerably lower net flux than predicted by the diffusion-limited result. At T = 400 K the deviations from the diffusion-limited result are very large; including the desorption resistance at this temperature reduces the hydrogen permeability by two to three orders of magnitude for membranes that are 1–10 μm thick. To characterize the importance of desorption resistances in membrane performance, it is useful to define the diffusion resistance ratio as $R_{\mathrm{diff}}/R_{\mathrm{tot}}$, where R_{diff} (R_{tot}) is the resistance due to intracrystalline diffusion (the total resistance of the membrane) [39, 40]. If J_{diff} is the membrane flux in the diffusion-limited regime and J is the actual flux through a membrane, then

$$\frac{R_{diff}}{R_{tot}} = \frac{J}{J_{diff}} \tag{3.25}$$

I am considering the situation where the only resistance other than intra crystalline diffusion is due to desorption from the membrane surface. Denoting this resistance by R_{des}, I see that

$$\frac{R_{desf}}{R_{tot}} = 1 - \frac{J}{J_{diff}} \tag{3.26}$$

I will refer to this quantity as the desorption resistance ratio. The desorption resistance ratios for the situations considered in Fig. 3.9 are shown in Fig. 3.11. It can be seen that for a membrane with thickness 1 or 2 μm, the temperature must be larger than 700 K

before the desorption resistance is less than 10% of the total resistance for the conditions considered in Fig. 3.9.

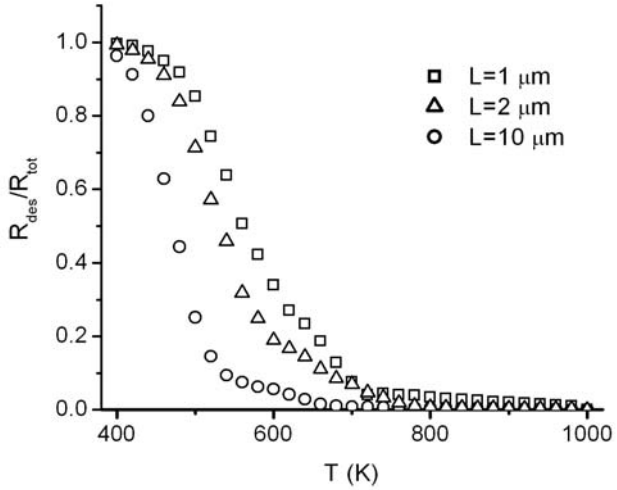

Figure 3.11: Desorption resistance ratio for $Cu_{25}Pd_{75}$ membranes of different thicknesses, *L* as a function of temperature. The feed pressure and permeate pressure is 1 atm and 0, respectively.

The results discussed above were all based on the same operating conditions, namely a feed pressure of 1 atm and a vacuum condition in the permeate side. Figure 3.12 shows the desorption resistance ratio as the permeate pressure is varied while holding the feed pressure constant at 1 atm. All of the results in Fig. 3.12 are for 1 μm membrane. The most interesting effects of the permeate pressure occur under the conditions where neither the intracrystalline diffusion or the desorption is completely dominant, that is for temperatures of 500–700 K. In this range, increasing the permeate pressure leads to a decrease in the desorption resistance ratio. That is, for lower permeate pressures, the desorption resistances tend to be more important. This sensitivity to the permeate

pressure can be understood by noting that at low temperatures the surface coverage of H can be quite high if the surfaces are close to being in equilibrium with even moderate pressures of gaseous H_2. As a result, the boundary conditions that control the strength of the desorption resistance can change significantly as the permeate pressure changes from a vacuum condition to a finite pressure.

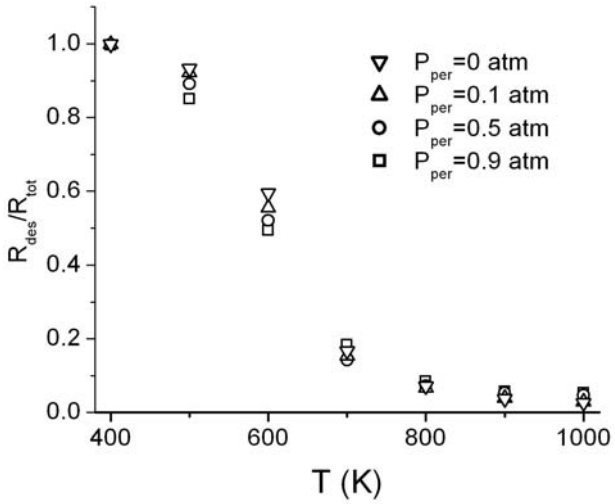

Figure 3.12: Desorption resistance ratio with different permeate pressures as a function of temperature. The thickness of the membrane and the permeate pressure is fixed to be 1 μm and 1 atm, respectively.

In Fig. 3.13, I explore the influence of feed pressure and the transmembrane pressure drop. Instead of plotting the desorption resistance ratio for all temperatures, this figure focuses on the conditions where this ratio is either 0.9 or 0.1. In the former case, the membrane's performance is dominated by desorption, while in the latter neglecting

the desorption resistance would be a reasonable approximation. Fig. 3.13 shows results for three sets of pressure drops as characterized by

$$\Delta P^{0.5} = \sqrt{P_{feed}} - \sqrt{P_{permeate}} \tag{3.27}$$

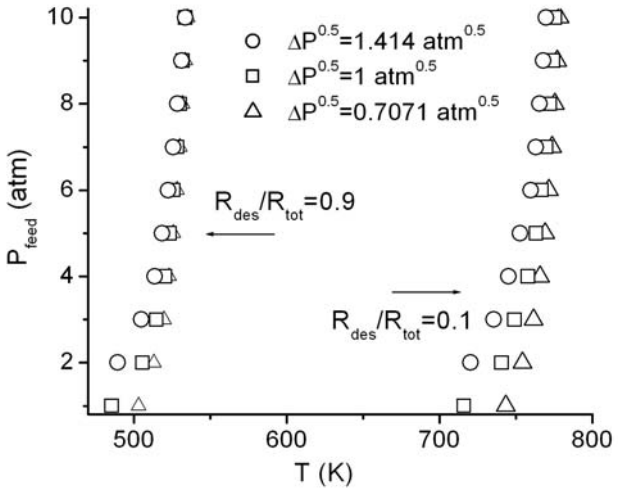

Figure 3.13: Desorption resistance ratio as a function of temperature for different feed and permeate pressures. The thickness of the membrane is 1 μm.

At the larger feed pressures shown in Fig. 3.13, the desorption resistance ratios are close to being independent of the pressure drop. At lower feed pressures, however, reducing the pressure drop increases the importance of the desorption resistance. For a feed pressure of 2 atm, for example, changing $\Delta P^{0.5}$ from 1.414 to 0.7071 atm$^{0.5}$ increases the temperature at which the desorption resistance ratio becomes 0.1 by ~20 K. As might be expected, the thickness of a membrane has a much more dramatic effect on the importance of the desorption resistance than the feed and permeate pressures. Fig. 3.14 shows that desorption resistance ratios for membranes that are 100, 10, and 1μm thick as a function of the feed pressure with a fixed trans-membrane pressure drop of 1 atm.

Similar to Fig. 3.13, only the conditions where the desorption resistance ratio is 0.9 or 0.1 are shown in Fig. 3.14. A useful way to view Fig. 3.14 is that any temperature to the right of the set of open symbols corresponding to a particular membrane thickness is a situation where it is accurate to assume that permeation through the membrane is dominated by bulk diffusion. For membranes that are 100 or 10 μm thick, this regime is reached for essentially any temperature above 500 or 600 K, respectively. If membrane thicknesses are reduced to 1 μm, however, temperatures above ~750 K are necessary before desorption resistances can be neglected. Another way to look at this is that at temperatures around 500 K, desorption resistances can be neglected for membranes that are 100 μm thick, but these resistances would dominate the performance of membranes that are 1 μm thick.

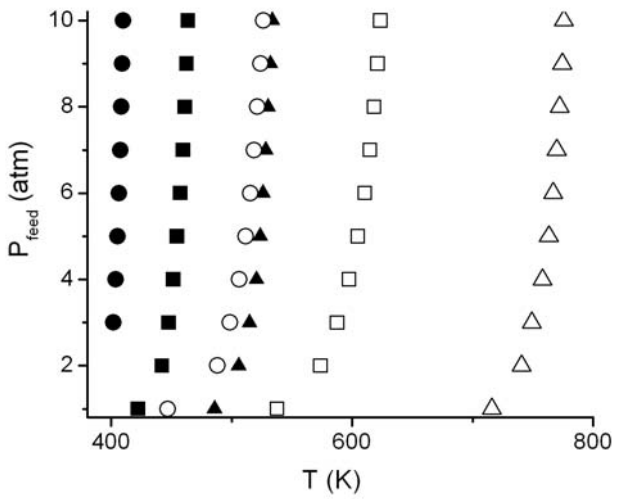

Figure 3.14 The desorption resistance ratio for membranes of different thicknesses. The solid and open symbols correspond to R_{des}/R_{tot}= 0.9 and 0.1, respectively. The circle, square and triangles correspond to 100, 10 and 1 μm membranes, respectively.

3. 5. Surface Resistance for other PdCu alloys

All the calculations above were for a $Pd_{75}Cu_{25}$ alloy, since the calculation of the desorption rate is based on the information obtained in $Pd_{75}Cu_{25}$. To explore the validity of the model in different PdCu alloys, I used the same cluster expansion parameters extracted from $Pd_{75}Cu_{25}$ to model the desorption energy on different PdCu surfaces. The binding energy on pure Pd(111) surface in an fcc site is predicted by this approach to be 0.530 eV, in a good agreement with the experimental result 0.513 eV used in Ward and Dao's calculation and the result I obtained from a DFT calculation (0.527 eV). The diffusion coefficients as a function of the alloy composition were calculated using the DFT-based results of Kamakoti and Sholl [13]. With these estimation, I calculated the desorption resistance ratio as a function of temperature for different PdCu alloys, as shown in Fig. 3.15. This figure also shows the result calculated with experimentally derived desorption parameters for pure Pd using Ward and Dao's method [10]. This comparison indicates that my estimation slightly underestimates the desorption resistance of pure Pd. Nonetheless, I feel that my results do give useful information about the trend in the resistance ratios as a function of alloy composition. It can be seen from Fig. 3.15 that the importance of the desorption resistance increases with the Pd amount in the alloy. This primarily is a result of the increase in the diffusion resistance as the Pd content of the alloy is decreased.

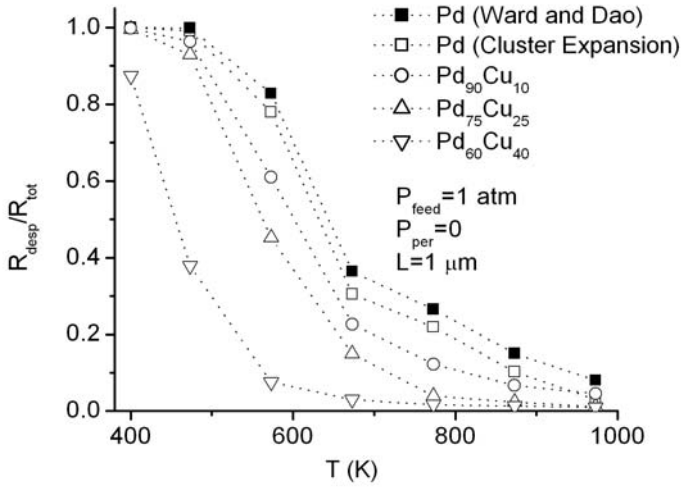

Figure 3.15: The desorption resistance ratio as a function of temperature for membranes of different composition. The solid symbols are calculated results using the same model in ref. 10. The dashed lines are to guide the eye.

3.6. Conclusion

In this chapter, I have applied plane wave density functional theory calculations to evaluate the surface resistance of hydrogen permeating through $Pd_{75}Cu_{25}$ membranes. My calculations focus exclusively on predicting the permeance of pure hydrogen through these membranes; no information about the performance of the membranes in the presence of chemical contaminants is generated by my calculations. My results indicate that diffusion is the rate-dominating process in these membranes at moderately high temperatures. Desorption is found to be the rate-limiting process at low temperatures. Neither adsorption nor transitions between surface and subsurface sites dominate the permeation process for temperatures in the range 400–1000 K. The influence of the thickness and composition of the membrane, the permeate pressure and the pressure

difference were also examined. The results show that the influence of the thickness and composition of membranes is much more important than the feed pressure or transmembrane pressure drop. For 1 μm membranes, the desorption resistance must be considered at temperatures lower than 700 K. At temperatures less than 500 K, the desorption resistance dominates the permeation process, which indicates that further decrease in membrane thickness would not improve the hydrogen flux under these operating conditions.

My calculations have provided information about surface resistances to hydrogen permeation through metal membranes that would be challenging to unambiguously determine from experiments. As with studies of surface resistances for other kinds of membranes, one useful outcome of models of this type is the ability to identify broad ranges of operating conditions for which surface resistances can be neglected. An important feature of my methods is that they could be extended to a range of metal alloys without requiring extensive experimental characterization of each material to be considered. As a result, my methods should be useful within the framework of selecting materials and optimizing membrane properties to enhance the performance of metal membranes for hydrogen separations.

3.7 Reference

[1]T. M. Nenoff, R. J. Spontak, C. M. Aberg MRS Bull. 31 (2006)

[2]S. N. Paglieri, J. D. Way Purif. Methods 31 1 (2002)

[3]D. S. Sholl, Y. H. Ma MRS Bull. 31 770 (2006)

[4]K. Hashi, K. Ishikawa, T. Matsuda, K. Aoki J. Alloys. Comp. 368 215 (2004)

[5]B. A. McCool, Y. S. Lin J. Membr. Sci 36 3221 (2001)

[6]F. Guazzone, E. E. Engwall, Y. H. Ma Cat. Today 118 24 (2006)

[7]Y. Zhang, J. Gwak, Y. Murakoshi, T. Ikehara, R. Maeda, C. Nishimura J. Membr. Sci 227 203 (2006)

[8]N. M. Peachey, R. C. Snow, R. C. Dye J. Membr. Sci 123 (1996)

[9]M. D. Dolan, N. C. Dave, A. Y. Ilyushechkin, L. D. Morpeth, K. G. McLennan J. Membr. Sci 285 30 (2006)

[10]T. L. Ward, T. Dao J. Membr. Sci 153 211 (1999)

[11]P. Kamakoti, B. D. Morreale, M. V. Ciocco, B. H. Howard, R. P. Killmeyer, A. V. Cugini, D. S. Sholl Science 307 569 (2005)

[12]P. Kamakoti, D. S. Sholl J. Membr. Sci 225 145 (2003)

[13]P. Kamakoti, D. S. Sholl Phys. Rev. B 71 014301 (2005)

[14]C. G. Sonwane, J. Wilcox, Y. H. Ma J. Phys. Chem. B 110 24549 (2006)

[15]C. G. Sonwane, J. Wilcox, Y. H. Ma J. Chem. Phys. 125 184714 (2006)

[16]S. Q. Hao, D. S. Sholl J. Chem. Phys. 130 244705 (2009)

[17]G. Kresse, J. Hafner Phys. Rev. B 48 13115 (1993)

[18]G. Henkelman, B. P. Uberuaga, H. Jonsson J. Chem. Phys. 113 9901 (2000)

[19]A. V. Ruban, H. L. Skriver, J. K. Norskov Phys. Rev. B 59 15990 (1999)

[20]J. W. Han, J. R. Kitchin, D. S. Sholl J. Chem. Phys. 130 124710 (2009)

[21]K. W. Wang, S. R. Chung, T. P. Perng J. Alloys. Comp. 422 223 (2006)

[22]J. A. Leiro, M. H. Heinonen, I. G. Batirev App. Surf. Sci 90 515 (1995)

[23]R. A. Bennett, S. Poulston, N. J. Price, J. P. Reilly, C. J. Barnes, M. Bowker Surf. Sci. 433 816 (1999)

[24]V. Pallassana, M. Neurock, L. B. Hansen, J. K. Nørskov J. Chem. Phys. 112 5435 (2000)

[25]B. D. Morreale, B. H. Howard, O. Lyoha, R. M. Enick, C. Ling, D. S. Sholl Ind. Eng. Chem. Res. 46 6313 (2007)

[26]W. Dong, V. Ledentu, P. Sautet, A. Eichler, J. Hafner Surf. Sci. 411 123 (1998)

[27]J. F. Paul, P. Suatet Phys. Rev. B 53 8015 (1996)

[28]J. M. Sanchez, F. Ducastelle, D. Gratias Physica A 128 334 (1984)

[29]O. Wieckhorst, S. Muller, L. Hammer, K. Heinz Phys. Rev. Lett. 74 174202 (2004)

[30]L. Semidey-Flecha, D. S. Sholl J. Chem. Phys. 128 144701 (2008)

[31]S. Muller J. Phys: Condes. Matter 15 R1429 (2003)

[32]T. Vegge Phys. Rev. B 70 035412 (2004)

[33]B. Dai, D. S. Sholl, J. K. Johnson J. Phys. Chem. C 111 6910 (2007)

[34]R. H. Fowler, E. A. Guggenheim *Statistical Thermodynamics* (Cambridge University Press, Cambridge, 1939),

[35]T. L. Hill *Statistical Mechanics* (McGraw-Hill, New York, 1956),

[36]D. Frenkel, B. Smit *Understanding molecular simulation: From algorithms to applications, 2nd Edition* (Academic Press, San Diego, 2002),

[37]S. A. FitzGerald, R. Hannachi, D. Sethna, M. Rinkoski, K. K. Sieber, D. S. Sholl Phys. Rev. B 045415 (2005)

[38]O. M. Braun, C. A. Sholl Phys. Rev. B 58 14870 (1998)

[39]D. A. Newsome, D. S. Sholl J. Phys. Chem. B 109 7237 (2005)

[40]D. A. Newsome, D. S. Sholl Nano Lett. 6 2150 (2006)

Chapter IV Evaluation of the H permeability in metal sulfides

In the application of dense metal membranes as hydrogen purification materials, one fundamental challenge is the poisoning of membranes due to trace gases such as hydrogen sulfide and carbon monoxide. H_2S severely reduces the performance of Pd membranes, the most studied metal membranes for hydrogen purification.[1] In order to solve the poisoning problem, Pd-based alloys are studied experimentally, among which PdCu is found to increase the poisoning resistance to H_2S.[2, 3] In this chapter, I discuss another possible approach to solve the poisoning problem. That is, instead of using Pd based metal membranes, I examined the possibility of using metal sulfide membranes for hydrogen purification. I will discuss how to apply Density Functional Theory calculations to predict the permeation characteristics of H in nine different metal sulfides. I will discuss how to estimate the solubilities and diffusivities of hydrogen in these materials from the calculations of the adsorption and hopping of individual hydrogen atom, and further discuss the potential of using these materials as hydrogen purification membranes.

4.1 Introduction

One difficulty in the application of Pd membrane in hydrogen purification is that Pd membranes are sensitive to trace impurities in the feed gas. H_2S, for example, can dramatically reduce the performance of Pd membranes.[1, 4] Several research groups studied the effect of hydrogen sulfide poisoning on hydrogen permeability of the Pd composite membranes.[1, 3, 5, 6] Pd-coated membranes can rapidly be destroyed after exposure to a gas stream containing hydrogen sulfide, and the poisoning effects are

typically irreversible. For example, Morreale and coworkers studied the influence of H_2S on pure palladium membranes at temperatures of 623, 723, and 908 K in the presence of a 120 h exposure to 0.1%H_2S-10%He-H_2. They found that the palladium membranes exhibited a continuous decrease in hydrogen flux in the presence of the H_2S-containing gas mixture. After 120 h of operation in the presence of H_2S, the rate of flux decrease had diminished substantially, with reductions in performance of 75%, 82%, and 81% were observed at temperatures of 623, 723, and 908 K, respectively.[6]

The impact of H_2S on Pd based membranes can be discussed in terms of two mechanisms.[6] First, sulfur can deactivate the membrane surface by adsorbing on surface sites and diminishing the catalytic activity of the membrane surface. Several papers have been published to address the issue of adsorption of S on Pd(111).[7, 8, 9] They observed a substantial decrease in the electron density belonging to the metal near the Fermi level and a simultaneous drop in the electron population of its 4d band.[10] After adsorption of sulfur on the Pd surfaces the activity of Pd decreases for adsorption reactions involving donation of electrons to the adsorbate molecules (H_2, CO, etc.).[11] The adsorbed sulfur atoms also hinder the dissociation of H_2 on the Pd surfaces[12] and reduce the mobility of hydrogen atoms located on the Pd surface[13]. As I discussed in Chapter III, catalytic H_2 dissociation is a fundamental step in the overall transport mechanism of hydrogen through dense palladium. This mechanism, which can be referred to as a "catalytic poisoning" mechanism, negatively impacts membrane performance via physisorbed or chemisorbed sulfur on the surface of the membrane. Second, H_2S gas can chemically react with the membrane to produce a corrosion product on the surface. This corrosion product can exhibit characteristics that would limit the

catalytic activity required for transport and/or reduce the overall performance by forming a layer with low permeability for hydrogen. This mechanism will be referred to as "corrosive decay".

Recently, several groups have reported the formation of Pd sulfides when they exposed Pd membranes to H_2S containing gases.[1, 6] For example, Kajiwara reported rupture of a Pd composite membrane after exposure to a hydrogen stream containing hydrogen sulfide. Pd became palladium sulfide during their experiments.[1] Experiments at NETL provide clear evidence that palladium membranes exposed to gas mixtures containing H_2S for prolonged periods under certain conditions develop thick layers of Pd_4S. Thus, when examining the effect of H_2S, corrosive decay must be considered rather than simply assuming catalytic poisoning.[6]

It is widely thought that the observations listed above for Pd_4S are likely to apply to other sulfides as well, meaning that the formation of sulfide layer on a metal membrane will lead to strong decreases in hydrogen permeability.[6] If, on the other hand, dense sulfides show appreciable permeability for hydrogen, they could potentially be used in membranes suitable for sulfur-containing environments. The motivation of my work is thus to examine a novel approach to the challenge of sulfur poisoning of metal membranes, namely the use of metal sulfides rather than metals as membrane materials. The crystal structures of numerous metal sulfides are already known. However, I know of no experimental efforts to measure H permeability through metal sulfides.

In situations where experimental examination of dense membrane materials is challenging, first principles calculations based on Density Functional Theory (DFT) can be a useful complementary tool. DFT calculations have been shown to be useful for

exploring the crystal structures and electronic properties of metal sulfides.[14, 15, 16] It can also accurately describe the diffusion of metal atoms in metal sulfides.[17] This body of previous work with DFT calculations indicates that these methods may be useful for examining the permeation of H through metal sulfides.[18]

In this chapter, I apply DFT calculations to predict the permeation characteristics of H in nine metal sulfides including Pd_4S. One reason to choose these materials is that previous reports showed that DFT can accurately predict these material's crystal structures and their cohesive and electronic properties. This idea excludes MoS_2, for example, because DFT does not accurately characterize the weak interactions between layers in this layered material.

4.2 Computational details

I used the Vienna *ab initio* simulation package (VASP) to perform DFT calculations, using the generalized gradient approximation (GGA) with the PW91 functional to describe electron exchange-correlation effects. Ion-electron interactions were described by ultrasoft pseudopotentials. A plane-wave expansion with a cutoff of 250 eV is used in all calculations.[19] Geometry relaxations were performed with a conjugate gradient method algorithm until the forces on all unconstrained atoms were less than 0.03 eV/Å. A Monkhorst-Pack mesh with 4×4×4 *k*-points was used for all calculations. Spin effects were considered in materials involving Fe and Ni.

I studied H binding in VS, CrS, FeS, NiS and NbS, all of which have a $B8_1$ (NiAs-type) crystal structure, FeS_2 and NiS_2, both with a C2 structure, ScS with a B1 (NaCl-type) structure and Pd4S with a D_{2d}^4 structure.[20, 21] A computational supercell

containing 2×2×2 primitive unit cells was used in all calculations. I note that the International Crystal Structure Database (ICSD) does not list any crystal structures that include any of these metals, sulfur, and hydrogen ternary system.[20] To find the energy minima for interstitial H in these materials, I applied a method based on using empirical pair potentials to create initial states for DFT calculations.[22] All atoms were relaxed during the DFT geometry optimization, although the unit cell size and shape was fixed at the DFT-optimized structure for the sulfide.

Transition states for diffusion of H were determined using the Nudged Elastic Band (NEB) method.[23] The vibrational frequencies of local minima and transition states were calculated in the harmonic approximation by assuming that localized vibrations of H atoms are decoupled from vibrations of the metal atoms. This procedure gives three real frequencies at a local energy minimum and two real frequencies and one imaginary frequency at a transition state.

4.3 Interstitial H properties in metal sulfides

Before performing any calculation involving interstitial H in the metal sulfide, the crystal structures of all metal sulfides were optimized first. Table 1 lists the DFT optimized lattice constants of the metal sulfides I studied, as well as experimental data for these quantities.[14] I also list the difference of unit cell volume between the DFT optimized structure and experimental measurements. For all the sulfides I considered, the DFT optimized structures were in good agreement with experimental data, which confirmed that DFT is a good tool to study these systems, consistent with previous reports.

As light elements typically occupy the interstitial sites rather than substantitial sites in metals, my calculations examined interstitial H in metal sulfides by placing one H atom in a supercell containing 2×2×2 primitive unit cells of the solid. The lattice constant of each material was fixed at the DFT-optimized value listed in Table 4. 1, except where otherwise noted. The initial configuration of metal-sulfide-hydrogen system was obtained using empirical pair potential to find the local minima. After DFT optimization[24], all possible interstitial sites in the metal sulfides were distinguished and discussed below.

Table 4.1: Crystallographic data for metal sulfides, compared with data from Raybaud et al. [14] and Gronvold et al.[21]

	Bravais class	Space group	DFT optimized lattice constants (Å)		Measured lattice constants (Å)		ΔV
VS	Hexagonal	$P6_3/mmc$	a=3.327	c=5.717	a=3.340	c=5.785	-2.0%
CrS	Hexagonal	$P6_3/mmc$	a=3.360	c=5.374	a=3.329	c=5.324	2.9%
FeS	Hexagonal	$P6_3/mmc$	a=3.432	c=5.581	a=3.445	c=5.763	-3.9%
NiS	Hexagonal	$P6_3/mmc$	a=3.436	c=5.318	a=3.439	c=5.323	-0.3%
NbS	Hexagonal	$P6_3/mmc$	a=3.347	c=6.512	a=3.320	c=6.460	2.5%
FeS2	Cubic	$Pa\bar{3}$	a=5.527		a=5.428		5.6%
NiS2	Cubic	$Pa\bar{3}$	a=5.529		a=5.620		-4.8%
ScS	Cubic	$Fm\bar{3}m$	a=5.245		a=5.190		3.2%
Pd4S	tetragonal	$P\bar{4}2_1c$	a=5.217	C=5.702	a=5.115	c=5.590	6.1%

4.3.1 Possible interstitial sites for individual hydrogen atoms

For VS, CrS, FeS, NiS and NbS with $B8_1$ crystal structure, the metal atoms (M) form a hexagonal lattice and sulfur atoms occupy half of the M_6 prisms, as shown in Fig. 4.1. DFT optimization revealed that there are three possible interstitial sites for H in these sulfides. Site A is a site located in the empty M_6 prism (atoms labeled 1-6 in Fig. 4. 1) and close to a M_3 plane (atoms labeled 1-3 in Fig. 1). Site B is located in the middle of two metal atoms and two sulfur atoms (atoms 1, 2, 7, and 8 in Fig. 4. 1). Site C is located in the same empty prism with site A, but close to M_4 plane defined, for example, by atoms 1, 2, 4, and 5 in Fig. 4.1.

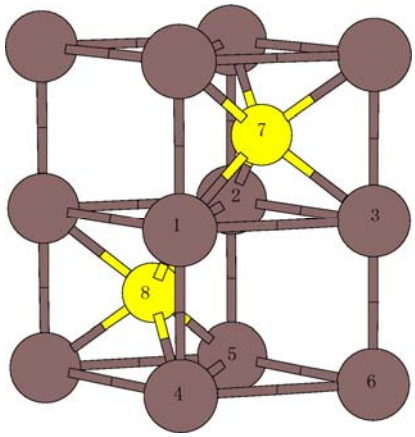

Figure 4.1: Illustration of the unit cell of metal sulfides with $B8_1$ structure, with metal (sulfur) atoms colored brown (yellow).

Both FeS_2 and NiS_2 have a C2 crystal structure. DFT optimization gave two possible binding sites for interstitial H. Site A is located in a MS_3 cage (atoms 1, 2, 3, and 5 in Fig. 2), while site B is located in an S_4 cage (atoms 1, 2, 3, and 4 in Fig. 4. 2) .

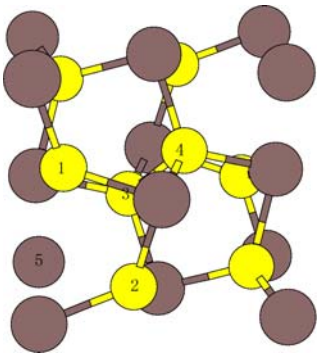

Figure 4.2: Illustration of the unit cell of metal sulfides with C2 structure, with the same color scheme as Fig. 4.1.

ScS has the B1 (NaCl type) structure, and I found two possible interstitial sites in the lattice. The most stable site is located in a Sc_4S_4 cube while the second interstitial site is located in the center of Sc_2S_2 planes that forms the sides of the Sc_4S_4 cubes.

For Pd_4S, five distinct interstitial sites are located in its D_{2d}^4 structure. The most stable site, site A is identified as a tetrahedral site surrounded by fmy Pd atoms. The other fmy sites, sites B-D, are all surrounded by three Pd atoms and one S atom. In Table 4.2, I listed the information for all possible interstitial sites in these metal sulfides, including the surrounding atoms, nearest neighbors and binding energies as discussed below.

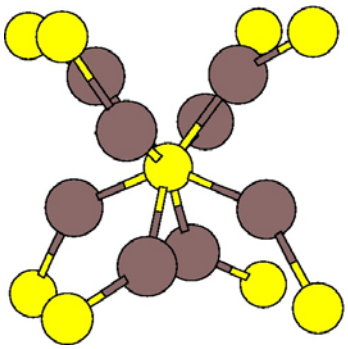

Figure 4.3: Illustration of the unit cell of Pd_4S, with the same color scheme as Fig. 4.1.

4.3.2 Properties of interstitial hydrogen in metal sulfides

After the geometry optimization of each sulfide with one interstitial hydrogen atom in a supercell containing 2×2×2 primitive unit cells, the zero point energy corrected binding energies of interstitial hydrogen, E_b, were calculated as [25]

$$E_b = E_{MS-H} - E_{MS} - 0.5E_{H_2} + E_{MS-H}^{ZPE} - 0.5E_{H_2}^{ZPE} \quad (4.1)$$

Here $E_{MS\text{-}H}$, E_{MS}, E_{H2} is the total energy of the metal sulfides with one interstitial hydrogen, without interstitial hydrogen, and gaseous H_2, respectively, and $E_{MS\text{-}H}^{ZPE}$, (E_{H2}^{ZPE}) is the zero point energy of interstitial hydrogen (gaseous H_2).With this definition, negative binding energies are energetically favorable relative to gaseous molecular H_2.

The binding energies in each metal sulfide are shown in Fig. 4. 4. and listed in Table 4. 2. In all five metal sulfides with $B8_1$ structure, site A is the most stable site while site C is the least stable site. The binding of hydrogen in site A of FeS and VS is very energetically favorable with binding energies lower than -0.4 eV, but all other sites in these five materials are energetically unfavorable compared with gaseous H_2. This result also indicates that a high solubility of hydrogen in FeS and VS may exist, as I will discuss later. For NbS and ScS, the binding energies at all possible sites are higher than 0.3 eV. For FeS_2 and NiS_2, the lowest binding energy is even higher than 1.5 eV. These data indicate that the interstitial H is very unstable and H solubility is very low in these sulfides. In Pd_4S, I notice that the binding energy at site A is 0.11 eV, which also indicated that a considerable solubility in Pd_4S.

Table 4.2: Information for all interstitial sites in the metal sulfides I examine.

sulfides	Interstitial site	Nearest atoms	Nearest sites	E_b (eV)
VS	A	V6	1A 3B 3C	-0.47
	B	V2S2	2A 2C	0.2
	C	V6	2A 2B	1.09
FeS	A	Fe6	1A 3B 3C	-0.71
	B	Fe2S2	2A 2C	0.26
	C	Fe6	2A 2B	0.67
CrS	A	Cr6	1A 3B 3C	0.01
	B	Cr2S2	2A 2C	0.25
	C	Cr 6	2A 2B	0.49
NiS	A	Ni6	1A 3B 3C	0.07
	B	Ni2S2	2A 2C	0.27
	C	Ni6	2A 2B	0.31
NbS	A	Nb6	1A 3B 3C	0.3
	B	Nb2S2	2A 2C	1.08
	C	Nb6	2A 2B	1.25
FeS2	A	FeS3	3A 1B	1.47
	B	S4	4A	1.91
NiS2	A	NiS3	3A 1B	1.52
	B	S4	4A	1.94
ScS	A	Sc4S4	8B	0.85
	B	Sc2S2	2A	1.62
Pd_4S	A	Pd4	4B	0.11
	B	Pd3S	A B C D	0.17
	C	Pd3S	B 2D E	0.23
	D	Pd3S	B 2C E	0.25
	E	Pd3S	2C 2D	0.29

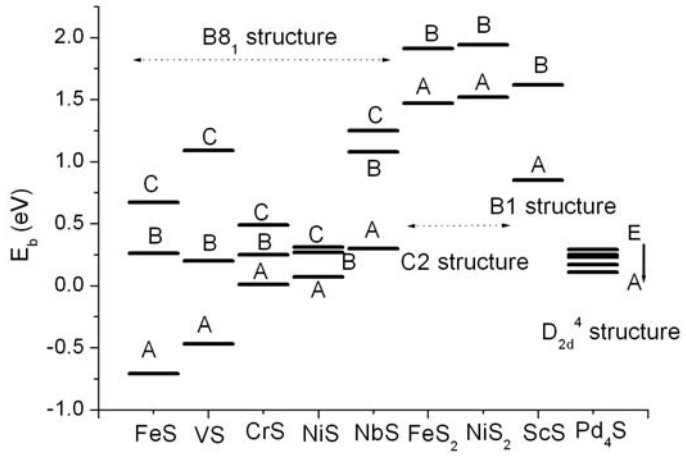

Figure 4.4: Binding energies of hydrogen in metal sulfides as calculated using DFT.

4.3.3 Lattice distortion caused by interstitial hydrogen

The presence of interstitial hydrogen can cause a significant local distortion of lattice atoms in these sulfides. For example, when one interstitial hydrogen atom occupies site A of FeS in the prism formed by Fe atoms1-6 in Fig. 4. 1, the movement of the nearest metal atoms, Fe1, Fe2 and Fe3 is 0.33 Å, while the movement of the nearest sulfur atom, S1 is 0.37 Å. In Table 4.2, the movements of the nearest metal and sulfur atoms caused by the interstitial hydrogen are listed for all possible binding sites.

In order to further check the distortion of lattice caused by the interstitial hydrogen, I calculated the optimized unit cell volume with all the atoms and unit cell size and shape allowed to relax. The results showed that with one interstitial H atom in the supercell, the unit cell is slight expanded compared to its original shape. For instance, the volume of the expanded FeS unit cell is about 105% to its original volume. However, the binding energies of interstitial hydrogen do not change much after the relaxation of the

unit cell. For FeS, the changes of the binding energies are less than 0.02 eV. Similar effects were observed for other sulfides that allowing the unit cell to relax did not change the binding energies much. Therefore, I used the data mentioned above from calculations without volume relaxation for further discussions.

Table 4.3: The average displacement in Å of the nearest metal or sulfur atoms caused by interstitial hydrogen binding in metal sulfides.

		Metal	Sulfur			Metal	Sulfur
FeS	Site A	0.33	0.37	FeS_2	Site A	0.41	0.37
	Site B	0.30	0.26		Site B	0.24	0.40
	Site C	0.42	0.46	NiS_2	Site A	0.43	0.37
VS	Site A	0.28	0.28		Site B	0.23	0.41
	Site B	0.26	0.25	ScS	Site A	0.24	0.25
	Site C	0.30	0.21		Site B	0.23	0.24
CrS	Site A	0.32	0.38	Pd_4S	Site A	0.12	0.13
	Site B	0.29	0.23		Site B	0.15	0.17
	Site C	0.43	0.47		Site C	0.13	0.18
NiS	Site A	0.32	0.37		Site D	0.15	0.14
	Site B	0.30	0.28		Site E	0.16	0.17
	Site C	0.40	0.41				
NbS	Site A	0.35	0.37				
	Site B	0.30	0.29				
	Site C	0.40	0.43				

4.3.4 Interstitial H-H interaction in FeS and VS

In previous research, most reports regarded the interstitial H as individual adsorbates due to the low solubility of H in pure metals under practical conditions.[25] High interstitial H concentration was reached only at high H_2 pressure and leads to the formation of metal hydride or hydrogen-vacancy clusters. My DFT calculations, however, revealed that both FeS and VS have a highly favorable binding site, site A, which indicates high hydrogen solubilities. As a result, interstitial H-H interactions must be considered for further solubility and diffusivity calculations.[22] I used DFT to compute the interaction energy of possible H-H pairs with the H atoms located in nearby interstitial sites A using

$$E_a = E_{H-H-MS} - 2E_{H-MS} + E_{MS}. \qquad (4.2)$$

Here, E_{H-H-MS}, E_{H-MS} and E_{MS} are the total energy of metal sulfides with two interstitial hydrogen atoms, with one interstitial hydrogen atom and without interstitial hydrogen, respectively.

There are three configurations that are possible to put two hydrogen atoms in one unit cell in my calculations, I-II, I-III, I-IV, as illustrated in Figure 4. 5. With one interstitial H atom at site I, metal atoms 2 and 3 become closer to the H atom while metal atoms 5 and 6 move further away. On the other hand, with one interstitial hydrogen atom at site II, metal atoms 5 and 6 become closer while metal atoms 2 and 3 move further away. Therefore, if H atoms are present in both sites I and II, the lattice distortions associated with the individual interstitials have opposite trends, making the structure unstable compared to having the interstitials well separated. The interaction energy for this situation was calculated to be 2.98 eV for FeS and 3.02 eV for VS, so the

simultaneous occupation of these sites is extremely unfavorable. A similar argument indicates that simultaneous occupation of sites I and III is unfavorable. The interaction for this case was calculated to be 2.53 eV and 2.71 eV for FeS and VS, respectively.

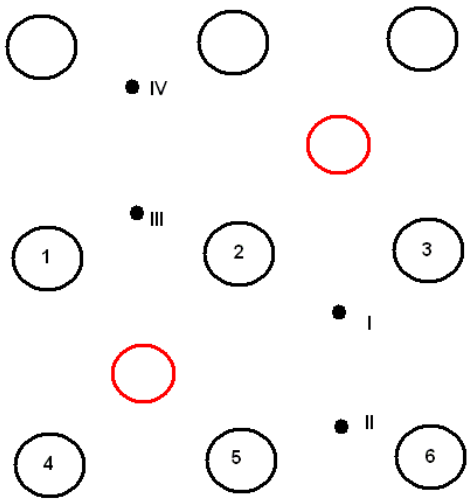

Figure 4.5: Illustration of FeS or VS viewed along a axis, with fmy locations for H binding site A labeled I-IV. The large black (red) circles indicate M (S) atoms.

If an interstitial H atom is located at site IV in Fig. 4. 5, the lattice distortion induced by this interstitial increases the distance between M atoms 2 and 3. The overall trend in this case is to make the simultaneous occupation of sites I and IV favorable. My calculations showed that the interaction energy is -0.04 eV and -0.03 eV for FeS and VS, respectively. This small attractive interaction energy is similar in size to the results that have been reported for pairs of interstitial H atoms in several hcp metals.[26]

My results are consistent with the Westlake criterion, a rule of thumb that two nearby interstitial sites cannot be simultaneously occupied by H atoms if the distance

between the sites is less than 0.21 nm.[27] For occupation of I-II and I-III, the H-H distances are 1.78 Å and 1.80 Å for FeS, 1.80 Å and 1.84 Å for VS. For I-IV binding, the distance is 3.15 Å and 3.21 Å for FeS and VS, respectively.

4.4 H solubility in metal sulfides

I used the results above to predict the solubility of H in metal sulfides. Once the site energies were defined, H solubility can be obtained with a direct statistical mechanics calculation in the limit of low interstitial H concentrations.[3, 28, 29] Interstitial sites in the solid are treated as independent three-dimensional harmonic oscillators in equilibrium with gaseous phase.[3] The solubility can thus obtained from the equilibrium between the gaseous H_2 and interstitial H phase. A detailed discussion on calculating the solubility can be found in Chapter II and V. For FeS and VS, I included the strong repulsion between nearby interstitial sites by assuming that only half of the sites can be occupied. I verified the accuracy of this assumption by performing Grand Canonic Monte Carlo (GCMC) simulations for these two sulfides using the interaction energies calculated above.

In Fig. 4.6, I show the concentration of hydrogen in metal sulfides in equilibrium with 1 atm of gaseous H_2. For comparison, I also listed experimental observations for the solubilities of H in some metals in Table 4. 3. As was already clear from the binding energies of the interstitial sites in Fig. 2, FeS and VS can take up large amounts of interstitial H, Pd_4S has lower H solubility than FeS, VS, CrS and NiS. All the other metal sulfides I considered have extremely low solubilities. For Fe, V and Ni, the solubility in

FeS, VS and NiS is higher than in pure Fe, V and Ni, while the solubility in NbS is lower than in pure Nb.

As might be anticipated from the results above, my calculations suggest that hydrogen atoms form an ordered structure in FeS and VS in equilibrium with moderate H_2 pressures and temperatures. As mentioned above, no crystal structure that simultaneously includes any of the metals I have considered here, sulfur, and hydrogen are reported in the Inorganic Crystal Structure Database, a comprehensive compilation of experimentally determined crystal structures. It is possible that the very slow diffusion of interstitial H in FeS and VS could place strong kinetic limitations on the formation of the ordered structures suggested by my calculations. I will discuss this in the following part of this chapter.

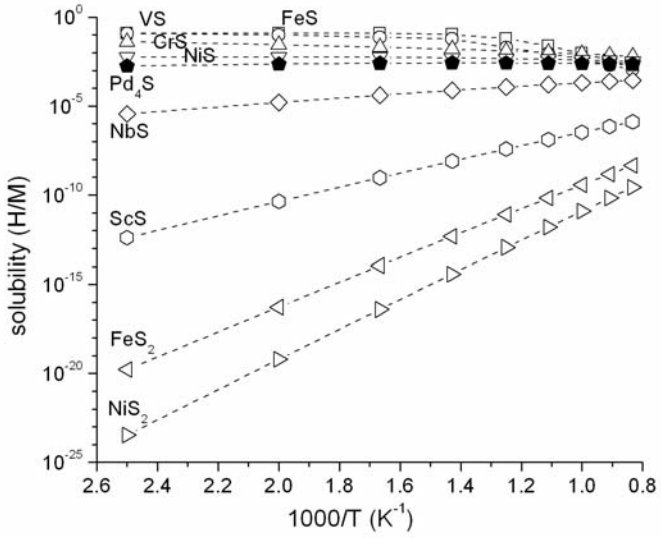

Figure 4.6: Concentration (H/Metal) of hydrogen in metal sulfides in equilibrium with 1 atm H_2.

Table 4.4: Experimental data for the solubility and permeability of H in several pure metals.[29, 30]

metal	H solid concentration in equilibrium with hydride at T = 300 K (H/metal)	H_2 permeability at T= 773 K (mol/m·s·$Pa^{0.5}$)
V	0.5	1.6×10^{-6}
Fe	3×10^{-8}	1.8×10^{-10}
Ni	$<7.6\times10^{-5}$	7.8×10^{-11}
Pd	0.03	1.9×10^{-8}
Nb	0.07	5.0×10^{-7}

4.5 H diffusion in metal sulfides

After examining the H solubility in each metal sulfide, I now turn to the diffusion of interstitial hydrogen in these metal sulfides. I only consider the diffusion of interstitial H in the limit of dilute concentrations for each material, including FeS and VS. The effect of high H concentration in these two sulfides will only be discussed qualitatively.

First I will discuss H hopping in the $B8_1$ structures. In this structure, each A site is connected with three B sites and three C sites, each B site is connected with one C site and two A sites, and each C site is connected with one B site and two A sites. I used the NEB method to calculate all possible hopping barriers in FeS, as listed in Table 4. 5. It is seen that hopping between site A to site B will dominate the diffusivity, since it has the lowest activation energy barrier and this path can lead to net diffusion between the energetically favored A sites. For VS, CrS and NbS, I only calculated the hopping barrier

between site A and site B. In FeS and VS, the energy at the transition state for this process is still lower than the energy at site C, which confirms that a higher activation barrier for hopping between site A and C makes this process much slower than hopping between site A and B. The relative energies of sites B and C in CrS and NbS indicate that this treatment is also appropriate in these cases. The only exception here is NiS, which has a similar binding energy at site B and site C. Thus I calculate the activation energy barriers for both A to B and A to C hopping. The results showed that the most favorable path is still hopping from A to B while the barrier for A to C hopping is 0.23 eV higher than A to B hopping. This indicates that both A to B and A to C hopping will contribute to the diffusion in NiS.

Now I turn to the other sulfides I examined. In FeS_2, NiS_2 and ScS, all possible hopping paths were calculated. In FeS_2 and NiS_2, each A site is connected with three A sites and one B site, while each B site is connected with fmy A sites. There are two possible hopping paths, A → B → A and a direct hop from site A to another A. In ScS, each A site is connected with two B sites while each B site is connected with six A sites. There is only one hopping path, A → B → A. All possible activation energy barriers were examined using NEB calculations.

In Pd_4S, each tetrahedral site has fmy neighboring sites. For example, site A is connected to fmy B sites and site B is connected to one A site, one B site, one C site and one D site. Complete information on how these interstitial sites are connected is listed in Table 4.2. In my calculation, I considered the hopping of hydrogen between the most stable sites, that is, hops from site A to a nearby site of the same type. There are several

possible hopping paths between A sites, among which the minimum energy path (MEP) is A→C→C→A. The net activation energy barrier for this path is 0.28 eV.

To summarize the results from my NEB calculations, I listed the hopping barriers in each metal sulfide in Table 4.5. Once the transition states were located, I then calculate the self diffusivity at dilute concentration along the *a* axis, D_x, (for all sulfides) and along the *c* axis for sulfides with hexagonal or tetragonal structure, D_z.[31] I approached this task by applying the theory developed by Braun and Sholl. In their theory, the diffusion of atoms is considered to be a random walk corresponding to a Poisson-Markoff process. The self diffusivity is related to the site to site hopping rates, *k*, and the structure of the crystal. A detailed description of their theory can be found in Chapter II. The site to site hopping rates in their equations were calculated using quantum corrected harmonic transition state theory:[25]

$$k = \frac{\prod_{i=1}^{3} f(h\nu_i / 2k_bT)}{\prod_{j=1}^{2} f(h\nu_j^{TS} / 2k_bT)} \exp(-E_a / k_bT) \qquad (4.3)$$

Here E_a is the zero point energy corrected activation energy barrier, ν_i, ν_j^{TS} are the vibrational frequencies of hydrogen at the interstitial sites and transition states, respectively, k_b is Boltzmann's constant, h is Planck's constant, T is temperature and $f(x) = \sinh(x)/x$. to calculate the self diffusivity at dilute concentration This is an analytic method for calculating the net diffusion coefficient of a species within a periodic geometry once the individual hopping rates between sites within the primitive cell of the material are known. For hexagonal structures, the overall self diffusivity is calculated as

$D = \sqrt{3D_x^2 + D_z^2}$ For tetragonal structure, $D = \sqrt{2D_x^2 + D_z^2}$ and for cubic structures, $D = \sqrt{3}D_x$.

The net self diffusivities calculated from these site to site hopping barriers are shown in Fig. 4. 7. This figure also shows selected experimental results for H diffusion in pure metals. For all metal sulfides except Pd_4S the diffusion of hydrogen is very slow. For example, at 500 K, the H diffusivity in Fe is fmy orders of magnitude higher than in FeS_2 and eight orders of magnitude higher than in FeS. For Pd_4S, the diffusivity is about 1-2 orders of magnitude lower than Pd at temperatures I considered. In order to check which hopping path contributes the most in each metal sulfide, I compared the net activation energy barrier of MEP with the net diffusion barrier in Table 4. 6. The latter comes from the interpolation of the diffusivity data as

$$D = D_0 \, \mathrm{e}^{-E_{dif} f / k_b T} \qquad (4.4)$$

Here D and E_{diff} is the net diffusivity and diffusion barrier, respectively and D_0 is the pre-exponential factor. I notice that for most metal sulfides, the net diffusion barrier is very similar or equal to the net activation energy barrier of MEP. The only exception here is Pd_4S, in which the difference between these two barriers is 0.06 eV. It indicates that in Pd_4S besides the minimum energy path A→C→C→A, an alternative path A→C→B→C→A with a net activation energy barrier 0.35 eV also contributes significantly to the net diffusivity.

As stated above, my calculated diffusivities are valid at dilute interstitial concentrations. As a high repulsion exists in FeS and VS between interstitial H at site I and site III, and at site IV and site III as illustrated in Fig. 4.5, a higher energy barrier is expected when one H atom hopes from site I to site III with the existence of another H

atom at site IV. It seems likely that H-H interactions that are present in FeS and VS act to reduce the diffusivity of H at non-dilute loadings, so it is likely that H diffusivity in FeS and VS in equilibrium with moderate pressures of H_2 is even lower than the values shown in Fig. 4. 7.

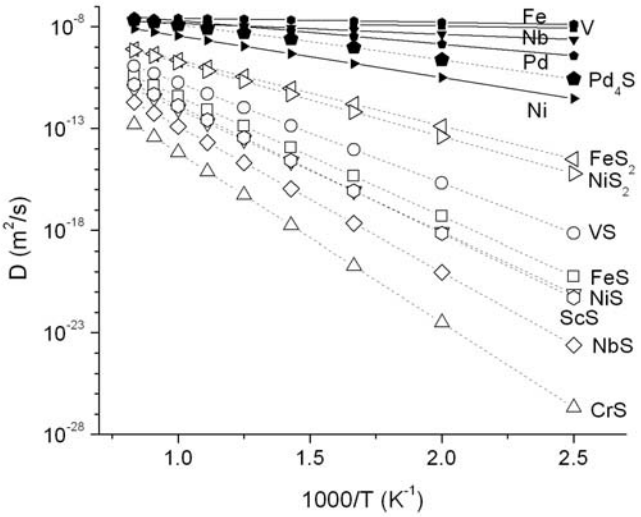

Figure 4.7: Diffusivity of interstitial H in metal sulfides as calculated using DFT. H diffusivities in selected metals from experimental measurements are also shown.[29]

4.6 H permeability in sulfides

With the assumption that the permeation of hydrogen is dominated by bulk diffusion, H permeability through a dense material can be calculated as a product of solubility and diffusivity.[3, 29] If additional resistances to net hydrogen transport exist, for example surface processes that limit H_2 dissociation or recombination, a material's permeability is lower than an estimate based on bulk solubility and diffusivity alone.[32, 33] Figure 4.8 shows the calculated H permeabilities in the metal sulfides based on

considering bulk diffusion of interstitial H as the rate determining process. For every sulfide, the predicted permeability is low, mainly due to the low diffusion of hydrogen.

Table 4. 5. Activation energy barriers (E_a) for H hopping in metal sulfides.

Metal sulfides	Hopping path	E_a (eV)	Metal sulfides	Hopping path	E_a (eV)
FeS	A→ B	1.05	FeS_2	A→B	0.64
	B→ A	0.11		B→A	0.41
	A→ C	1.74		A→A	0.73
	C→ A	0.42	NiS_2	A→B	0.72
	C→ B	1.02		B→A	0.55
	B→ C	1.43		A→A	0.84
VS	A→B	0.98	ScS	A→B	1.17
	B→A	0.40		B→A	0.41
CrS	A→B	1.45	Pd_4S	A→C	0.12
	B→A	1.05		C→A	0.01
NiS	A→ B	1.20		C→C	0.16
	B→ A	1.04		C→E	0.23
	A→ C	1.43		E→C	0.16
	C→ A	1.19		C→B	0.24
	A→B			B→C	0.30
	B→A			E→B	0.15
NbS	A→ B	1.22		B→E	0.27
	B→ A	0.34		E→D	0.20
				D→E	0.24
				B→D	0.25
				D→B	0.17

Table 4. 6. The pre-exponential factor (D_0) and diffusion barrier (E_{diff}) interpolated use Eq. (4.4), and the net activation energy barrier of the MEP ($E_{a,net}$) in all metal sulfides.

	D_0 (10^{-7} m^2/s)	E_{diff} (eV)	$E_{a,net}$ (eV)
FeS	15.3	1.06	1.05
VS	13.7	0.98	0.98
CrS	2.45	1.45	1.45
NiS	9.69	1.20	1.20
NbS	17.5	1.23	1.22
FeS_2	4.10	0.64	0.64
NiS_2	7.35	0.72	0.72
ScS	2.96	1.17	1.17
Pd_4S	5.47	0.28	0.34

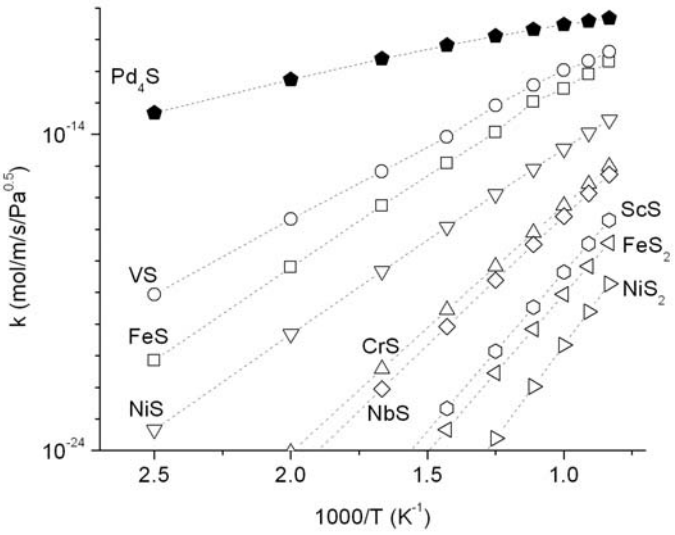

Figure 4.8: Permeability of hydrogen in metal sulfides.

At least two phenomena appear to dominate the low permeability of H through metal sulfides. First, in most of the sulfides, the binding energy differences between adjacent interstitial sites are large. When this occurs, the net activation energy for H diffusion has to be very large, regardless of the solubility of H in the material. Only NiS and Pd_4S do not fit this qualitative description. A second factor in almost all the materials I examine is the large local lattice distortions that are caused by interstitial H in NiS. For example, the nearest Ni atoms have to move 0.53 Å during hopping of an H atom from site A to site B. This large change suggests that the activation energy for this process is large, as indicated by my direct calculations of this quantity. It is noteworthy than there is less local lattice distortion during hopping in Pd_4S than in any of the other sulfides I examined. For hopping from the most favorable site to its neighboring site, the next most favorable site, Pd atoms only move 0.15 Å. In FeS_2, for the hopping between site A and

site B, the average movement of nearest atoms during hopping between site A and B is 0.29 Å, while in ScS, the movement is 0.27 Å. These movements are associated with activation energy barriers higher than the barrier in Pd_4S while lower than in $B8_1$ sulfides.

The main motivation for this study was to explore the possibility of using metal sulfides as hydrogen purification membranes. To check the accuracy of my calculation method, I compared the result for Pd_4S with the experimental estimation, and found that my calculations give a result about 7 times lower than the experimental estimations. It indicates that my results are sufficiently accurate to further discuss the possibility of using these metal sulfides as H separation materials. To finish this discussion, I compare the properties of the metal sulfides shown in Fig. 8 with pure metal membranes. The H permeabilities of several pure metals (for pure H_2 streams) are listed in Table 3. For all metal sulfides I considered, the predicted permeability is orders of magnitudes lower than even the pure metals such as Ni that would usually be considered to be poor membrane materials. That is, my results strongly suggest that the kinds of metal sulfides I have examined here show no promise whatsoever as membrane materials for purifying H_2. Instead, several of these sulfides appear to be good candidate materials for barrier coatings in situations where permeation of hydrogen is undesirable.

4.7 Conclusion

In this chapter, I discussed how to use first-principles calculations to evaluate the permeation rate of hydrogen through crystalline metal sulfides, for which no experimental information available currently. If metal sulfides with high permeation rates could be identified, they could have potential applications as membranes for high

temperature H_2 purification from sulfur-containing streams. I have described first-principles calculations of solubility and diffusion of interstitial H in nine metal sulfides with non-layered crystal structures. In every case, the hydrogen permeance predicted by my calculations is low compared to pure metals. For the only metal sulfides for which prior permeation data was available, Pd_4S, the calculated permeability is in reasonable agreement with the experimental data. However, its permeability is still below the requirement of practical applications.

My calculations assumed that diffusion of interstitial H through each metal sulfide was the rate-limiting process in net transport of hydrogen through a film of each material, and this diffusion occurred by site to site hopping between interstitial sites. One possible direction for future modeling of these materials would be to consider other sources of resistance to mass transport through films of this kind, similar to my earlier work on thin metal alloy films.[32, 33] Because including surface resistances will further decrease the net hydrogen permeability, including these effects will not change my qualitative conclusion that the metal sulfides are not suitable for use as membrane materials.

The low permeation rates of hydrogen through metal sulfides are mainly a result of the very slow diffusivity of interstitial H in these materials. At low and moderate temperatures (that is, room temperature and below), it is possible that quantum mechanical tunneling effects may contribute to the net diffusion of interstitial H. Although estimates of tunneling effects can be made using information from DFT calculations[34], I have not examined these effects here. Because the diffusivities predicted from my calculations that examined only activated hopping over the barriers between interstitial sites are so low, it is extremely unlikely the enhancements in these

rates associated with tunneling would be large enough to increase H permeation to levels of any interest in practical membrane applications.

4.8 Reference

[1]M. Kajiwara, S. Uemiya, T. Kojima Int. J. Hydrogen. Energy 24 839 (1994)

[2]B. H. Howard, R. P. Killmeyer, K. S. Rothenberger, A. V. Cugini, B. D. Morreale, R. M. Enick, F. Bustamante J. Membr. Sci. 241 207 (2004)

[3]P. Kamakoti, B. D. Morreale, M. V. Ciocco, B. H. Howard, R. P. Killmeyer, A. V. Cugini, D. S. Sholl Science 307 569 (2005)

[4]M. Mundschau, X. Xie Catal. Today 118 12 (2006)

[5]U. Feuerriegel, W. Klose, S. Sloboshanin, H. Goebel, J. Schaefer Langmuir 10 3567 (1994)

[6]B. D. Morreale, B. H. Howard, O. Iyoha, R. M. Enick, C. Ling, D. S. Sholl J. Membr. Sci. 46 6313 (2007)

[7]M. E. Grillo, C. Stampfl, W. Berndt Surf. Sci. 317 84 (1994)

[8]S. Speller, T. Rauch, J. Bomermann, P. Borrmann, W. Heiland Surf. Sci. 441 107 (1999)

[9]V. R. Dhanak, A. G. Shard, B. C. Cowie, A. Santonic Surf. Sci. 410 321 (1998)

[10]J. A. Rodrigez, S. Chaturvedi, T. Jirsak Chem. Phys. Lett. 430 176 (1998)

[11]H. Gao, Y. S. Lin, Y. Li, B. Zhang Ind. Eng. Chem. Res. 43 6920 (2004)

[12]M. L. Burke, R. J. Madix Surf. Sci. 237 1 (1990)

[13]F. J. Castro, G. Meyer, G. Zampieri J. Alloys Compd. 330-332 612 (2002)

[14]P. Raybaudyz, G. Kressey, J. Hafnery, H. Toulhoatz J. Condens. Matter 9 11085 (1997)

[15]P. Raybaudyz, G. Kressey, J. Hafnery, H. Toulhoatz J. Condens. Matter 9 11107 (1997)

[16]J. H. Wang, Z. Cheng, J. L. Bréas, M. Liu J. Chem. Phys. 127 214705 (2007)

[17]Z. Wang, T. Gu, K. T. Tada, S. Watanabe J. Chem. Phys. 128 014704 (2008)

[18]D. C. Sorescu, D. S. Sholl, A. V. Cugini J. Phys. Chem. B 108 13115 (2004)

[19]G. Kresse, J. Hafner Phys. Rev. B 48 13115 (1993)

[20]The Inorganic Crystal Structure Database (ICSD). (http://www. fiz-informationsdienste.de/en/DB/icsd/.)

[21]F. Gronvold, E. Rost Acta. Cryst. 15 11 (1962)

[22]S. Q. Hao, D. S. Sholl Energy Envir. Sci. 1 175 (2008)

[23]G. Henkelman, B. P. Uberuaga, H. Jonsson J. Chem. Phys. 113 9901 (2000)

[24]S. Q. Hao, D. S. Sholl J. Phys. Condens. Matter 21 115402 (2009)

[25]P. Kamakoti, D. S. Sholl Phys. Rev. B 71 014301 (2005)

[26]D. S. Sholl J. Alloys Compd. 462 446 (2007)

[27]D. G. Westlake J. Less Common Metals 91 1 (1983)

[28]C. G. Sonwane, J. Wilcox, Y. H. Ma J. Chem. Phys. 110 24549 (J. Phys. Chem. B)

[29]G. Alefeld, J. Volkl *Hydrogen in Metals II* (Springer-Verlag, Berlin, Heidelberg, New York, 1978),

[30]S. A. Steward *Review of hydrogen isotope permeability through materials* (U.S. Department of Commerce, Springfield,VA, 1983),

[31]O. M. Braun, C. A. Sholl Phys. Rev. B 58 14870 (1998)

[32]T. L. Ward, T. Dao J. Membr. Sci. 153 211 (1999)

[33]C. Ling, D. S. Sholl J. Membr. Sci. 303 162 (2007)

[34]B. Bhatia, D. S. Sholl Phys. Rev. B 72 224302 (2005)

Chapter V. Screening of PdCuAg ternary for H_2 purification

5.1 Introduction

One route to improving the performance of pure metal membranes is to develop metal alloys to achieve the multiple objectives required for successful membranes. Pd based binary alloys, for example, have been widely examined experimentally and theoretically, with Pd being the core material for binary alloy in combination with elements including cerium, copper, gold, iron, nickel, silver, yttrium.[1] Among these binary alloys, PdCu alloys are particularly interesting because these membranes may improve resistance to poisoning.[2] However, the permeability to hydrogen has been observed to decrease with Cu concentration in the alloys.[2, 3] Other binary alloys such as PdAg and PdAu have been shown to increase the permeability of hydrogen compared to pure Pd.[1, 4] However, there is no evidence that the resistance of contaminants relative to pure Pd is improved for these binary alloys. Based on these results, identification of Pd based alloys with considerable hydrogen flux and resistance of the contaminants is still required.

Although some experimental studies of Pd-based binary alloys have been reported, it is still challenging to experimentally screen a large series of alloys, since such efforts would require extremely large resources. In recent years, theoretical approaches based on first-principles calculations provide a complementary route to predict the performance of metal alloys in H_2 purification. Kamakoti and Sholl have developed an *ab initio* method to effectively examine the solubility, diffusivity and permeability of hydrogen in the bulk phase of PdCu alloys without any experimental input.[2, 3, 5] Sonwane recently used the

same method to examine PdAg and PdAu alloys.[6, 7] In this method, the calculations begin with the well known crystalline structure of PdCu alloys. The binding energies of hydrogen in the interstitial sites in PdCu alloys are calculated by Density Functional Theory (DFT). Once the binding energies of H in the interstitial sites are found, Sieverts' law relates the interstitial concentration of atomic H to the gas phase pressure. Diffusion of H in PdCu can be regarded as a series of hops between connected interstitial sites. The rate of individual hops can be computed using quantum corrected harmonic transition state theory.[5] Once the site to site hopping rate for a large connection of sites are known, the net diffusivity of the interstitial H can then be simulated with a Kinetic Monte Carlo (KMC) method. Finally, the membrane can be characterized by the permeability of hydrogen, which is defined as a product of the Sievert's constant and the diffusivity.

Kamakoti and Sholl's calculation showed that the predictions of the permeability of H in PdCu alloys were in good agreement with experimental data.[2] Subsequently, Semidey-Flecha and Sholl extend this method to examine a series of PdCuM alloys with M=Ni, Pt, Ag and Au.[8] Their work indicated that the permeability of PdCuAg is increased compared to PdCu alloys for at least some alloys. In this chapter, I will further extend these calculations in screening PdCuAg ternary alloys. I aim to find alloys with improved permeability compared to the binary PdCu alloys or even to pure Pd. I discuss the methods used in modeling ternary alloys, in Section 2. The computational details are given in Section 3. A series of PdCuAg ternary alloys with are then examined. I describe the solubility, diffusivity and permeability of hydrogen in these alloys in Section 4.

5.2 Method

5.2.1 Cluster expansion modeling

A key challenge in applying DFT calculations to describe interstitial H in alloys such as PdCu is that these substitutionally disordered materials have a plethora of structurally distinct binding sites. Kamakoti and Sholl approached this challenge in their PdCu screening by performing DFT calculations for H in a collection of distinct interstitial site, then fitting the observed results for the binding energies and transition state energies to a simple lattice model in terms of parameters that describe the local environment of each site.[3, 5] They assumed that, for example, the site energies were only affected by the number of Cu atoms in the nearest neighbor (NN) and next nearest neighbor (NNN) shell of the interstitial site.

This simplified model gave quite accurate results for simple binary systems such as PdCu, but it is unclear if it can be extended in the same form for ternary alloys. Recently, Semidey-Flecha and Sholl applied a more general model, the cluster expansion (CE), in describing the relationship between the binding energies and transition state energies of H in Pd alloys and the local environment of these site.[8] The CE model assumes that the total energy of a given configuration can be written as a linear combination of the energy of special clusters as

$$E = E_0 + \sum J_i^{(1)} \sigma_i^{(1)} + \sum J_i^{(2)} \sigma_i^{(2)} + \ldots \qquad (5.1)$$

where each $J_i^{(n)}$ is a parameter defining the energy of a cluster of *n* atoms, while the coefficient $\sigma_i^{(n)}$ can be obtained from the given configuration. This model must be truncated with some finite number of interactions. To determine which truncated model gives the most accurate prediction, I used the "Leave One Out" (LOO) method.[8] In the

LOO analysis, a possible truncated model is evaluated by performing least square minimization n times where n is the number of independent data. Each time one data point from the complete set of n data is "left out" and the LOO error, R_{LOO}, is defined as

$$R_{LOO}^2 = \frac{1}{n}\sum (E_{pred,k} - E_k)^2 \qquad (5.2)$$

Here E_k is the kth data point and $E_{pred,k}$ is the value for this data point predicted by the model fitted for all the data expect the kth data point. The LOO analysis provides a means to compare models with different number of parameters. In my study, truncated cluster expansion model with the lowest LOO error is used for future calculations with the alloys being discussed.

In the results presented below, DFT calculations are first performed in the examination of each alloy. The CE method is then used to model the data obtained from DFT calculations. Two criteria are used to test whether the CE model gives an accurate prediction. First, the cluster expansion model should not predict any interstitial site having binding energies lower than those sites for which DFT data is already available. This criterion ensures an accurate description for those sites with low binding energies dominating the H solubility. Secondly, the CE method should generate a distribution of site energies that does not significantly deviate from the connection of sites examined with DFT calculations. This criterion ensures an accurate description of the energy distribution. If either of these two criteria is not satisfied, additional DFT calculations are performed. After adding this data to the earlier DFT data, CE modeling is performed again. This procedure is continued until my DFT data set and the corresponding CE model are considered complete enough to provide useful information to model the entire range of interstitial sites in the alloy. Once the CE model is available, the net solubility

and diffusivity of H is calculated using the same methods already described for binary alloys in Chapter II.

5.2.2 DFT data for interstitial H

To describe the behavior of hydrogen in an alloy, a series of interstitial sites should be first examined using DFT calculations to provide enough information for further modeling. For example, Kamakoti et al. examined 58 octahedral (O) sites and over 100 tetrahedral (T) sites in their study of PdCu.[3] Semidey-Flecha examined 21 O sites and 88 T sites to screen $Pd_{96}M_4$ alloys.[8] The difference between binary and ternary alloys is that the latter alloys have many more possible interstitial sites as characterized by the arrangement of metal atoms in the shells around a site. One challenge in this research is thus how to effectively collect enough DFT data, especially for the transition states. The NEB method, which I used in my previous chapters to locate the transition states, first constructs a set of images of the system, typically on the order of 4-20 between the initial and final state.[9] Each image defines a separate configuration that must be treated in DFT. A spring interaction between adjacent images is added to ensure continuity of the path, thus mimicking an elastic band. An optimization of the band, involving the minimization of the force acting on the images, brings the band to the minimum energy path (MEP) and the saddle point along this path is located as the transition state. Locating one transition state thus includes simultaneous optimization of 4-20 images. This situation means it is impractical to perform NEB calculation for hundreds of transition states.

I developed a new method to improve the numerical efficiency of finding the transition states instead of performing NEB calculations. The starting point of this method is the observation that the transition states for interstitial H always lie close to the middle of the window of the set of three metal atoms that connects an O site and a T site. Based on this, the H position is initialized at the middle of the ideal window while the positions of metal atoms are initialized as the same as in the relaxed T site. When the initial position is close enough to a true transition state, a quasi-Newton optimization then leads to the saddle point. This method reduces the task of locating a transition state to one geometry optimization, thus saves at least 80% of calculation time (assuming only 5 images are used in NEB calculations). The vibrational frequencies of hydrogen are calculated in the final state to determine whether the geometry optimization converges to a transition state instead of a local minima site on the energy surface. A transition state, a saddle point on the energy surface, gives two real frequencies and one imaginary frequency, while a local minima state gives three real frequencies.

5.2.3 Scope of work

Previously, Semidey-Flecha and Sholl have studied the effect of a small amount of an additive metal, M, on the performance of PdCuM membranes. That work examined alloys with composition $Pd_{70.4}Cu_{25.9}M_{3.7}$ with M=Ag, Au, Pt and Ni, showing that adding Ni had a negative effect on H permeability, while adding Ag improves the permeability.[8] Previous reports on PdAg binary alloys also showed a positive effect on the permeability compared with pure Pd. Therefore, in this research, I examined a series of PdCuAg alloys with different Cu and Ag composition.

5. 3 Computational details

I performed DFT calculations using the Vienna ab initio Simulation Package (VASP) using the generalized gradient approximation with the PW91 functional to describe electron exchange-correlation effects in this study. Ion-electron interactions were described by ultrasoft pseudopotentials. A plane-wave expansion with a cutoff of 233.73 eV was used in all calculations. Geometry relaxations were performed with a conjugate gradient method until the forces on all unconstrained atoms were less than 0.03 eV/Å. A Monkhorst-Pack mesh with 4×4×4 k-points was used for all calculations.

The supercell I used contained 27 metal atoms and one H atom located in the interstitial site of the metal lattice. I assume that PdCuAg ternary alloys adopt the substitutional random fcc structure as in PdAg and PdCu with Pd composition no less than 55 at.%. Metal atoms were randomly distributed among the fcc lattice in the supercell. All atoms allowed to relax during the calculation, with the volume of the cell fixed at the optimized volume without the interstitial H.

Transition states for diffusion of hydrogen were determined using the method I introduced above. The vibrational frequencies of hydrogen were calculated in the harmonic approximation, assuming localized vibrations of hydrogen atom are decoupled from vibrations of metal atoms. Zero point energies of hydrogen (ZPE) are calculated as

$$ZPE = \frac{1}{2}\sum_i h\nu_i \qquad (5.3)$$

Here h is the Planck's constant, ν_i is the vibrational frequency of H. The summation takes on all possible real frequencies. A local minimum has three real frequencies while a transition state gives two real frequencies and one imaginary frequency.

5.4 Screening of PdCuAg alloys

5.4.1 Optimization of lattice constants

I chose to examine seven different PdCuAg ternary alloys: $Pd_{92.6}Cu_{3.7}Ag_{3.7}$, $Pd_{85.2}Cu_{3.7}Ag_{11.1}$, $Pd_{85.2}Cu_{11.1}Ag_{3.7}$, $Pd_{81.5}Cu_{11.1}Ag_{7.4}$, $Pd_{70.4}Cu_{11.1}Ag_{18.5}$, $Pd_{70.4}Cu_{25.9}Ag_{3.7}$ and $Pd_{66.7}Cu_{25.9}Ag_{7.4}$ For comparison, I also examine the performance of three PdAg binary alloys, $Pd_{96.3}Ag_{3.7}$, $Pd_{92.6}Ag_{7.4}$, $Pd_{81.5}Ag_{18.5}$ and three PdCu binary alloys, $Pd_{96.3}Cu_{3.7}$, $Pd_{88.9}Cu_{11.1}$, $Pd_{74.1}Cu_{25.9}$. All the compositions here and in my later discussions are given in units of at.%. Figure 5.1 shows the chosen compositions on a ternary composition diagram. In the phase diagram of PdCu binary alloys, alloys with less than 55 at% Pd have a bcc structure which shows no resistance to contaminants.[2] In my calculations, I limit the concentration of Pd to be higher than 66% for this reason.

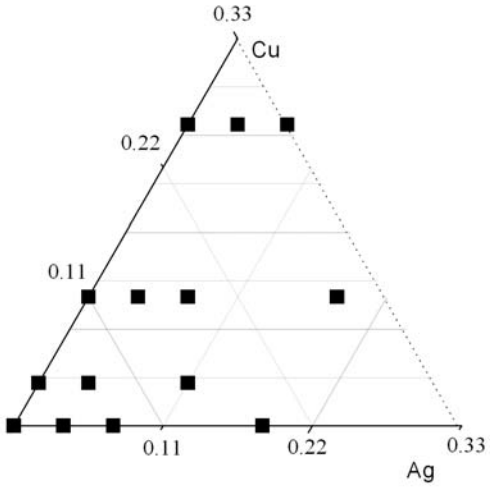

Figure 5.1: Compositions examined in my work shown on a ternary Pd-Cu-Ag composition diagram.

Geometry optimization was performed to get the lattice constant of each alloy without interstitial H. Table 5.1 lists the DFT-optimized lattice constant for each alloys I considered, including pure Pd. Substituting Ag for Pd expands the lattice since Ag has a larger atom size than Pd, and substituting Cu for Pd has the opposite effect due to the smaller size of Cu atom. In previous studies, Vegard's law was used to describe the lattice constants of Pd based binary alloys.[3] I find, however, that the lattice constants predicted by Vegard's law are only in moderate agreement with the value obtained from DFT calculations, which indicates that DFT optimization of the lattice constant is necessary to get an accurate result.

Table 5.1: Optimized lattice constant (LC) for PdCuAg alloys. The volume expansion is calculated as $\frac{V_{alloy}-V_{Pd}}{V_{Pd}}\times 100\%$, where V_{alloy} and V_{Pd} is the volume of the unit cell for the alloy and for pure Pd. For simplification I only list the concentration of Cu and Ag.

Cu/Ag (at.%)	LC (Å)	Volume expansion (%)	Cu/Ag (at.%)	LC (Å)	Volume expansion (%)
0/0	3.960	0.00	11.1/0	3.929	-2.33
0/3.7	3.970	0.76	11.1/3.7	3.937	-1.73
0/7.4	3.973	0.99	11.1/7.4	3.946	-1.06
0/18.5	3.992	2.44	11.1/18.5	3.964	0.30
3.7/0	3.953	-0.53	25.9/0	3.896	-4.77
3.7/3.7	3.955	-0.38	25.9/3.7	3.899	-4.55
3.7/11.1	3.973	0.99	25.9/7.4	3.902	-4.33

5.4.2 CE models for selected PdCuAg alloys

To characterize the behavior of interstitial hydrogen in PdCuAg alloys, one H atom is first located at an interstitial site and the whole structure is optimized by allowing all metal atoms and H atom to relax. Two possible interstitial sites exist in fcc structures: the octahedral site (O site) and the tetrahedral site (T site). For each supercell I considered, I calculated the binding energies of H in all possible interstitial sites in the supercell, as well as the energy of all transition states between adjacent O and T sites. The cluster expansion method is then applied to model the data obtained from DFT calculations. This process is repeated until the CE model satisfies those two criteria discussed in Section 5.3. A similar process is applied for the zero point energies. In the Appendix, I have listed the LOO error for each alloy, as well as the number of sites examined in my DFT calculations.

To check how well CE predicts the data compared with DFT calculations, the same table also listed the least square error of each CE model, R_{LS}, defined as:

$$R_{LS}^2 = \sqrt{\frac{\sum_{i=1}^{n} (E_i^{CE} - E_i^{DFT})^2}{n}} \qquad (5.4)$$

here E_i^{CE} and E_i^{DFT} are the *i*th data predicted by the CE model and by DFT calculations, respectively. For all the alloys I consider, the least squares errors are smaller than 0.015 eV and the LOO error is smaller than 0.020 eV, which indicates that my CE models give accurate predictions for the binding energies, as shown in the Appendix. In the Appendix, I also compare the distribution of site energies predicted by the CE model when applied to a large random volume and by DFT calculations, by plotting the cumulative probability of the site energies for each set of data. This comparison shows that there are

no significant deviances between the CE model and DFT calculations, indicating that my CE models can be used to describe the full set of interstitial sites and transition states in these alloys to calculate the macroscopic properties of interstitial H discussed below.

5.4.3 Solubilities of hydrogen in selected PdCuAg alloys

The method to calculate the solubility of H in PdCuAg alloys has been described in Chapter II. I first look at the solubilities for PdAg binary alloys, normalized by the value in pure Pd, as shown in Fig. 5. 2. The solubilities of hydrogen increase with the amount of Ag in the binary phase at fixed temperature, and this increase is more significant at low temperatures. At 600 K, the solubility of hydrogen in $Pd_{81.5}Ag_{18.5}$ is predicted to be 3.4 times higher than in pure Pd. The calculated results are proved to be in a good agreement with the experimental results from Holleck and Sakamotot et al., [4, 10] which further indicates that my model is capable for screening PdCuAg alloys. Sonwane and Ma recently used similar method to calculate the solubilities of hydrogen in PdAg alloys.[6, 7] They found that the solubilities of hydrogen increases with Ag concentration for alloys with less than 25 at.% Ag, which is also consistent with my observations.

Figure 5.3 shows the calculated solubilities of hydrogen in PdCuAg alloys, normalized by the solubilities in pure Pd. For comparison, I also showed the calculated solubilities of hydrogen in PdCu and PdAg binary alloys. The normalized solubility for each alloy at 800 K is shown in Fig. 5.4. A similar trend is observed for PdCuAg ternary alloys as for PdAg binary alloys. That is, the solubilities increase with Ag concentration in the alloys. This magnitude of this trend, however, becomes less significant at high Ag concentrations. Much of this trend can be understood in terms of lattice parameters of the

alloys. Since Ag is a larger atom than Pd, adding Ag in the alloy expands the lattice, as seen in Table 5.1. The free space for the interstitial hydrogen atom is increased due to the expanded lattice, which lowers the energies of interstitial H atoms. Therefore, the solubilities of hydrogen increase with Ag concentration in the alloy.

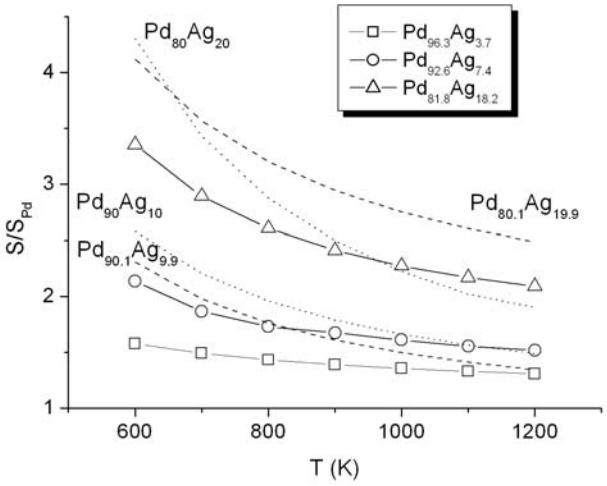

Figure 5.2: Predicted solubilities of hydrogen in PdAg alloys, normalized by the solubilities in pure Pd. The dotted experimental data for $Pd_{90}Ag_{10}$ and $Pd_{80}Ag_{20}$ came from reference 4. The dashed data came from reference 10.

To further understand the solubility trends in Fig. 5.4, I compared the distribution of binding energies in O sites, which contribute the most for the solubilities, generated by CE modeling for alloys with same Cu content but different Ag concentrations, as shown in Fig. 5.5. The comparison supports the conclusion I drew in the last paragraph that adding Ag favors the interstitial hydrogen; this occurs due to decreases in binding energies of the most stable sites. However, I also notice that besides these sites being more favorable, other sites become more unfavorable as the Ag content is increased.

Further examination revealed that the binding energies of H in O sites increase as the number of Ag atoms in the nearest neighbor shell increases. This can be understood in terms of the atom size; having more Ag atoms in the NN shell decreases the free space available for the interstitial H atom relative to a cage with fewer or no Ag atom in the NN shell. This observation implies that adding Ag in the alloy causes two different effects. First, Ag atom expands the lattice, which is favorable for H occupation. Secondly, with more Ag content in the alloy, more interstitial sites have one or more Ag atom in its nearest neighbor shell, which is unfavorable for the interstitial hydrogen. The overall solubility is the result of the interplay of these two effects.

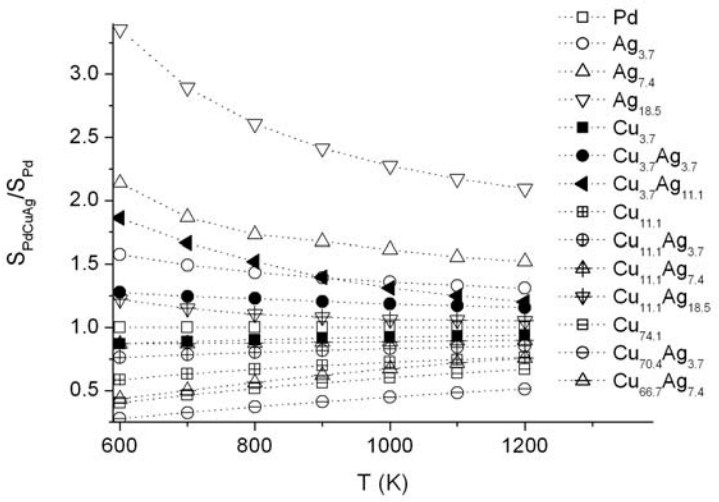

Figure 5.3: Predicted solubilities of hydrogen in PdCuAg alloys, normalized by the solubilities in pure Pd. For simplification only the concentration of Cu and Ag are listed in the label.

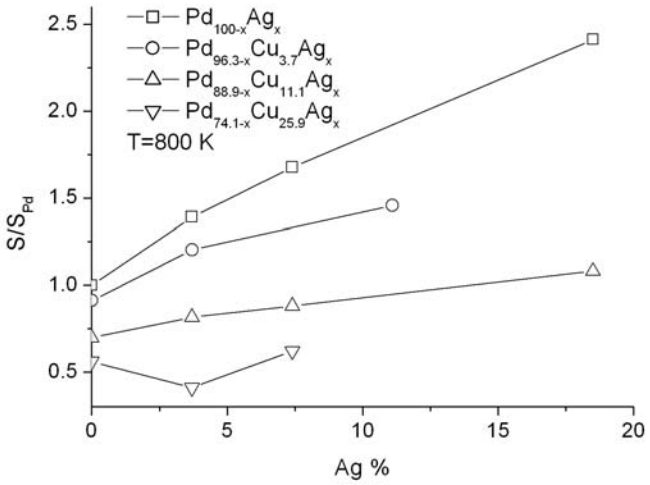

Figure 5.4: Predicted solubilities of hydrogen in PdCuAg alloys at 800 K, normalized by the solubilities in pure Pd.

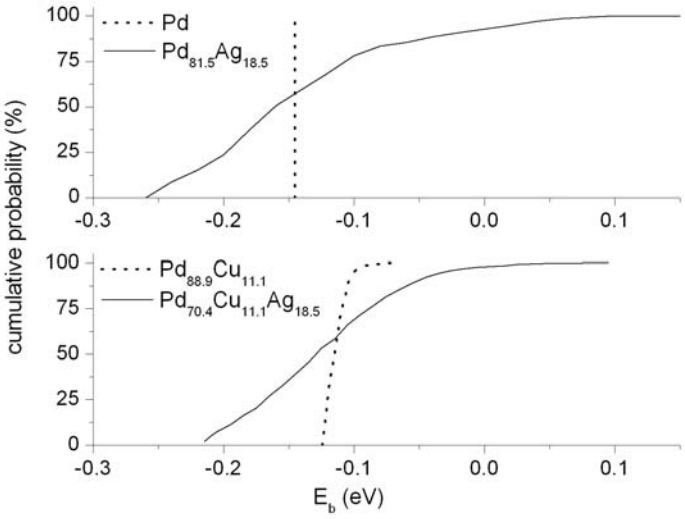

Figure 5.5: The cumulative probability distribution of binding energies in O sites for different PdCuAg alloys predicted from CE models.

In Fig. 5.6, I compare the solubilities in PdCuAg alloys normalized by the values in PdCu binary alloys with the same Cu concentration. Although adding Ag increases the solubility, this increase is more significant for alloys with lower Cu content. This phenomenon can be understood by analyzing the distribution of binding energies in O sites in the alloys. For example, in Fig. 5.5, I showed the effect of adding 18.5% Ag on the binding energies for alloys with different Cu content. For alloys with no Cu, adding 18.5% Ag decreases the binding energy at the most stable site from -0.14 to -0.26 eV, while it only decreases from -0.13 eV to -0.21 eV in the alloys with 11.1% Cu. Since the solubilities are dominated by the sites with the lowest the binding energies, the more negative binding energy indicates higher solubility. Thus, the increase in the solubility associated with Ag concentration is more significant for alloys with less Cu content.

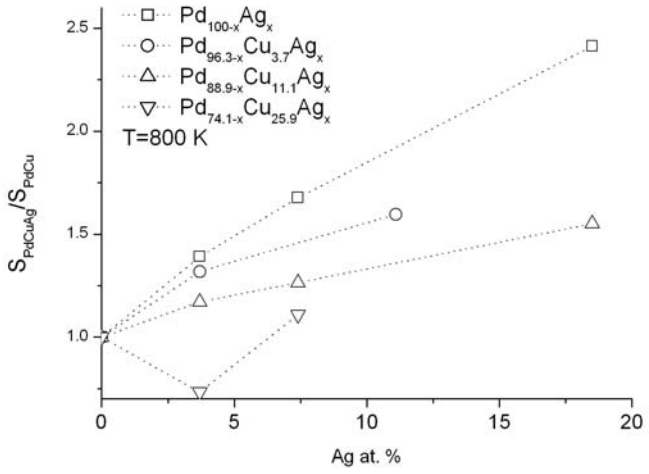

Figure 5.6: Predicted solubilities of hydrogen in PdCuAg alloys at 800 K, normalized the value in PdCu binary alloy with the same Cu concentration.

After obtaining the solubilities for the PdCuAg alloys shown in Fig. 5.1, I interpolate the solubilities for other PdCuAg alloys using a cubic order spline function to fit the calculated data. The maximum concentrations of Cu and Ag are limited to be 25.9 % and 18.5%, respectively. The Pd concentration is limited to be no less than 66.7% in the interpolation. Figure 5.7 shows the interpolated contour map of the solubility normalized by the value in pure Pd from my calculations at 800 K. All compositions above/below the solid line in Fig. 5.7 indicate lower/higher solubilities than pure Pd. The alloys with high solubility typically contain more Ag than Cu. The highest normalized solubility at 800 K is about 2.2 times to the value in pure Pd; this result occurs for a binary PdAg alloy.

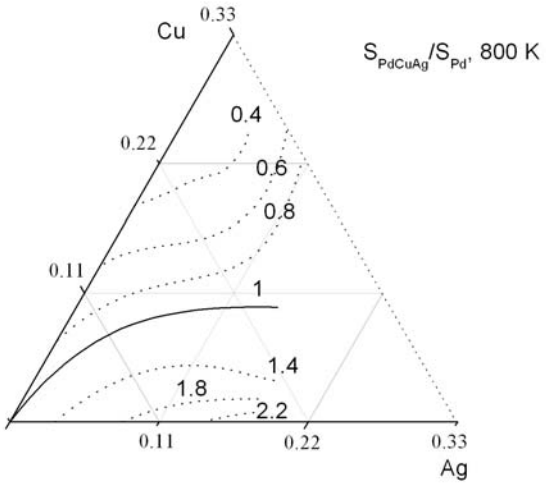

Figure 5.7: Contour map of the predicted solubility of hydrogen in PdCuAg alloys normalized by the value in pure Pd at 800 K.

5.4.4 Diffusivities of hydrogen in selected PdCuAg alloys

After the CE models for the site energy at the O sites, T sites and the transition states were available, I performed Kinetic Monte Carlo simulations to get the net diffusivity of hydrogen in PdCuAg alloys as described in Chapter II. I first compare my calculated results for PdAg binary alloys with experimental reports. In Fig. 5.8, I show the calculated diffusivities for $Pd_{96.3}Ag_{3.7}$, $Pd_{92.6}Ag_{7.4}$ and $Pd_{81.5}Ag_{18.5}$, normalized by the value in pure Pd. Experimental results for $Pd_{90}Ag_{10}$ and $Pd_{80}Ag_{20}$ are also shown in the same graph.[4, 10] Both the experiments and theoretical calculations show an opposite trend from what is observed for the solubilities, namely, the diffusivities of H decrease as the content of Ag increases in the alloy. For example, at 600 K, my calculations give the normalized diffusivities of 0.98, 0.94 and 0.72 for $Pd_{96.3}Ag_{3.7}$, $Pd_{92.6}Ag_{7.4}$ and $Pd_{81.5}Ag_{18.5}$, respectively. This trend is consistent with experimental reports, as shown in Fig. 5.8.

Figure 5.9 shows the diffusivities of hydrogen in PdCuAg ternary alloys, normalized by the value in pure Pd. The results for PdAg and PdCu binary alloys are also shown in the same graph. Figure 5.10 shows the normalized diffusivity at 800 K. For alloys with no or low Cu content, the diffusivity decreases with Ag concentration in the alloy. For alloys with high Cu content, however, the diffusivity first increases with Ag concentration, then decreases at high Ag concentration.

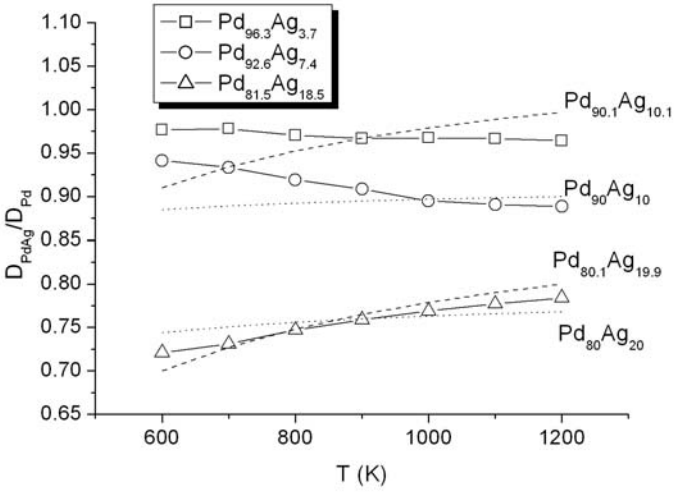

Figure 5.8: Predicted diffusivities of hydrogen in PdAg binary alloys, normalized by the diffusivities in pure Pd. The dotted data came from reference 4. The dashed data came from reference 10.

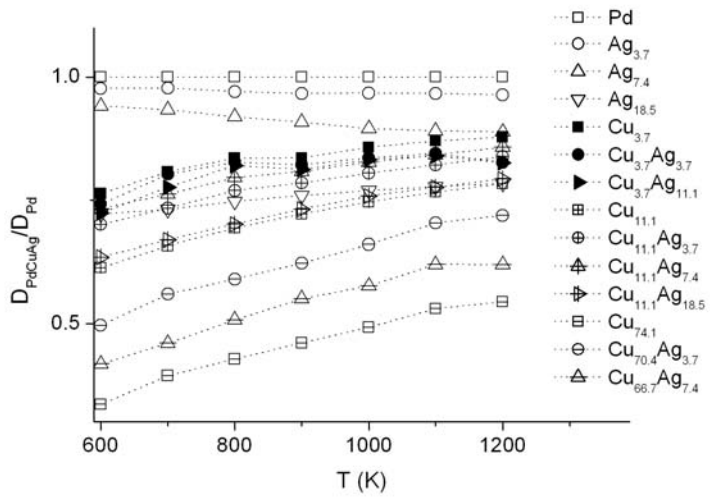

Figure 5.9: Predicted diffusivities of hydrogen in PdCuAg alloys, normalized by the diffusivities in pure Pd. For simplification only the concentration of Cu and Ag are listed in the label.

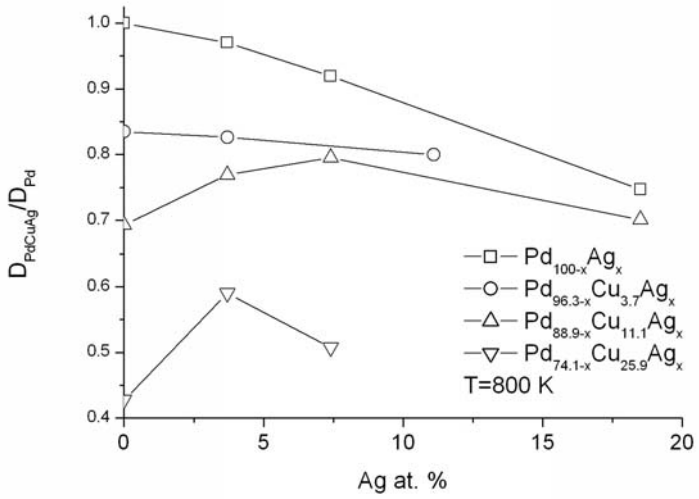

Figure 5.10: Predicted diffusivities of hydrogen in PdCuAg alloys at 800 K, normalized by the diffusivities in pure Pd.

Unlike the solubility, which is determined directly by H binding in the interstitial sites, the diffusivity is affected by both the binding energies and the barrier heights for individual hops. To understand the effect of adding Ag on the diffusivity of hydrogen in PdCuAg alloys, I applied an average jumping rate theory (AJRT) [11] to my systems, a approximate theory that can be solved semi-analytically. In AJRT, the diffusivity, *D*, is proportional to an average hopping rate, $\bar{\Gamma}$, and the mean square displacement per jump.[11] In fcc structures, this relationship can be described as:

$$D = \frac{1}{24}\bar{\Gamma}a^2 \tag{5.5}$$

where *a* is the lattice constant. The average jumping rate is approximated by:

$$\bar{\Gamma} = \frac{8\Gamma_0 \int p(E)N_s(E)dE \int N_b(E')e^{-(E'-E)/k_bT}dE'}{\int p(E)N_s(E)dE} \tag{5.6}$$

Here, k_b is the Boltzmann's constant and T is the temperature. Γ_0 is a pre-factor that can be assumed to be a constant for all alloys, and $p(E)$ is the probability of occupying a site with energy E. This distribution obeys the Fermi-Dirac distribution as:

$$p(E) = \frac{1}{e^{(E-\mu)/k_bT} + 1} \tag{5.7}$$

where μ is the chemical potential of H.

The functions N_s and N_b in Eq. (5.5) are the normalized distribution of the binding energies and barrier energies, respectively. Because I aim to use the AJRT to get physical insight into the diffusion process, I used simplified models for these functions rather than my more detailed CE models. In this simplified approach, only the contribution of O sites to the denominator of Eq. (5.6) is considered, since the binding energies in T sites are usually at least 0.1 eV higher than in O sites and the contribution of T sites can therefore be neglected. Additionally, zero point energies in all O sites and transition states are assumed to be constants. My approach to finding a simplified model for the O site binding energies is illustrated in Fig. 5.11. In this figure, O sites whose NN shell are made up of x Pd atoms, y Cu atoms, and z Ag atoms are denoted $Pd_xCu_yAg_z$. The symbols shown in Fig. 5.11 show averages of DFT calculated O site binding energies for each kind of site as a function of the lattice parameter of the alloy. For each class of binding site, the binding energies decrease approximately linearly as the lattice parameter is increased. As expected, increasing the number of Ag atom in the NN shell increases the binding energies, while this effect is less significant for Cu atoms.

The energy of H atoms in the transition states between adjacent O and T sites also decreases with the lattice constant, as shown in Fig. 5.12. To classify the available TS in a simplified description, I used the local environment of the NN shell of the T site rather

than the O site to distinguish different transition states. There are fmy metal atoms in the NN shell of each T site, three of which form a "window" that connects to an O site and defines a TS. I classified transition states by considering the three metal atoms forming the window separately from the fourth metal atom making up the T site. For example, a TS denoted Pd_2Ag-Ag has a window formed by two Pd atoms and one Ag atom, with the fourth metal atom defining the T site being Ag. The results in Fig. 5.12 indicate that the presence of Ag atoms in the window forming a TS increases the energy of the TS significantly, while the effect of substituting Cu for Pd is almost negligible.

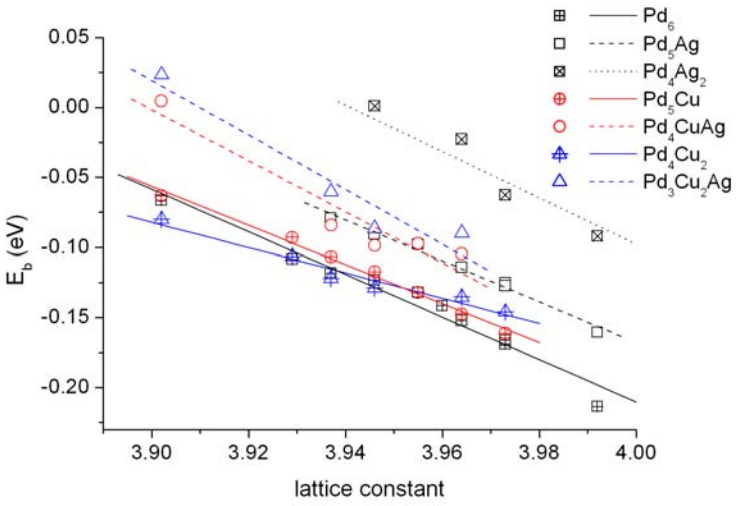

Figure 5.11: The average classical binding energies in O sites in PdCuAg alloys as a function of the alloy lattice constant. Symbols show averages of DFT data for the classes of O sites indicated in the legend, while lines show the fitted binding energies defined in Eq. (5.8).

In my simplified model, the binding energy in each class of O site (TS) was fitted to the available DFT data using

$$E_b(E_{TS}) = E_0 + c \cdot (LC - 3.96) \qquad (5.8)$$

Here E_b (E_{TS}) is the binding energy in the O site (transition state), LC is the lattice constant in Å, while E_0 and c are parameters fitted from the DFT data. The fitted parameters in Eq. (5.8) for O sites (transition states) are listed in Table. 5.2.

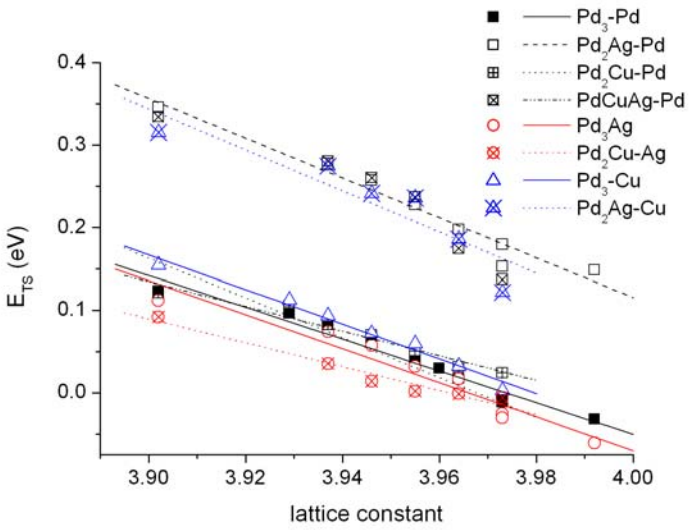

Figure 5.12: The average classical binding energies in transition state in PdCuAg alloys as a function of the alloy lattice constant. Symbols show averages of DFT data for the classes of O sites indicated in the legend, while lines show the fitted binding energies defined in Eq. (5.8).

Table 5.2: The fitted parameters in Eq. (5.8) for different O sites and transition states (TS), with all units in eV.

O site	E_0	c	TS	E_0	c
Pd_6	-0.141	-2.22	Pd_3-Pd	0.027	-1.92
Pd_5Ag	-0.106	-1.69	Pd_2Ag-Pd	0.212	-2.42
Pd_4Ag_2	-0.032	-1.67	Pd_2Cu-Pd	0.045	-1.49
Pd_5Cu	-0.140	-1.39	PdCuAg-Pd	0.200	-2.69
Pd_4CuAg	-0.111	-1.92	Pd_3-Ag	0.012	-2.06
Pd_4Cu_2	-0.136	-1.10	Pd_2Cu-Ag	0.003	-1.45
Pd_3Cu_2Ag	-0.098	-2.15	Pd_3-Cu	0.041	-2.10
			Pd_2Ag-Cu	0.195	-2.28

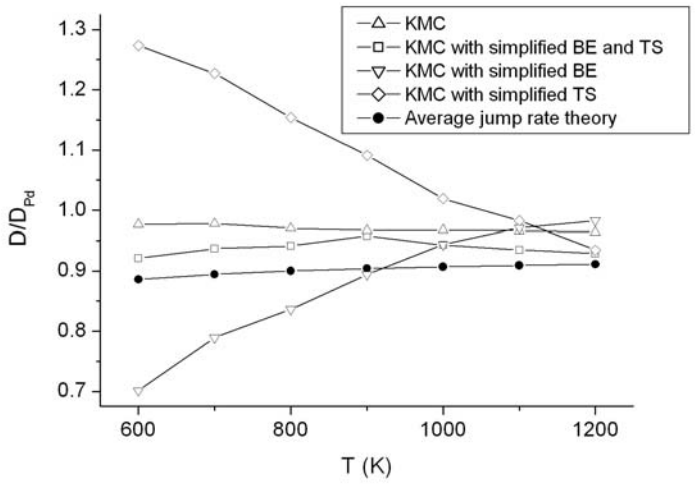

Figure 5.13: The normalized diffusivity of hydrogen in $Pd_{96.3}Ag_{3.7}$ using average jump rate theory or KMC simulations with different assumptions for the binding energies (BE) at the interstitial site and energies at the transition states (TS).

The AJRT in the form described above invokes two main assumptions. First, I used the simplified description defined in Eq. (5.8) for the energies of the O sites and transition states instead of the more detailed CE expansion I developed earlier. Second, the AJRT assumes that the probability distributions of the O site binding energies and the TS energies are independent. This second assumption cannot be exactly true; there is clearly a considerable spatial correlation between the atoms that define the energy of an O site and the atoms that define the energies of the transition states that control jumps out of the same O site. I tested the validity and importance of these assumptions separately by comparing results from the AJRT with KMC simulations for $Pd_{96.3}Ag_{3.7}$.

I first consider the validity of the simplified models for the site energies. Figure 5.13 shows KMC results from fmy independent simulations for $Pd_{96.3}Ag_{3.7}$, one using the full CE-based description of site energies, one using the simplified description above for both O sites and TS, and two in which the simplified description was used for either O sites or TS but not both. In all of these KMC calculations, the full CE-based model was used for T sites. It is clear from the figure that mixing the CE models and simplified models for the O sites and TS gives poor results, but applying the simplified model to both O sites and TS gives diffusivities that lie within 10% of the full CE result, which should be viewed in this discussion as the correct result. In other words, the simplified model I developed above appears to capture the main features of H diffusion, at least in the binary Pd-Ag alloy for which I performed these KMC simulations.

To examine the assumption made in the AJRT about the statistical independence of the energy distributions of the O sites and TS, I can compare the predictions of the AJRT with KMC simulations that use the same simplified model for the binding energies,

shown in Fig. 5.13. The AJRT results give diffusivities that are ~5% smaller than the KMC calculations for the PdAg binary alloy examined in this figure. This observation suggests that the correlations that are ignored by the AJRT have a relatively small influence on the overall diffusivity of H. This implies that the AJRT can be used to examine the diffusivity of H in alloys for which a model of the O site and TS binding energies is available in a way that avoids the necessity of performing KMC simulations.

A comparison between the predictions of the AJRT using the simplified binding energies defined above and KMC results with the full CE-based description of site energies for PdCuAg alloys is shown in Figure 5.14. Although the AJRT does not give quantitatively accurate results for the reasons discussed above, it captures the main trends shown previously in Fig. 5.10 and provides a useful framework to understand these results. The diffusivity of H in the alloys decreases as Ag concentration is increased. The analysis that led to my implementation of the AJRT highlights two main effects that exist when Ag is added to the alloy. First, the change in O site binding energy as a function of Ag content is more marked than the equivalent change in the TS energies. As a result, the activation energy for H atoms to hop out of O sites tends to increase as Ag content is increased. For example, when the lattice constant changes from 3.960 Å (pure Pd) to 3.992 Å ($Pd_{81.5}Ag_{18.5}$), the binding energy in Pd_6 site decrease by 0.072 eV, while the energy in Pd_3-Pd transition state decrease by 0.060 eV. The activation energy barrier, the difference between the binding energy in the O site and the energy in the transition state, slightly increases by 0.012 eV. Secondly, Figure 5.12 reveals that hopping through a triangle of atoms consisting of one or more Ag atoms is much less favorable than hopping through other kinds of transition states. This local effect means that large

activation energy barriers exist for H hopping in the immediate vicinity of Ag atoms. The combination of these two effects means that throughout the PdCuAg phase diagram, adding Ag to the alloy tends to reduce the net diffusivity of H.

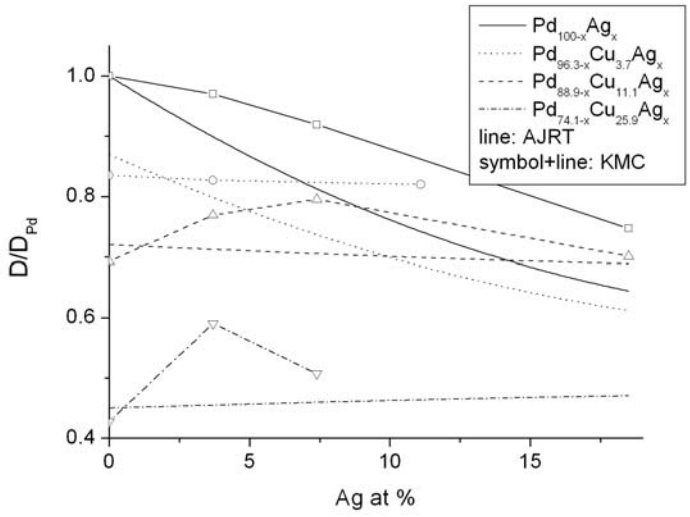

Figure 5.14: The diffusivity of hydrogen in PdCuAg alloys at 800 K from average jump rate theory and from KMC simulations, normalized by the value in pure Pd.

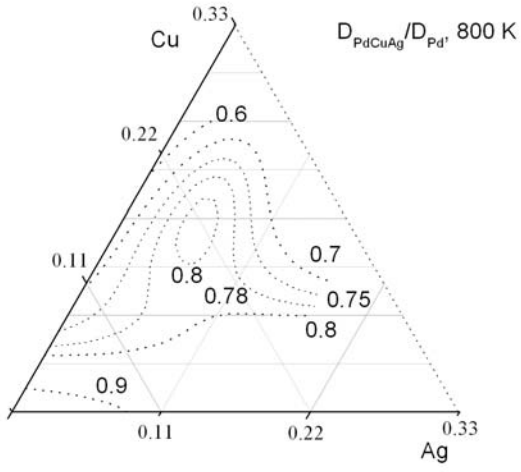

Figure 5.15: Contour map of the diffusivity of hydrogen in PdCuAg alloys normalized by the value in pure Pd at 800 K.

In Fig. 5.15, I plot a contour map of H diffusivity at 800 K, interpolated from my calculated data. The interpolation process has been described in the previous section. In this contour map, pure Pd has the highest diffusivity; all PdCuAg alloys have a lower diffusivity than pure Pd. The lowest diffusivity in this map is still about 60 % of the value in pure Pd, which indicates that the diffusivity is unlikely to be a dominant factor in determining the permeabilities for these alloys.

5.4.5 Permeabilities of hydrogen in PdCuAg alloys

In the previous two sections, I have calculated the solubilities and diffusivities in PdCuAg ternary alloys, as well as in PdCu and PdAg binary alloys. In this section, I will discuss the impact of adding Ag on the permeabilities of hydrogen in the alloys, which is a product of the solubilities and diffusivities. In Fig. 5.16, I show the calculated permeability for each alloy at different temperatures, normalized by the value in Pd. The normalized permeabilities at 800 K are shown in Fig. 5.17. Figure 5.16 and Fig. 5.17 show that the net permeability of H increases with Ag concentration for alloys with the same amount of Cu. Similar to the solubility, the strength of this trend is diminished at high Cu or Ag content. In Fig. 5.18, I showed the calculated contour map of the permeability at three different temperatures, 600, 800 and 1200 K. The shape of the contour map of the permeability is closer to the map of the solubility than to the diffusivity, which indicates that for the permeability the increased solubility with Ag concentration is more dominant than the diffusivity.

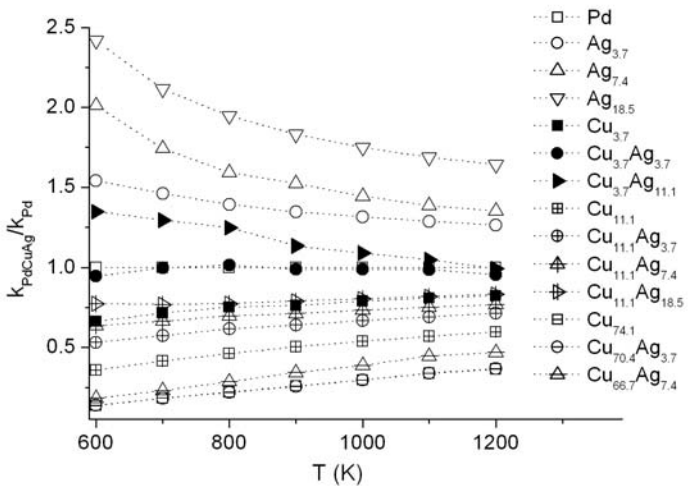

Figure 5.16: Predicted permeabilities of hydrogen in PdCuAg alloys, normalized by the permeabilities in pure Pd. For simplification only the concentration of Cu and Ag are listed in the label.

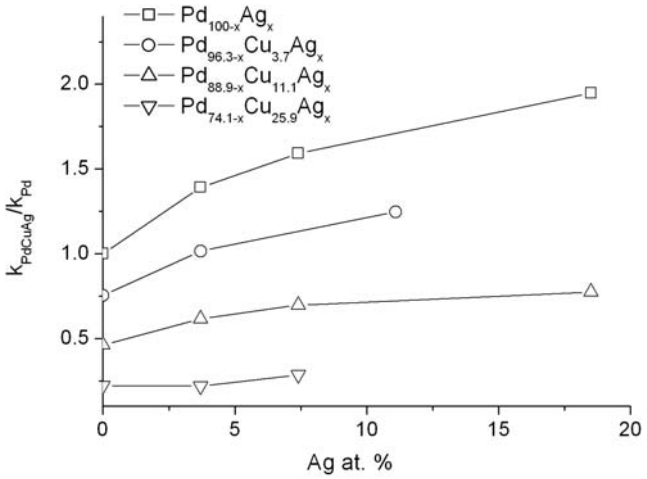

Figure 5.17: Predicted permeabilities of hydrogen in PdCuAg alloys at 800 K, normalized by the permeabilities in pure Pd.

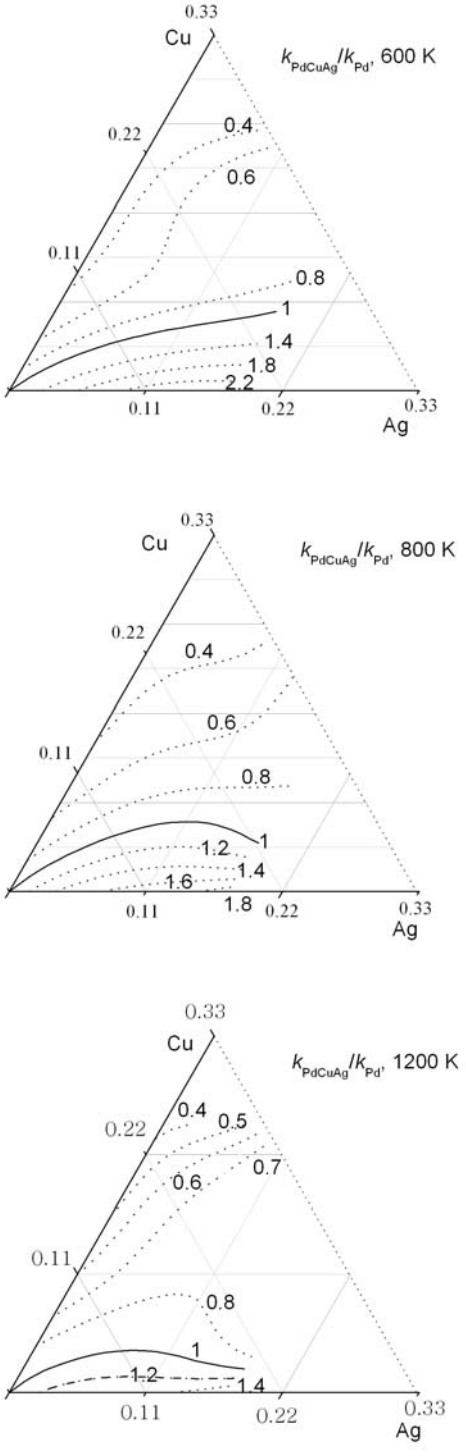

Figure 5.18: Contour map of the permeability of hydrogen in PdCuAg alloys normalized by the value in pure Pd at 600 K (top), 800 K (middle) and 1200 K (bottom).

In Fig. 5.19, I focus on the contour where the permeability of PdCuAg is equal to pure Pd. All compositions located below this contour at each temperature in the ternary phase diagram have higher permeability than pure Pd. When the temperature increases from 600 K to 1200 K, this contour slightly moves higher Ag concentrations, which indicates for alloys with the same Cu content, more Ag is required at higher temperature to maintain the same permeability.

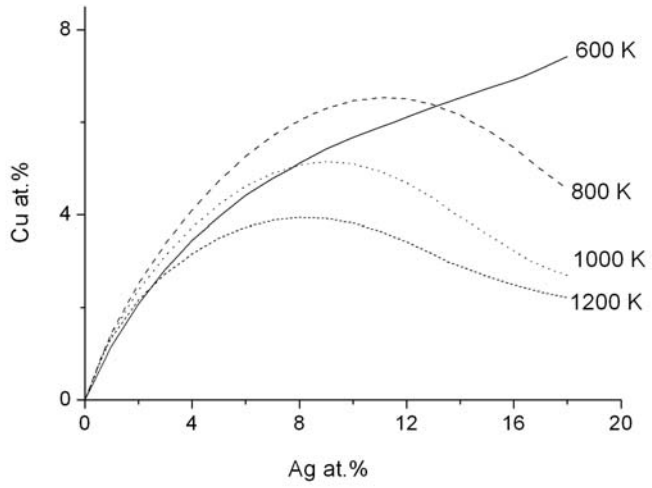

Figure 5.19: Alloys with equal permeability in pure Pd at different temperatures. For simplification I only plot the concentration of Cu and Ag in this graph. The Pd concentration can be calculated as Pd %=100- Cu%-Ag%.

5.5 Conclusions

In this chapter, I have screened a series of PdCuAg alloys as H_2 purification membranes. The solubilities of hydrogen are observed to increase with Ag concentration while the diffusivities decrease in most cases. The net permeability, a product of the solubility and the diffusivity, increases if Ag is substituted for Pd, which indicates that for

these alloys, solubility is more dominant contributor to the permeability than the diffusivity. In the contour map of the permeabilities, I have located compositions which have a higher permeability than pure Pd. These alloys are of particular interest as they might be a good candidate as H_2 purification membranes, which require both high permeability and high contaminant resistance.

This is the first time that H permeability has been examined for a board range of ternary compositions. The contour maps of the H solubility, diffusivity and permeability have been plotted for ternary alloys. Although my research only examined PdCuAg ternary alloys, the same method can also be used for other ternary alloys. [8] Theoretical predictions for H permeability in ternary alloys can, thus, provide a useful way in searching new materials with good properties for H_2 purification.

5.6 Reference

[1]S. N. Paglieri, J. D. Way Sep. Purif. Methods 31 1 (2002)

[2]P. Kamakoti, B. D. Morreale, M. V. Ciocco, B. H. Howard, R. P. Killmeyer, A. V. Cugini, D. S. Sholl Science 307 569 (2005)

[3]P. Kamakoti, D. S. Sholl J. Membr. Sci. 225 145 (2003)

[4]G. L. Holleck J. Phys. Chem. 74 503 (1970)

[5]P. Kamakoti, D. S. Sholl Phys. Rev. B 71 014301 (2005)

[6]C. G. Sonwane, J. Wilcox, Y. H. Ma J. Chem. Phys. 125 184714 (2006)

[7]C. G. Sonwane, J. Wilcox, Y. H. Ma J. Phys. Chem. B 110 24549 (2006)

[8]L. Semidey-Flecha, D. S. Sholl J. Chem. Phys. 128 144701 (2008)

[9]G. Henkelman, B. P. Uberuaga, H. Jonsson J. Chem. Phys. 113 9901 (2000)

[10]Y. Sakamoto, S. Hirata, H. Nishikawa J. Less-Common Metals 88 387 (1982)

[11]L. M. Cameron, C. A. Sholl J. Phys.: Condens. Matter 11 4491 (1999)

Chapter VI Evaluation of carbon diffusion in Pd and Pd-based alloys

Pd-based alloys are a well-established material as membranes for separating and purifying hydrogen from mixed gas streams and as a catalyst for hydrogenation reactions. One target application for the integration of membrane technologies has been the treatment of syngas streams from gasification processes. The gasification effluent stream typically contains hydrogen mixed with impurities like carbon dioxide, carbon monoxide, steam, and trace amounts of hydrogen sulfide and ammonia. In Chapter IV, I discussed how hydrogen sulfide affects the performance of metal membranes and used first-principles calculations to evaluate the permeability of hydrogen in nine metal sulfides. In this chapter, I will discuss another impact of these impurities, namely the diffusion of carbon in Pd and Pd based alloys.

6.1 Introduction

Diffusion of carbon in iron group transition metals is important in a number of technologically important processes such as surface hardening and molecule-surface interactions in heterogeneous catalysis.[1, 2] For example, due to its relatively high diffusivity, interstitial diffusion of carbon often controls the kinetics of phase transformations and microstructure in steels. The diffusion of carbon in ferrite and austenite has been thoroughly investigated experimentally for over 50 years.[3] However, a description of the atomic details of the diffusion path of carbon in ferrite and austenite from first principle calculations was only given relatively recently. [4]

When Pd-based alloys are used in the treatment of syngas streams from gasification processes, trace amount of impurities like carbon dioxide, carbon monoxide,

steam, and trace amounts of hydrogen sulfide and ammonia are introduced on the feed side of the membrane as well as hydrogen. [5, 6] It is clear from both experiments and theoretical calculations that under the conditions where metal membranes would be used, carbon-containing species such as CH_4 and CO can adsorb and react on the metal surface.[7, 8] Recent experiments revealed that after a long time of operation a carbon layer could be observed on the permeate side of the membrane, which indicated that the diffusion of carbon in Pd based alloys shouldn't be neglected. Besides that, both surface adsorbed carbon and subsurface carbon were demonstrated to be an important role in heterogeneous catalytic processes. Recent experiments revealed that the population of subsurface sites of palladium by either hydrogen or carbon governs the Pd catalyzed alkyne hydrogenation events on the surface. [1, 2] Based on these observations, the potential role of dissolved carbon in these applications means that a quantitative understanding of the dissolution and diffusion of carbon in Pd and Pd based alloys would be useful.

The diffusion of carbon in Pd was only studied experimentally by Yokoyama et al.,[9] who observed a diffusion activation energy of 1.35 eV for this process. The diffusivity measured for carbon in these experiments was about seven orders of magnitude lower than the diffusivity of hydrogen in Pd at 1223 K.[9] I am not aware of any previous studies that have quantified the diffusion rates of carbon in Pd-based alloys.

Based on my previous success on using first-principles calculations to explore the diffusivity and solubility of hydrogen in Pd based alloys, in this chapter, I studied a first principles study of the dissolution and diffusion characteristics of carbon in pure Pd and in PdAg, PdAu, and PdCu alloys. I first studied the diffusivity of carbon in pure Pd at

different temperatures and compared it with Yokoyama's reports, then turned to understanding how the alloy components changed the diffusion process. Finally, I considered the diffusion in a commercially used alloy, $Pd_{77.7}Ag_{22.3}$.

6.2 Method

In this study, DFT calculations were performed using the Vienna *ab initio* Simulation Package (VASP) using the generalized gradient approximation (GGA) with the PW91 functional to describe electron exchange-correlation effects. Ion–electron interactions were described by ultrasoft pseudopotentials. A plane-wave expansion with a cutoff of 300.0 eV is used in all calculations.[10] Geometry relaxations were performed with a conjugate gradient method until the forces on all unconstrained atoms were less than 0.03 eV/Å. A Monkhorst–Pack mesh with 4×4×4 *k*-points was used for all calculations.

I studied carbon binding in pure Pd and in selected PdCu, PdAu and PdAg alloys. Pure Pd has an fcc crystal structure, and the alloys I considered were assumed to have a substitutionally random fcc structure. This structure is consistent with the experimentally established binary phase diagrams for each alloy I considered.[11] DFT optimization gave a lattice constant of 3.960 Å for pure Pd without any interstitial carbon atoms. In all calculations the volume of the lattice was kept constant and all atoms were free to move during the calculation, as appropriate for examining an interstitial species with a low concentration. In a supercell containing 27 Pd atoms, an interstitial carbon in an octahedral site only slight expanded the interstitial site by moving the Pd atoms in the nearest neighbor shell 0.048 Å. This number decreased to 0.018 and 0.001 Å for Pd

atoms in the next nearest and third nearest shell, respectively. This small expansion indicated that keeping the volume of the supercell constant is acceptable in my calculations. Performing a series of calculations with supercells containing 4, 16, 27, 32 and 64 Pd atoms, I found that when the supercell size was increased beyond 27 Pd atoms, the binding energy of carbon changed by less than 0.02 eV relative to the result from the supercell with 27 Pd atoms. As a result, all my subsequent calculations for bulk materials were performed using a supercell containing 27 metal atoms.

Transition states for diffusion of carbon were determined using the Nudged Elastic Band (NEB) method.[12] The vibrational frequencies of local minima and transition states were calculated in the harmonic approximation by assuming that localized vibrations of carbon atoms are decoupled from vibrations of the metal atoms. This procedure gives three real frequencies at a local energy minimum and two real frequencies and one imaginary frequency at a transition state.

6.3 Adsorption and diffusion of carbon in pure Pd

6.3.1 Adsorption and diffusion of carbon in pure Pd at 0 K

Previous reports indicate that light elements including H, N, C, and O typically occupy the interstitial site rather than substitute the lattice atoms of metals.[4, 13] To test whether this is also the case for C in Pd, I calculated the binding energies of interstitial and substitutional C. The binding energy of interstitial carbon was calculated as

$$E_b = E_{MC} - E_M - E_C \qquad (6.1)$$

Here, E_b, E_{MC}, E_M and E_C are the binding energy, the total energy of the metal in the presence of interstitial carbon, the total energy of the pure metal, and the reference

carbon energy, respectively. The reference state of carbon is chosen to be gaseous CH_4, one potential source of carbon in the process of purifying hydrogen. With this choice, E_C is defined by

$$E_C = E_{CH_4} - 2E_{H_2} \qquad (6.2)$$

Here, E_{CH_4} and E_{H_2} are the zero point energy corrected total energies of gaseous CH_4 and H_2, correspondingly. Zero point energies were calculated within the harmonic approximation.

Two kinds of interstitial sites exist in the fcc lattice of pure Pd, the octahedral site (O site) and the tetrahedral site (T site). Figure 6.1 shows the calculated binding energies for possible configurations of interstitial carbon in pure Pd with the DFT-optimized lattice constant of 3.960 Å. The binding energy of interstitial carbon in the O site is 2.03 eV, which indicates the interstitial carbon configuration is unfavorable compared to gaseous CH_4. Interstitial C in the O site, however, is more stable than the interstitial species in the T site by ~0.8 eV.

I also estimated the substitutional energy of a C atom by calculating

$$E_s = E_{M_{n-1}C} - \frac{n-1}{n} E_M - E_C \qquad (6.3)$$

Here, n is the number of Pd atoms in the defect-free supercell, which is 27 in my calculations, and $E_{M_{n-1}C}$ is the total energy of a supercell with n-1 metal atoms and a single substitutional carbon atom. I found the substitutional energy to be 6.2 eV, which is much higher than the interstitial configurations. This indicates that the configuration is highly unfavorable. As a result, I only consider interstitial carbon in my following calculations.

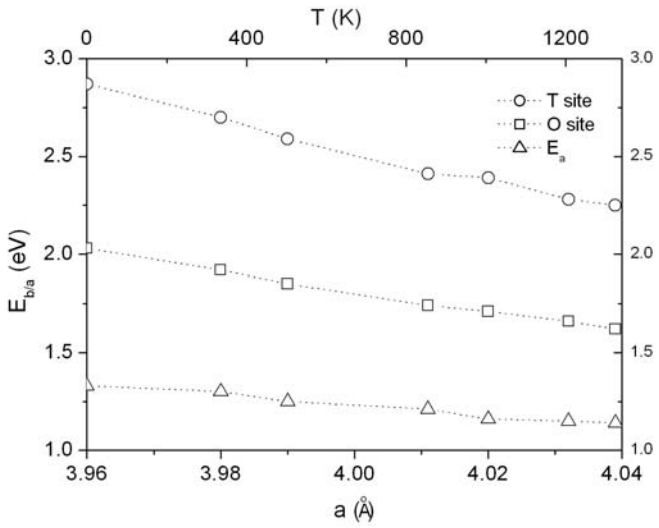

Figure 6.1: The binding energies and diffusion barriers of interstitial carbon in pure Pd as a function of lattice constants or temperature calculated as described in the text.

I now turn to describing the diffusion of interstitial C in Pd. Because the O site is the most stable location for interstitial C, I considered processes that allowed C to hop from an O site to another nearest neighbor O site. Two possible hopping paths were chosen in NEB calculations. The first one starts from an O site, passes through a T site and ends at another O site,[14, 15] while the second one connects two O sites directly.[4, 16] The former path is typically expected to be the dominant diffusion path in fcc metals, but the latter path has been reported for C diffusion in austenite at low concentration,[4] and O hopping in Ni.[16] I found, however, that C cannot diffuse in Pd via the latter path at any appreciable rate. That is, the only physically relevant hopping path starts in an O site and passes through a T site before ending at another O site. The converged minimum energy path for this process is symmetric, with a double maxima and one intermediate local minimum at the T site. The energy barrier between the O site and the transition state

is 1.33 eV using the DFT-optimized lattice constant. Hopping from a T site to an O site proceeds with a barrier of 0.49 eV, so this is a much faster process than O to T hopping.

6.3.2 Interaction between interstitial carbon and vacancies

Metal vacancies have been found to play an important role in absorption of C in metastable Fe-C alloys.[17] Since the presence of H is known in some circumstances to increase the vacancy concentration in Pd,[18] I examined the interaction between C and vacancy defects in Pd. Specifically, I calculated the binding energies of carbon with a Pd vacancy in the nearest neighbor shell of the interstitial sites. The interaction energy between interstitial C and a Pd vacancy, E_I, was defined by

$$E_I = E_{VC} - \frac{n-1}{n} E_M - E_b - E_C \qquad (6.4)$$

where E_{VC} is the total energy of the supercell containing the interstitial carbon-vacancy cluster. With this definition, a positive interaction energy is found when an interstitial-vacancy pair is favored compared to having both defects isolated in the crystal. The calculated interaction energy was 0.13 eV for the O site and 0.11 eV for the T site. Although interstitial C is slightly stabilized by these vacancies, the large formation energy for Pd vacancies suggests that interstitial-vacancy complexes will play a relatively minor role in the absorption of C in Pd, unlike the situation in Fe-C systems.[17]

Table 6.1: Hopping barriers of carbon from an O site to a T site in pure Pd with the existence of Pd vacancy. Here No means no vacancy exist in the calculation. NN and NNN means one vacancy exists in the nearest (next nearest) neighbor shell of the interstitial site. The activation energy barrier (E_a) is estimated to be the difference of the site energy between O site and transition state.

O site configuration	T site configuration	number of vacancies	E_a
No	No	0	1.33
NN	NN	1	1.25
NN	NNN	1	1.27
NNN	NN	1	1.28
NN,NNN	NN,NNN	2	1.21
NN,NNN	NN	2	1.23

To study how vacancies affect diffusion of carbon, several possible configurations of O to T hops in the vicinity of a vacancy or vacancies were examined using NEB calculations. The results of these calculations were listed in Table 6.1. After NEB calculations, the hopping barriers from O site to T site were examined. These calculations showed that the O-T hopping barrier slightly for sites near Pd vacancies in my calculation. In the vicinity of one Pd vacancy, the lowest barrier was found to be the hopping with a Pd vacancy in the nearest neighbor (NN) shell of the interstitial carbon for both initial O site and final T site, followed by the hop with a Pd vacancy in the nearest and next nearest neighbor shell of the interstitial carbon for the initial state and the final state,

respectively. For the hopping in the vicinity of two nearby vacancies, the lowest barrier is only 0.12 eV lower than the hopping in a perfect lattice. Because the population of Pd vacancy is typically small, these observations further support the idea that Pd vacancies do not play an important role in the absorption and diffusion of carbon in Pd. I did not consider the contribution of metal vacancies in the remainder of my calculations.

6.3.3 The effect of thermal expansion of Pd lattice

All of the results described above were based on calculations performed with the DFT-optimized lattice parameter for Pd, 3.960 Å. For interstitial species that are mainly relevant at high temperatures, it is useful to consider whether the characteristics of interstitial diffusion are affected by thermal expansion of the metal.[14, 16] Figure 6.1 shows the DFT-calculated binding energies and diffusion activation energies of C in Pd for several different lattice constants in the range 3.96-4.02 Å. Each quantity listed in the table decreases approximately linearly with the lattice constant over this range. As the lattice constant changes from 3.96 Å to 4.04 Å, the O site binding energy decreases by 0.41 eV, while the activation energy to hop out of an O site decreases by 0.19 eV.

To connect the data above with the effects of thermal expansion on C diffusion in Pd, I must define the temperature-dependent lattice constant of Pd. Two equations describing the experimentally observed lattice thermal expansion of Pd have been reported. The first one was given by Dutta et. al, [19]where the lattice constant (in m) is given as

$$a_T = 3.889\times10^{-10} + 4.5\times10^{-15}T + 1.37\times10^{-18}T^2 \qquad (6.5)$$

The second equation was reported by Lu et al.[20] who characterized the molar volume of Pd as

$$V_T = V_0 \, e^{3.11002\times10^{-5} T + 7.4407\times10^{-9} T^2} \qquad (6.6)$$

Here, V_T (V_0) is the molar volume at temperature T (0 K). These two equations define lattice constants that differ by less than 0.15 Å for T < 1400 K. I cannot use these lattice constants directly in interpreting my DFT calculations because of the small difference that exists between the DFT-optimized lattice constant at 0 K and the experimental observation. I therefore predicted the relevant lattice constant to use in applying my DFT data by multiplying that the ratio a_T/a_0 measured in experiments with the DFT-optimized lattice constant. At each temperature, I used the average of Eq. (6.5) and Eq. (6.6) as the experimental value. Using the above assumptions, I show how the binding energies and activation energy barriers for C diffusion in Pd change with temperature in Figure 6.1. Changing the temperature from 0 K to 1000 K is seen to reduce the binding energy of C in an O site by ~0.25 eV and the diffusion activation energy by ~0.1 eV.

6. 4 Adsorption and diffusion of carbon in Pd-based alloys

One key application of Pd based membranes is to purify hydrogen from gas mixtures. Because pure Pd membranes are prone to hydrogen embrittlement and poisoning by S-containing species, Pd-based alloys are useful materials for these applications.[21] PdAg alloys have been widely considered because they can show an improved permeability of hydrogen compared with pure Pd.[22, 23] PdCu alloys have been reported to be more resistant to sulfur poisoning than pure Pd.[24] I know of no previous studies that have quantified the solubility or diffusivity of C in Pd-based alloys

such as these. To provide some initial information on this topic, I extended my calculations to examine interstitial C in $Pd_{96}M_4$ alloys with M = Ag, Cu and Au to see how a low concentration of the non-Pd metal affects interstitial C. I then turned to a more complicated alloy, $Pd_{77.7}Ag_{22.3}$, to show how carbon behaves in an alloy that is already used in the practical applications.[3] In every case, I have defined the alloy composition in at.%. All of these alloys are known to be substitutionally random fcc crystals at elevated temperatures.[11] For each alloy, all calculations were performed using a 27 atom supercell with a DFT-optimized lattice constant. The lattice constant for each alloy is listed in Table 1. Compared to pure Pd, the presence of Cu decreases the alloy lattice constant while Ag or Au increases the lattice constant.

6.4.1 Adsorption and diffusion of carbon in $Pd_{96}M_4$

Similar to what I did for pure Pd, I calculated the binding energies of interstitial C in both O and T sites. In substitutionally random $Pd_{96}M_4$ alloys, more than 99% of O sites can be divided into three categories if the sites are characterized simply by the atoms forming the nearest neighbor (NN) and next nearest neighbor (NNN) shell of atoms around the site.[15] These sites have one M atom in the NN shell but pure Pd in the NNN shell (denoted NN-O), one M atom in the NNN shell but no M atoms in the NN shell (denoted NNN-O), or no M atoms in the NN or NNN shells (denoted NO-O). I similarly defined NN-T, NNN-T and NO-T sites. In Table 6.2, I listed the binding energies for each type of interstitial sites in different alloys. In each alloy, the NN-O site has the least favored binding energy among the O sites I examined, indicating that interstitial C will not typically be found in these sites. In $Pd_{96}Ag_4$ and $Pd_{96}Cu_4$, the NNN-O site has the

lowest binding energies, while in $Pd_{96}Au_4$ the NO-O and NNN-O site have very similar binding energies. Similar to the effect caused by the thermal expansion of pure Pd, the binding energies at NO-O sites become more favorable as the lattice constant of the alloy is increased. For T sites, I found that including an M atom in the NN or NNN shell increases the binding energy by about 0.3 eV. The NO-T sites are the most stable T site in all three alloys

Table 6.2: The binding energies and diffusion barriers for O to T hops of interstitial carbon in $Pd_{96}Cu_4$, $Pd_{96}Au_4$, $Pd_{96}Ag_4$ and $Pd_{77.7}Ag_{22.3}$.

composition	$Pd_{96}Cu_4$	$Pd_{96}Au_4$	$Pd_{96}Ag_4$	$Pd_{77.7}Ag_{22.3}$
lattice constant (Å)	3.953	3.968	3.970	4.011
E_b (eV)	NO-O 2.12	NO-O 1.97	NO-O 1.92	O 1.70-3.03
	NNN-O 2.08	NNN-O 1.98	NNN-O 1.93	
	NN-O 2.21	NN-O 2.29	NN-O 2.18	
	NO-T 2.97	NO-T 2.79	NO-T 2.80	T 2.42-4.05
E_a (eV)	1.36	1.31	1.30	1.20-1.25

To study the diffusivity of carbon in $Pd_{96}M_4$ alloys, I chose the hop beginning with a NO-O site, passing through a NO-T site, and ending at a NO-O site, as these two O sites were the most stable configurations in each alloy. The activation energy barriers

from a NO-O site to the transition state in these three alloys are listed in Table 6.2. The barrier from a NO-T site to the transition state can be defined by the difference of the binding energies at NO-O site and NO-T site. Although this barrier decreases with the lattice constant, the decreasing trend is less significant than the binding energies. The difference between the highest barrier, in $Pd_{96}Cu4$, and the lowest barrier, in $Pd_{96}Ag_4$, is only 0.05 eV, while this value is 0.2 eV for the binding energies.

6.4.2 Adsorption and diffusion of carbon in $Pd_{77.7}Ag_{22.3}$

I now turn to $Pd_{77.7}Ag_{22.3}$. One key difference between $Pd_{77.7}Ag_{22.3}$ and $Pd_{96}M_4$ is that a much larger number of local configurations can exist for the interstitial sites in the former material than in the latter. Instead of attempting to describe every possible site in $Pd_{77.7}Ag_{22.3}$ with DFT, I examine the set of 27 O sites in a single computational supercell containing 21 Pd atoms and 6 Ag atoms that were randomly distributed on the lattice sites in the supercell. Previous studies of interstitial H in PdM alloys revealed that the binding energies of interstitial H are correlated with the number of Pd atoms in the nearest and next nearest shell.[25] I found a similar behavior for interstitial C in $Pd_{77.7}Ag_{22.3}$. Figure 6.2 shows the calculated O site binding energies as a function of the number of Pd atoms in the nearest shell. The scatter of the results in Fig. 6.2 shows that using the number of Ag atoms in the NN shell alone cannot fully describe the binding energies in this alloy, as expected.[15] Nevertheless, simply counting the number of Ag atoms in this shell captures much of the variation in the observed binding energies; O sites without any Ag atoms in the NN shell have the lowest binding energies and the binding energies increases by ~0.25 eV/Ag atom as the number of Ag atoms in the NN shell is increased.

This trend is consistent with my observation from $Pd_{96}Ag_4$ that interstitial C is more unfavorable in the NN sites than in the NO site. Although increasing the Ag content from $Pd_{96}Ag_4$ to $Pd_{77.7}Ag_{22.3}$ creates more sites that are unfavorable for interstitial C because of the presence of nearby Ag atoms, the binding energy of the most favorable sites in the Ag-rich alloy is significantly lower than in the Ag-poor alloy. The most favorable site I observed in the $Pd_{77.7}Ag_{22.3}$ alloy has a binding energy ~0.3 eV lower than the O sites in pure Pd, an effect that can be attributed to the expanded lattice constant of the alloy relative to pure Pd. The fact that a significant fraction of the O sites in the $Pd_{77.7}Ag_{22.3}$ alloy have lower binding energies for C than the O sites in pure Pd indicates that at equilibrium the concentration of interstitial C in the alloy will be higher than in the pure metal.

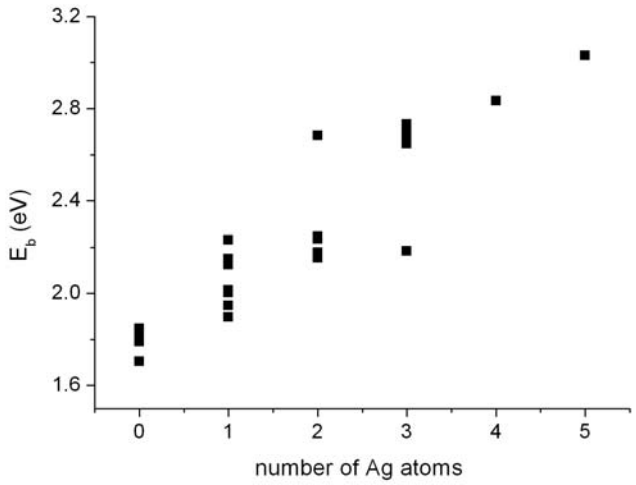

Figure 6.2: The binding energies of interstitial carbon in O sites of $Pd_{77.7}Ag_{22.3}$ as a function of the number of Ag atoms in the nearest neighbor shell.

To estimate how increasing the Ag content of the alloy changes the hopping of C between interstitial sites, I characterized the eight distinct hops that can occur from the O site with the lowest binding energy observed in $Pd_{77.7}Ag_{22.3}$. The calculated activation energies for this process, as shown in Table 6.2, were 1.20-1.25 eV lower than the value in pure Pd. I performed similar calculations for another O site in the alloy with one Ag atom in the NN shell whose binding energy is 0.31 eV higher than the lowest one. In this case both the initial configuration and the final configurations were different from the previous set of calculations. The hopping barriers, however, were found to be 1.22-1.28 eV. That is, all of the activation barriers for hopping out of these two distinct O sites were found to lie within a narrow range of energy.

6.5 Discussion

Above, I examined the absorption and diffusion of behavior of C in both pure Pd and Pd based alloys. In both pure Pd and Pd based alloys, increasing the lattice constant favors both the stability and hopping of interstitial carbon atoms. Further examination shows that despite the possible different environments outside of the nearest neighbor shell of the interstitial carbon atoms, I can use the same equations to describe the binding energies and the activation energy barriers of interstitial carbon in a NO-type site in both Pd and Pd based alloys, as shown in Figure 6.3. The equations are fitted to describe the linearly decreasing trend of the binding energies of the NO-type sites and hopping barriers in the unit of eV as shown below:

$$\begin{aligned} E_{b,O} &= -5.55a + 24.02 \\ E_{b,T} &= -8.75a + 37.53 \\ E_a &= -3.13a + 13.74 \end{aligned} \qquad (6.7)$$

Here $E_{b,o}, E_{b,T}$ and E_a is the binding energy at the O sites, T sites and the activation energy barrier, and a is the lattice constant of the metal.

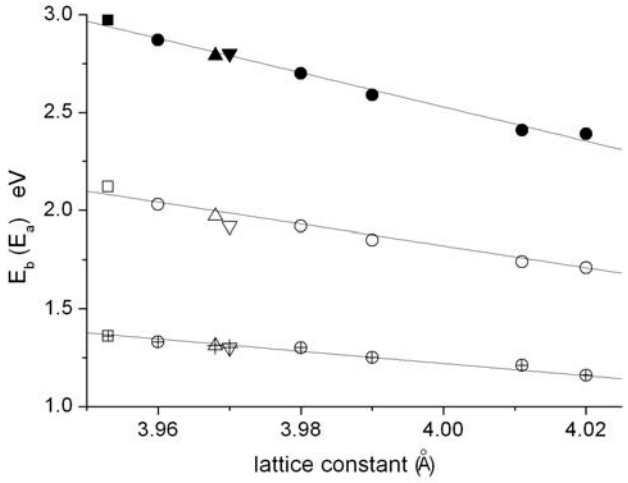

Figure 6.3: The binding energy and O to T activation energy as a function of the lattice constant in pure Pd and $Pd_{96}M_4$ alloys with M=Cu, Au and Ag. Solid symbols: T sites, Open symbols: O sites, symbols with crosses: activation energy. Circle: pure Pd, square: $Pd_{96}Cu_4$, upward pointing triangle: $Pd_{96}Au_4$, downward pointing triangle $Pd_{96}Ag_4$. Lines: fitting value from eq. 6. 6.

For $Pd_{77.7}Ag_{22.3}$, as I have discussed above, the binding energies in the interstitial sites depend strongly on the number of Ag atoms in the nearest neighbor shell, but the hopping barriers out of an O site, however, are roughly independent of the environment. These characteristics can be described using (in eV)

$$
\begin{aligned}
E_{b,O} &= 1.75 + 0.253 n_{Ag} \\
E_{b,T} &= 2.57 + 0.240 n_{Ag} \\
E_a &= 1.25
\end{aligned}
\tag{6.8}
$$

Here n_{Ag} is the number of Ag atoms in the nearest neighbor shell of the relevant interstitial site.

Once I have calculated the adsorption energy of interstitial carbon and activation barriers of the hopping in pure Pd, the diffusivity of the interstitial carbon can then be estimated by considering hopping between interstitial sites. The net diffusivity can be written as[26]

$$
D = n\beta d^2 / \bar{t} \tag{6.9}
$$

where n is the number of nearest neighbor sites for a diffusing interstitial atom, β = 0.25 is the probability that a jump from an O to a T site and a subsequent jump from the T site to an independently chosen O site advances the particle along a particular direction of diffusion, and d is the length of the jump projected onto the direction of diffusion, which is 0.5a in fcc metals where a is the lattice constant. t is the average time required for one hop, which is

$$
\bar{t} = \frac{1}{k_{O-T}} + \frac{1}{k_{T-O}} \tag{6.10}
$$

Here, k_{O-T} (k_{T-O}) is the hopping rate from O to T site (T to O site). I calculated the site to site hopping rates using the quantum corrected harmonic transition state theory as[25]

$$k_{O-T} = \frac{\prod_{i=1}^{3} v_o f(hv_i / 2kT)}{\prod_{j=1}^{2} v_j^{TS} f(hv_j^{TS} / 2kT)_i} e^{-E_{a,OT}/k_b T}$$
$$k_{T-O} = \frac{\prod_{i=1}^{3} v_T f(hv_i / 2kT)}{\prod_{j=1}^{2} v_j^{TS} f(hv_j^{TS} / 2kT)_i} e^{-E_{a,TO}/k_b T} \quad (6.11)$$

Here v_o, v_T and v_j^{TS} are the vibrational frequencies at the O site, T site and transition state, respectively, k_b and h are Boltzmann's constant and Planck's constant, $f(x) = \sinh(x)/x$ and $E_{a,OT}$ ($E_{a,TO}$) is the barrier for a hopping from O to T site (T to O site). As $E_{a,TO}$ is much lower than $E_{a,OT}$, $k_{T-O} \gg k_{O-T}$ and I can simplify Eq. (6.10) to

$$\bar{t} = \frac{1}{k_{O-T}} \quad (6.12)$$

Figure 6.4 shows the calculated diffusivity of carbon in pure Pd with and without the effects of thermal expansion on the lattice constant. When thermal expansion was included, the T-dependent lattice constant was estimated as described previously and the diffusion activation energies were defined using Eq. (6.7). To apply Eq. (6.11) in my calculations, I calculated the zero point energies (ZPE) of C in an O site, T site and transition state with different lattice constants. Unlike the binding energies, I found that the ZPE is almost independent of lattice constant. For example, when the lattice constant changes from 3.96 Å to 4.02 Å, the ZPE in the O site only decreases by 0.008 eV. Thus, I use the vibrational frequencies from Pd with the DFT-optimized lattice constant at all temperatures. The available experimental data is also shown in Fig. 6.4. The experimental data gives an activation energy of 1.37 eV at high temperature (1223-1378 K) and 1.32

eV at low temperature (300-640 K).[9] When I do not consider thermal expansion effects, I predict a net activation energy of 1.33 eV (1.35 eV) in the same high (low) temperature ranges and the diffusivity is ~4 (20) times lower than the high (low) temperature experimental values. After including thermal expansion effects, my calculations give a net activation energy of 1.25 eV (1.30 eV) in the high (low) temperature ranges. The diffusivity predicted with this approach is ~1.5 higher than the experimental value at high temperatures and ~8 times lower than the low temperature experimental values. When the small apparent inconsistency between the experimentally observed diffusivities is considered, I conclude that my first principles calculations accurately describe the diffusion of interstitial C in Pd.

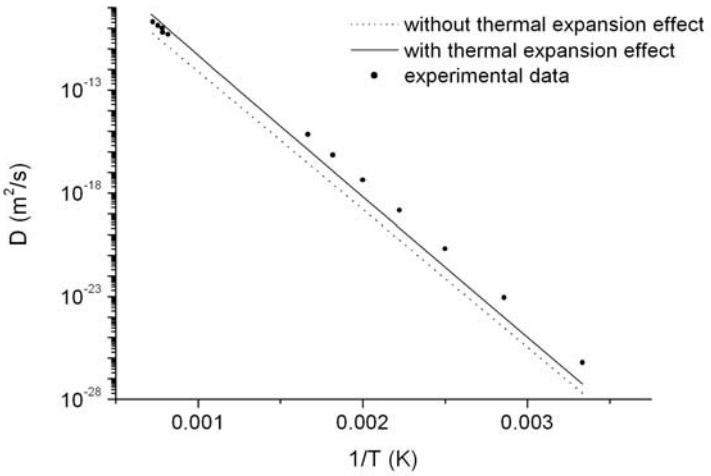

Figure 6.4: Predicted and experimentally observed diffusivity of C in pure Pd. The experimental measurements came from Yokoyama et al.'s report. [9] The calculated value showed both the result with and without considering thermal expansion of the lattice, as described in the text.

Due to the structure complexity of $Pd_{77.7}Ag_{22.3}$ alloys, an accurate calculation of the diffusivity of C in this material must consider all possible hopping paths in this alloy. Semidey-Flecha and Sholl have used methods based on cluster expansions to approach this task for H diffusion in metal alloys.[15] This approach is feasible when DFT data for a large collection of interstitial sites and transition states are available. Because I only generated DFT data for a limited number of transition states, I adopted a more approximate approach for estimating the diffusivity of C in $Pd_{77.7}Ag_{22.3}$. In these calculations, I generated a large substitutionally random simulation volume, then assigned the interstitial site and transition state binding energies using Eq. (6.8). I also assumed that the vibrational frequencies at different interstitial sites and transition states were independent of their the surrounding environment. The same Kinetic Monte Carlo methods used by Semidey-Flecha and Sholl[15] were then used to compute the diffusivity within this model. Figure 6.5 shows the diffusivity calculated in this way for $Pd_{77.7}Ag_{22.3}$ as well as the previous results for pure Pd that included thermal expansion effects. The results for the PdAg alloy did not include effects from thermal expansion. From 600 - 1200 K, the predicted diffusivity in $Pd_{77.7}Ag_{22.3}$ is 2-3 orders of magnitude lower than in pure Pd. It is interesting to note that for H diffusion in the same system, the diffusivity only decreases about 25% when the Ag content increases from 0 to 20%.[22] To explain this difference, I calculated the binding energies of H in PdAg alloys. These calculations show that adding a Ag atom in the nearest neighbor shell of an interstitial site only increases the binding energy by about 0.05 eV, while this value is 0.25 eV for carbon. This indicates, as might be expected, that the potential energy surface for

interstitial C is affected more strongly by the presence of Ag in the alloy than for interstitial H.

The effective activation energy barrier for C diffusion in $Pd_{77.7}Ag_{22.3}$ obtained from Fig. 6.5 is 1.47 eV. The difference between this value and the value for the local hops described in Table 2 is close to the energy change associated with adding one Ag atom in the nearest neighbor shell of an O site. This similarity is not a coincidence; it indicates that in the PdAg alloy, long-range diffusion of carbon must involve processes that move C from interstitial sites into neighboring interstitial sites that have an additional Ag atom in their NN shell. Even though the hopping barriers out of the distinct O sites I examined in Table 6.3 lay in a narrow range, the new barrier to hop from an O site into an adjacent T site and then onto a new O site will be dominated by the higher of the two intermediate barriers along this local path.

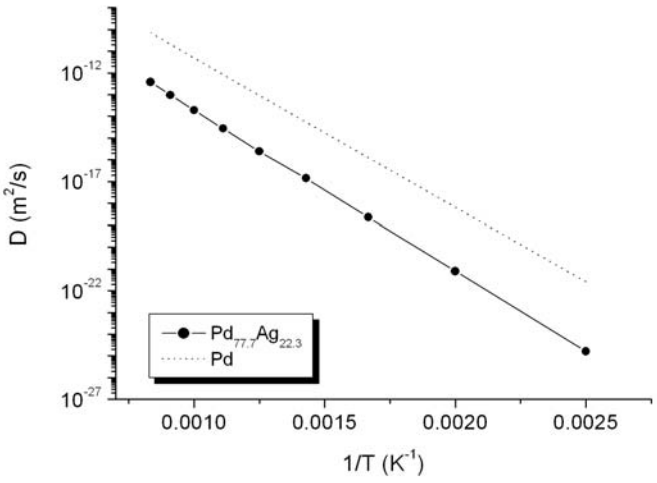

Figure 6.5: Predicted diffusivity of C in $Pd_{77.7}Ag_{22.3}$ and in pure Pd

6.6 Conclusion

In this chapter, I performed periodic DFT calculations of the absorption and diffusion of carbon in pure Pd and the Pd based alloys PdM with M=Cu, Ag and Au. In pure Pd, the most stable location for carbon is as an interstitial atom in an octahedral site. The binding energy in this site is endothermic by 2.03 eV compared with carbon in gaseous CH_4. Substitutional C is even less stable, and my calculations indicate that Pd vacancies will play at most a minor role in the population of interstitial C. The minimum energy path for carbon diffusion starts from an octahedral site, passes through an adjacent tetrahedral site and ends at another octahedral site. At low temperatures where thermal expansion of the metal can be neglected, my calculations have a diffusion barrier of 1.33 eV.

I found that in both Pd and Pd based alloys, the endothermic binding energy of C and the activation energy for interstitial diffusion decrease as the host's lattice parameter increases. Because the available experimental data for C diffusion in Pd is at elevated temperatures, it was important to include the effects of thermal lattice expansion when assessing the diffusivity of C in Pd. At temperatures above 1000 K, the diffusivity predicted via transition state theory is roughly an order of magnitude larger once thermal expansion effects are included than when the low temperature lattice constant for Pd was used. The diffusivity predicted by my calculations was in good agreement with the available experimental data.

In PdM alloys with low concentrations of M = Ag, Au, or Cu, the binding energy of interstitial C at sites with no M atoms in the nearest neighbor shell could be understood from the lattice expansion or contraction in the alloy relative to pure Pd. In each of these

alloys, the binding energy of interstitial carbon increases with the number of M atom in the nearest neighbor shell. Of the three alloys I considered, PdCu has the smallest lattice constant, thus it has the least favorable binding energies for interstitial C and the highest diffusion barriers. I also examine the properties of interstitial C in a more complex PdAg alloy, $Pd_{77.7}Ag_{22.3}$. By examining the binding energies and local activation energy for site to site hops in a range of sites in this alloy, I estimated the net diffusivity of C. My calculations predict that C diffusion in this alloy is 2-3 orders of magnitude slower than in pure Pd.

6.6 Reference

[1]D. Teschner, J. Borsodi, A. Wootsch, Z. Revay, M. Havecker, A. Knop-Gericke, S. D. Jackson, R. Schlogl Science 320 86 (2007)

[2]D. Teschner, E. Vass, M. Havecker, S. Zafeiratos, P. Schnorch, H. Sauer, A. Knop-Gericke, R. Schlogl, M. Chamam, A. Wootsch, A. S. Canning, J. J. Gamman, S. D. Jackson, J. MacGregor, L. F. Gladden J. Catal. 242 26 (2006)

[3]S. Uemiya, T. Matsuda, E. Kikuchi J. Membr. Sci. 56 315 (1991)

[4]D. E. Jiang, E. A. Carter Phys. Rev. B 67 214103 (2003)

[5]H. Gao, Y. S. Lin, Y. Li, B. Zhang Ind. Eng. Chem. Res. 43 6920 (2004)

[6]M. Mundschau, X. Xie Catal. Today 118 12 (2006)

[7]Y. Ma, J. Bansmann, T. Diemant, R. J. Behm Surf. Sci. 603 1046 (2009)

[8]K. M. Neyman, C. Innatam, A. B. Gordienko, I. V. Yudanov, N. Rosch J. Chem. Phys. 122 174705 (2005)

[9]H. Yokoyama, H. Numakura, M. Koiwa Acta. Mater. 46 2823 (1998)

[10]G. Kresse, J. Hafner Phys. Rev. B 48 13115 (1993)

[11]T. B. Massalski, H. Okamoto, P. R. Subramanian, L. Kacprzak *Binary alloy phase diagrams* (ASM International, Materials Park, Ohio, 1990), 3

[12]G. Henkelman, B. P. Uberuaga, H. Jonsson J. Chem. Phys. 113 9901 (2000)

[13]S. Q. Hao, M. Widom, D. S. Sholl J. Phys: Condens. Matter 21 115402 (2009)

[14]E. Wimmer, W. Wolf, J. Sticht, P. Saxe Phys. Rev. B 77 134305 (2008)

[15]L. Semidey-Flecha, D. S. Sholl J. Chem. Phys. 128 144701 (2008)

[16]E. H. Megchiche, M. Amarouche, C. Mijoule J. Phys: Condens. Matter 19 296201 (2007)

[17]C. J. Forst, J. Slycke, K. J. V. Vliet, S. Yip Phys. Rev. Lett. 96 175501 (2006)

[18]Y. Fukai, N. Okuma Phys. Rev. Lett. 73 1640 (1994)

[19]B. N. Dutta, B. Dayal Phys. Status Solidi B 3 2253 (2006)

[20]X. G. Lu, M. Selleby, B. Sundman Comp. Coupl. Phase. Diagr.Thermochem. 29 68 (2005)

[21]B. D. Morreale, B. H. Howard, O. Iyoha, B. M. Enick, C. Ling, D. S. Sholl Ind. Eng. Chem. Res. 46 6313 (2007)

[22]G. L. Holleck J. Phys. Chem. 74 503 (1970)

[23]C. G. Sonwane, J. Wilcox, Y. H. Ma J. Phys. Chem. B 110 24549 (2006)

[24]P. Kamakoti, B. D. Morreale, M. V. Ciocco, B. H. Howard, R. P. Killmeyer, A. V. Cugini, D. S. Sholl Science 307 569 (2005)

[25]P. Kamakoti, D. S. Sholl Phys. Rev. B 71 014301 (2005)

[26]C. Wert, C. Zener Phys. Rev. B 76 1169 (1949)

Chapter VII Conclusion

7.1 Conclusion

Metal membranes play a vital role in hydrogen purification. Defect-free membranes can exhibit, in principle, infinite selectivity for H_2. High performance metal membranes must be able to provide high fluxes, resistance to contaminants, long operational lifetime, and have low cost. Alloys offer a useful route to improve upon membranes based on pure metals. For example, using PdCu can increase the resistance of a membrane to H_2S relative to pure Pd.[1] Nevertheless, experimental development of new membranes is hindered by the large efforts required to make and test these materials.

In this work, I showed that a combination of first principles density functional theory (DFT) calculations and coarse grained lattice-gas modeling could be successfully used to predict the performance of Pd based alloys as H_2 purification membranes. I first performed atomic-scale DFT calculations to characterize the properties of interstitial, including binding energies, vibrational frequencies and activation barriers for hopping between interstitial sites. This information was then used in statistical mechanics models to predict the macroscopic properties of hydrogen in the metal alloys, including the solubility, diffusivity and permeability of hydrogen.

In this work, I first examined the resistance of surface processes in the permeation of H_2 through PdCu membranes. My results were found to be in qualitative and quantitative agreement with results for pure Pd using experimental inputs. For PdCu binary alloys, I found that adsorption from the gas phase and transitions between surface and bulk sites have negligible impact on the overall permeation rate. Permeation is dominated by bulk diffusion for thick membranes at temperatures higher than 600 K. For

membranes thinner than 1 μm, further reducing the thickness will not increase H flux when the temperature is lower than 500 K.

I then aimed to find materials with possible potential as H_2 purification membranes. Two different approaches were tested in my studies. First, I tested the possibility of using metal sulfides as H_2 purification membranes. Known metal membranes are poisoned by the formation of metal sulfides on the surface.[2] Identification of metal sulfides with high H permeability could, therefore, create a new avenue for overcoming poisoning problems. I used DFT calculations to predict the H permeability in nine different metal sulfides. None of these metal sulfides, however, showed promising results as H_2 purification membranes; some of them could even be considered as H_2 barrier layers due to the extremely slow diffusion of H in these sulfides. Secondly, I examined the H permeability in a series of PdCuAg ternary alloys. The concept behind this work was to use additive metal atoms that will enhance H permeability in PdCu based alloys, since PdCu binary alloys have experimentally been observed to increase the resistance to H_2S but low H permeability relative to pure Pd.[1] I found that adding Ag improves the solubility of H, a dominant factor in the permeability of H through PdCuAg alloys. H permeabilities were predicted for a board range of PdCuAg ternary compositions, within some of which were shown to have higher permeability than pure Pd. My calculations indicated that PdCuAg ternary alloys could be a good candidate in the purification of H_2.

Finally I examined the permeation of carbon through pure Pd and Pd-based alloys. The predicted diffusivity of carbon in pure Pd was found to be in a good agreement with experimental measurements. Similar predictions were made for Pd based alloys. The

diffusivity of carbon in $Pd_{77.7}Ag_{22.3}$ was found to be 2-3 orders of magnitude than in pure Pd, mainly due to the diffusion paths for C that are effectively blocked by unfavorable sites created by Ag atoms in the alloy.

An important feature of all of the work in this thesis is that my computational predictions required no experimental input. This implies that although my work focuses on the prediction of Pd-based alloy membranes, the same method could be applied for predicting the performance of other materials for H_2 purification purposes. Semidey-Flecha and Sholl have shown that my method works well for different $Pd_{96.3}M_{3.7}$ alloys. Screening of other PdCuM ternary alloys could also been done using my method. Besides that, there are several interesting opportunities for further work. First, in this thesis, I focus on substitutionally random fcc metal alloys as H_2 purification membranes. The binary phase diagrams of metals, however, list many ordered intermetallics, some with different crystal structures from the constituent metals. This leads to the interesting question of whether these ordered intermetallics metals could be used in hydrogen purification. Kamakoti and Sholl have studied the performance of PdCu bcc alloys, and this ordered alloy exhibits high hydrogen permeability because H can diffuse rapidly in this structure.[1] In Chapter IV, I discussed how to calculate the solubility and diffusivity of hydrogen in ordered metal sulfides. A similar computational approach could play an important role in screening ordered intermetallic metals. Secondly, as I have discussed in Chapter V, the understanding and prediction of the diffusion behavior of interstitial hydrogen in metal alloys still remains challenging. My current method to predict the diffusivity requires a great amount of DFT calculations, accurate cluster expansion modeling of the data from DFT calculations and kinetic Monte

Carlo (KMC) simulations based on the cluster expansion models. In Chapter V I showed that the Average Jump Rate Theory (AJRT) could give reasonable predictions of diffusivity for $Pd_{96.3}Ag_{3.7}$. The advantage of using the AJRT is that it avoids the KMC simulations and only uses simplified models for the binding energies and activation energies barriers, instead of the cluster expansion models. It would be useful to have a more detailed idea of how well this approach matches with KMC simulations. If AJRT could still give reasonable predictions for other alloys, it could provide an additional approach in prediction the performance of metal alloys.

7.2 Reference:

[1]P. Kamakoti, B. D. Morreale, M. V. Ciocco, B. H. Howard, R. P. Killmeyer, A. V. Cugini, D. S. Sholl Science 307 569 (2005)

[2]B. D. Morreale, B. H. Howard, O. Iyoha, R. M. Enick, C. Ling, D. S. Sholl J. Membr. Sci. 46 6313 (2007)

Appendix

In this section, I showed the validation process of cluster expansion (CE) modeling of the binding energies of H in the interstitial sites and energies in the transition states for all alloys I considered in Chapter V. The validation of a CE model involves two steps. First, I compared the energies predicted by CE model and DFT calculations. This comparison is shown in Fig. 1. It is clear that all CE models gave an accurate prediction for the energies compared with DFT calculations, as proven by the LOO error and the least square error listed in Table 1. The LOO error and the least square error are defined in Eq. (5.2) and (5.4), respectively.

The second step to validate a CE model is to compare the distribution of energies predicted by CE model and obtained from DFT calculations. I compared the cumulative probabilities of the energies predicted by CE models and DFT calculations in Fig. 2. for all alloys. It is clear that the cumulative probabilities generated from CE predictions didn't deviate from DFT results significantly, which indicates that the CE models gave an accurate description of the energy distributions. Based on my discussions in Chapter V, these two comparisons ensure the validation of CE models used in the prediction of the macroscopic properties of H solutions.

Table A.1: The LOO error (R_{LOO}) and least square error (R_{LS}) of CE models for each alloy, and the number of data used to get the CE model.

alloy	site	data	R_{LOO} ($\times 10^{-3}$eV)	R_{LS} ($\times 10^{-3}$eV)
$Ag_{3.7}$	O	21		1.2
	T	88		4.0
	TS	92		3.4
$Ag_{7.4}$	O	36	11.3	2.1
	T	92	3.2	4.2
	TS	92	13.1	6.3
$Ag_{18.5}$	O	54	3.9	1.5
	T	108	8.7	3.2
	TS	432	13.1	7.8
$Cu_{3.7}$	O	21		2.9
	T	88		6.5
	TS	92		7.0
$Cu_{3.7}Ag_{3.7}$	O	36	1.4	4.2
	T	92	2.5	9.3
	TS	92	7.3	10.4
$Cu_{3.7}Ag_{11.1}$	O	27	3.1	6.1
	T	54	10.6	10.5
	TS	216	6.8	13.4
$Cu_{11.1}$	O	27	2.5	4.7
	T	54	1.6	3.2
	TS	216	16.7	12.1
$Cu_{11.1}Ag_{3.7}$	O	27	1.9	3.1
	T	54	4.4	6.7
	TS	216	8.9	7.4
$Cu_{11.1}Ag_{7.4}$	O	27	4.5	6.2
	T	54	6.2	8.1
	TS	216	11.3	19.7
$Cu_{11.1}Ag_{18.5}$	O	54	1.5	7.4
	T	108	3.5	14.3
	TS	432	10.1	16.2
$Cu_{25.9}Ag_{3.7}$	O	27		9.9
	T	54		20.3
	TS	216		16.9
$Cu_{25.9}Ag_{7.4}$	O	54	1.7	11.6
	T	108	4.3	12.3
	TS	432	7.7	18.7

Figure A.1: The binding energies in the octahedral sites (O), tetrahedral sites (T) and the energy in the transition state (TS) obtained from DFT calculations and predicted by CE models for alloys (a) $Pd_{92.6}Ag_{7.4}$ (b) $Pd_{81.5}Ag_{18.5}$ (c) $Pd_{92.6}Cu_{3.7}Ag_{3.7}$ (d) $Pd_{85.2}Cu_{3.7}Ag_{11.1}$ (e) $Pd_{88.9}Cu_{11.1}$ (f) $Pd_{85.2}Cu_{11.1}Ag_{3.7}$ (g) $Pd_{81.5}Cu_{11.1}Ag_{7.4}$ (h) $Pd_{70.4}Cu_{11.1}Ag_{18.5}$ and (i) $Pd_{66.7}Cu_{25.9}Ag_{7.4}$

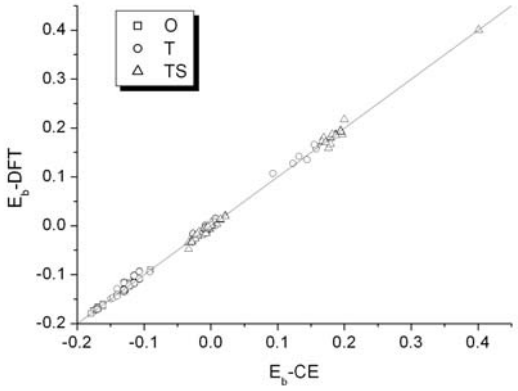

(a) $Pd_{92.6}Ag_{7.4}$

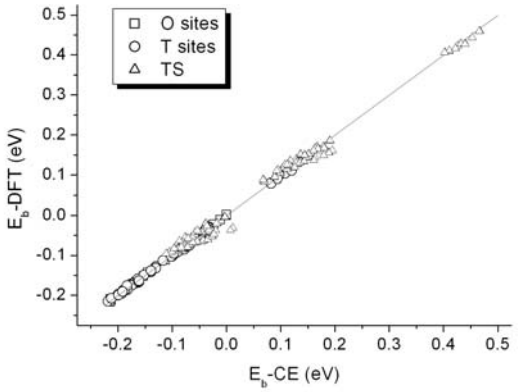

(b) $Pd_{81.5}Ag_{18.5}$

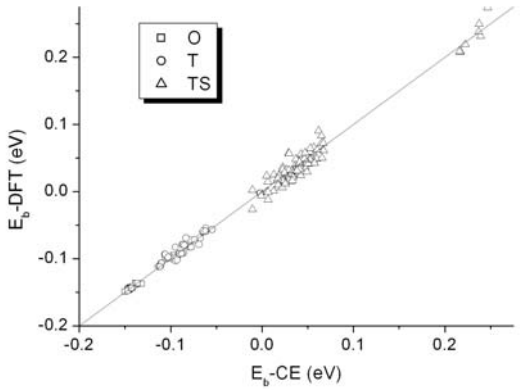

(c) $Pd_{92.6}Cu_{3.7}Ag_{3.7}$

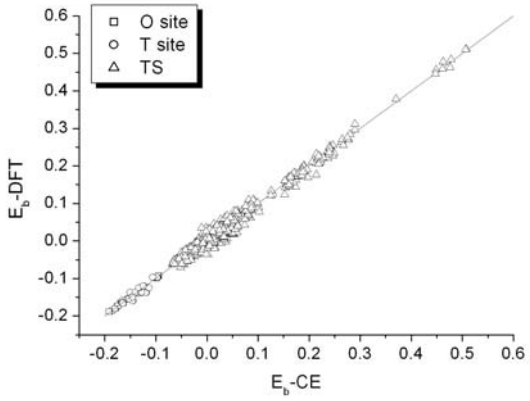

(d) $Pd_{85.2}Cu_{3.7}Ag_{11.1}$

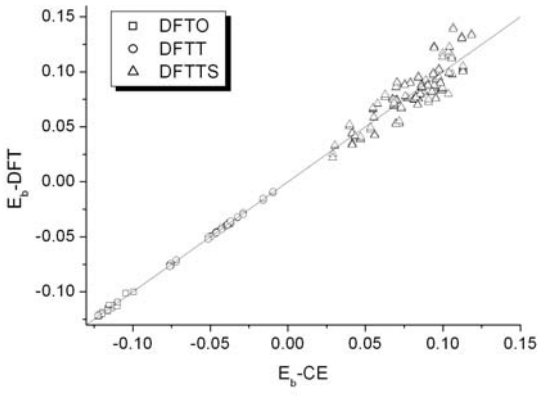

(e) $Pd_{88.9}Cu_{11.1}$

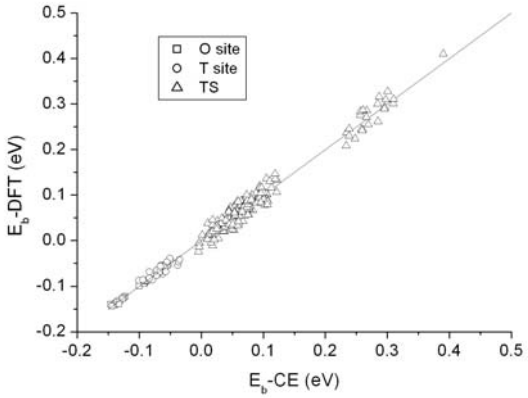

(f) $Pd_{85.2}Cu_{11.1}Ag_{3.7}$

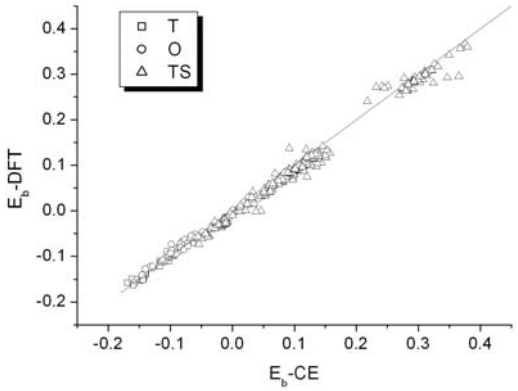

(g) $Pd_{81.5}Cu_{11.1}Ag_{7.4}$

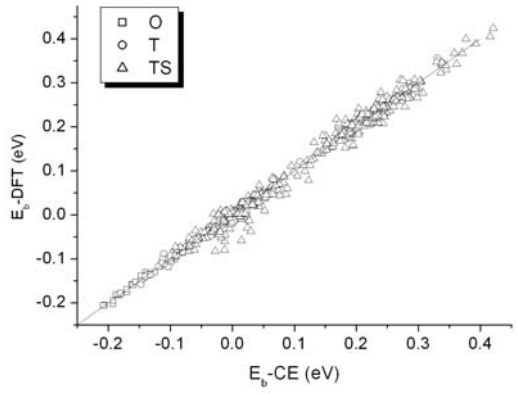

(h) $Pd_{70.4}Cu_{11.1}Ag_{18.5}$

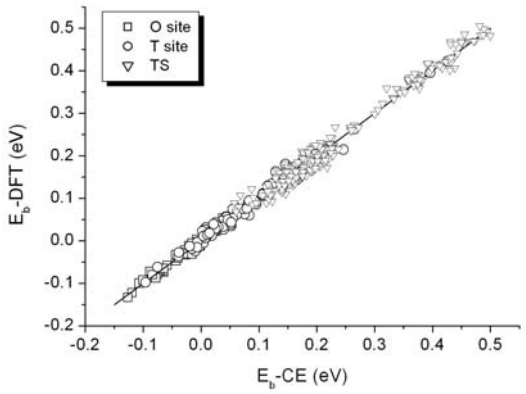

(i) $Pd_{66.7}Cu_{25.9}Ag_{7.4}$

Figure A.2: The cumulative probabilities for the binding energies in the octahedral sites (O), tetrahedral sites and the energies in the transition states (TS) as obtained from DFT calculation and CE model on a large random cell. (a) $Pd_{92.6}Ag_{7.4}$;(b) $Pd_{81.5}Ag_{18.5}$; (c) $Pd_{92.6}Cu_{3.7}Ag_{3.7}$; (d) $Pd_{85.2}Cu_{3.7}Ag_{11.1;}$ (e) $Pd_{88.9}Cu_{11.1}$ (f) $Pd_{85.2}Cu_{11.1}Ag_{3.7}$ (g) $Pd_{81.5}Cu_{11.1}Ag_{7.4}$ (h) $Pd_{70.4}Cu_{11.1}Ag_{18.5}$ and (i) $Pd_{66.7}Cu_{25.9}Ag_{7.4}$

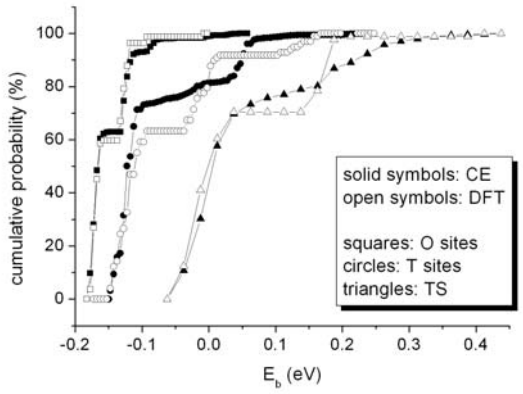

(a) $Pd_{92.6}Ag_{7.4}$

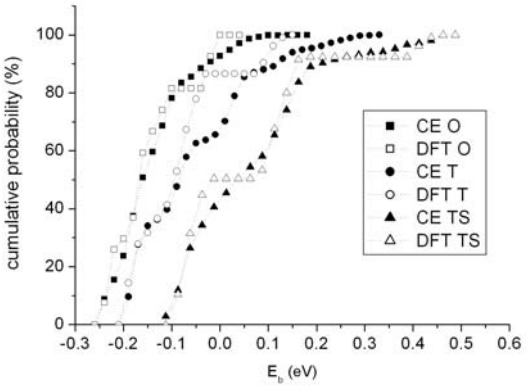

(b) $Pd_{81.5}Ag_{18.5}$

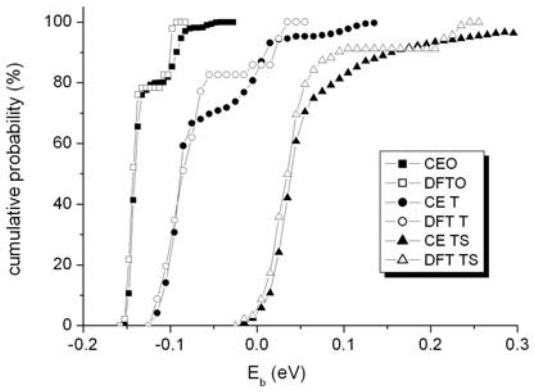

(c) $Pd_{92.6}Cu_{3.7}Ag_{3.7}$

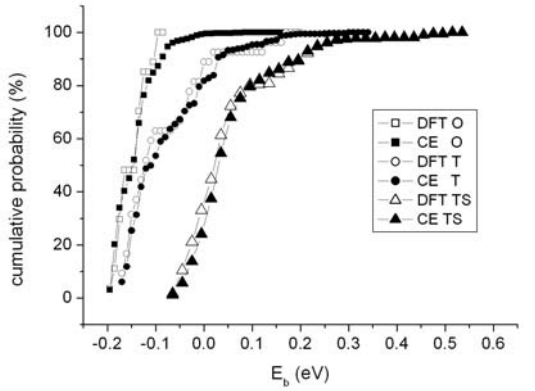

(d) $Pd_{85.2}Cu_{3.7}Ag_{11.1}$

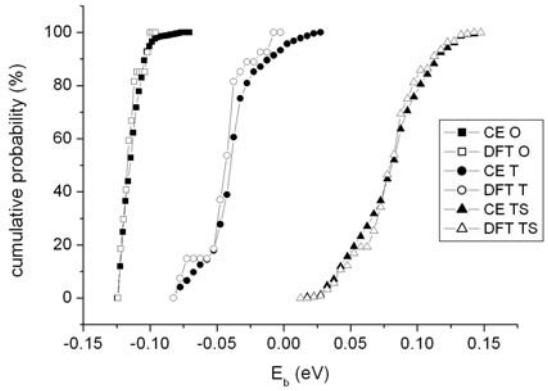

(e) $Pd_{88.9}Cu_{11.1}$

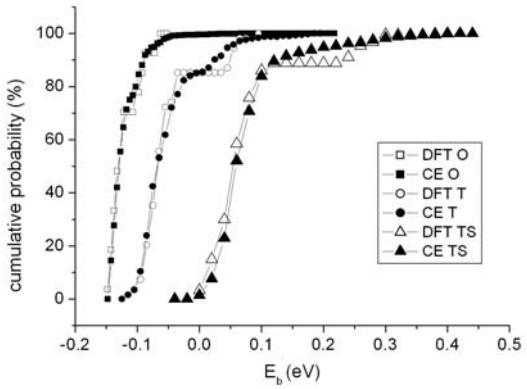

(f) $Pd_{85.2}Cu_{11.1}Ag_{3.7}$

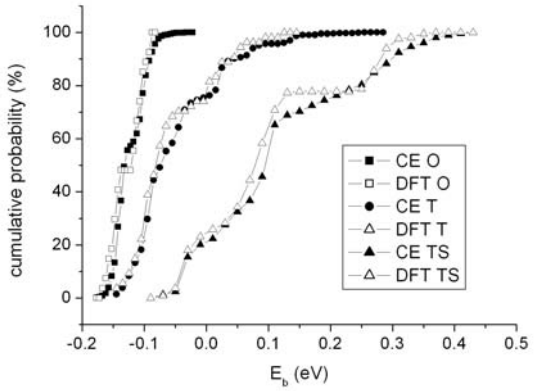

(g) $Pd_{81.5}Cu_{11.1}Ag_{7.4}$

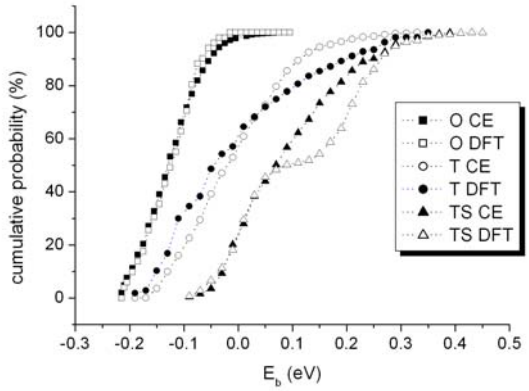

(h) $Pd_{70.4}Cu_{11.1}Ag_{18.5}$

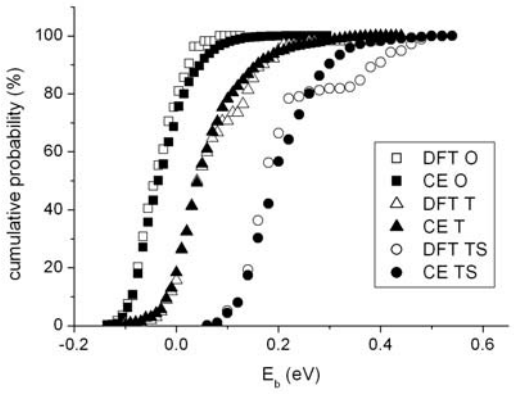

(i) $Pd_{66.7}Cu_{25.9}Ag_{7.4}$